

UNIVERSITÉ DE MONTRÉAL

DYNAMICS AND CONTROL OF BLUFF-BODY-WAKE-STRUCTURE  
INTERACTION

NEGAR NABATIAN  
DÉPARTEMENT DE GÉNIE MÉCANIQUE  
ÉCOLE POLYTECHNIQUE DE MONTRÉAL

THÈSE PRÉSENTÉE EN VUE DE L'OBTENTION  
DU DIPLÔME DE PHILOSOPHIÆ DOCTOR  
(GÉNIE MÉCANIQUE)  
MAI 2014

UNIVERSITÉ DE MONTRÉAL

ÉCOLE POLYTECHNIQUE DE MONTRÉAL

Cette thèse intitulée :

DYNAMICS AND CONTROL OF BLUFF-BODY-WAKE-STRUCTURE INTERACTION

présentée par : NABATIAN Negar

en vue de l'obtention du diplôme de : Philosophiæ Doctor

a été dûment acceptée par le jury d'examen constitué de :

M. LAKIS Aouni A., Ph.D., président

M. MUREITHI Njuki W., Ph.D., membre et directeur de recherche

M. KAHAWITA Rene, Ph.D., membre

Mme BOTEZ Ruxandra Mihaela, Ph.D., membre

## DEDICATION

گر مرید راه عشقی، فکر بدنامی مکن  
شیخ صنغان، خرقه رهن خانه خدا داشت

در حرکاتی که آغاز می‌کنی، بخشی از عمرت را در آن کار می‌گذاری و تجربه‌های تلخ و شیرین را از سر می‌گذرانی. حاصل این کار می‌شود یک خط که روح را تعالی  
می‌بخشد. در این بین، فقط آنهایی که همراهت بوده‌اند حال تو را می‌فهمند. همانا که بی‌نیاز از کلمات با نوازششان سخن می‌گویند و چه عمیق و گویا. خانواده و اساتیدم در ایران بی  
شک برای من همان همراهانند. این کار به احترام باور مشرکان تقدیم می‌شود به مردان و زنان شریف سرزمینم که برای ساختن آینده‌ای بهتر در ایران تلاش می-  
کنند.

*“If thou be a disciple of love’s Path, defame not:*

*Pawned at the vintner’s house, his religious garment Shaikh San’an held”*

*Hafez*

*At each work you leave a part of your life while passing through some hard and sweet experiences. The result is a pleasure that sublimates your soul. Among your companions, only few ones understand how you really feel. The ones that needless of words talk through their eyes, and how deeply. My family and professors in Iran undoubtedly are those ones for me. This Thesis due to our common belief is dedicated to all respectful women and men of my land who are trying to make a better future for Iran.*

## ACKNOWLEDGMENTS

Firstly, I would like to thank my supervisor, Prof. Njuki Mureithi for his guidance throughout this research work and associated publications. The financial support provided from his research grants by the Natural Sciences and Engineering Research Council of Canada (NSERC) is also acknowledged. For this dissertation I would like to thank my committee members: Prof. Aouni Lakis, Prof. Ruxandra Botez, Prof. Rene Kahawita and Prof. Luc Adjengue for their time and interest. I would like to acknowledge my colleague Xiaofei Xu for his guidance and useful suggestions in modeling work. I am also grateful to my colleagues Anne-Laure Menard, Malek Adouni, Hamed Marouane and Cedric Beguin for their help in translation process of “Résumé” and “Condensé en français”. Additionally, I would like to thank all my other colleagues who made a friendly environment for working and became good friends of mine. I owe thanks to my close friends in Iran who supported me.

Finally, I would like to express my deepest gratitude to my lovely family. To my parents and brother who supported me with their endless love. To my wonderful family in Canada especially dear Katy who made life enjoyable once again and to my previous professors in Iran who made me believe their presence despite of the long distance. Thank you.

## RÉSUMÉ

L'interaction fluide-structure est observée dans la majorité des applications industrielles. L'interaction peut conduire à la génération de forces indésirables affectant les structures et causant de la fatigue ou des dommages. Une approche pour comprendre la dynamique fondamentale et la stabilité des sillages des cylindres consiste à réaliser des simulations utilisant les oscillations forcées. Deux aspects d'un tel écoulement sont considérés. Le premier concerne la dépendance des symétries de configuration de détachement tourbillonnaire avec l'amplitude des oscillations forcées, de la fréquence d'excitation et de la direction des oscillations. Les oscillations forcées, dépendantes de l'amplitude et de la fréquence des oscillations, entraînent la formation de différentes configurations de sillage présentant des symétries spécifiques. Les simulations numériques et les analyses de stabilité sont utilisées pour déterminer les modes instables du sillage et leurs bifurcations. L'oscillation forcée dans la direction d'écoulement d'un cylindre circulaire est étudié pour prédire les modes du sillage sur une plage déterminée d'amplitude et de fréquence. Les calculs numériques en deux dimensions des équations de Navier-Stokes sont réalisés en utilisant la méthode des conditions aux frontières périodiques forcées avec une plage de fréquence de forçage  $f_e / f_s \in [1-2]$ ; couvrant les régimes d'excitations harmoniques et super-harmoniques avec des ratios d'amplitude dans la plage  $A / D \in [0-0.5]$ . Les modes d'accrochage symétriques et asymétriques sont observés pour trois différents ratios d'amplitude et de fréquence d'oscillation. Le mode asymétrique 2S lorsque  $f_e / f_s = 1$  pour  $A/D=[0.35-0.5]$ , le mode P+S à  $f_e / f_s = 1.5$  pour  $A/D=[0.175,0.5]$ , et le mode S à  $f_e / f_s = 2$  pour  $A/D=[0.175,0.5]$  sont confirmés. À cause de la non-linéarité des équations de Navier-Stokes et de la complexité de la dimension infinie de la dynamique des fluides, les modes primaires sont calculés à l'aide de l'outil de décomposition orthogonale aux valeurs propres (POD). Une procédure de Galerkin est utilisée pour projeter les équations de Navier-Stokes dans un espace de dimension réduite incluant les deux premiers modes POD. Cette méthode réduit la taille du problème d'un espace de dimension infinie à un nombre fini de modes (degrés de liberté) représentant la dynamique du sillage. Les modes dominants du détachement tourbillonnaire sont invariants en fonction des groupes de symétrie. La théorie de la bifurcation équivariante est utilisée pour développer le modèle d'ordre inférieur en utilisant les propriétés de symétrie des modes principaux. Ainsi, la bifurcation équivariante et les théories des formes normales sont combinées avec des calculs numériques des équations de Navier-Stokes pour

décrire précisément les propriétés spacio-temporelles des modes de sillage d'écoulement et de leurs bifurcations. Une analyse linéaire du modèle analytique de bas ordre aux environs du point de bifurcation est réalisée pour prédire les séquences de bifurcation observées sur les simulations. La bifurcation en double-tore pour l'excitation harmonique, le mode de compétition pour le cas super non-harmonique pour  $f_e / f_s = 1.5$  qui entraîne le bris de la symétrie de réflexion et dans le cas super-harmonique pour  $f_e / f_s = 2$  changeant la symétrie de réflexion de la fonction propre dominante sont tous fidèlement prédits par le modèle d'ordre réduit proposé. Les résultats présentés dans cette thèse se concentrent sur la compréhension de la physique des modes de détachement tourbillonnaire en fonction des ratios d'amplitude et de fréquence des oscillations forcées.

Le second aspect considéré dans cette thèse est la stabilité des ondes en deux dimensions pour des perturbations tridimensionnelles avec  $Re=200$ . Les simulations tridimensionnelles sont réalisées dans le cas d'oscillations harmoniques forcées avec des amplitudes d'oscillation sélectionnées et les résultats sont comparés à ceux obtenus avec les simulations en deux dimensions. Les résultats correspondent bien avec le modèle 2D qui montre que l'hypothèse de l'onde 2D pour l'oscillation forcée en ligne est correcte. Le mouvement du cylindre empêche les instabilités tridimensionnelles de l'écoulement, ce qui le maintient en deux dimensions. Les deux simulations en 2D et 3D sont aussi réalisées pour évaluer l'influence du mouvement du cylindre sur la structure de l'onde et pour proposer un mécanisme physique de la suppression du détachement du tourbillon de Karman. Les modes asymétriques 2S et P+S, et le mode symétrique S ainsi que les modes quasi-statiques sont observés au niveau des résultats numériques. Il a été montré que le coefficient de portance diminue lorsque le mode symétrique se développe dans l'onde. La région d'accrochage pour différents cas est également déterminée. Il a été montré que la région d'accrochage s'élargit en augmentant le ratio de fréquence forcée. Basé sur le modèle à bas ordre et sur les résultats numériques, le mécanisme physique du détachement tourbillonnaire et des effets des oscillations sont expliqués.

## ABSTRACT

Fluid-structure interaction is encountered in most of the engineering and industrial flow applications. The interaction can lead to generation of undesirable forces acting on structures and causing fatigue or damage. One approach to understanding the fundamental wake flow dynamics and stability is to conduct simulations using forced oscillation of a cylinder. Two aspects of such a flow are considered. The first is the dependence of vortex shedding pattern symmetries on the forced oscillation amplitude, forcing frequency ratios and the direction of the oscillation relative to flow direction. The forced oscillation, depending on the amplitude and frequency of the oscillation, causes formation of various patterns which have specific symmetries. Numerical simulations and stability analysis are employed to determine the unstable wake flow modes and their bifurcations. The forced inline oscillation of a circular cylinder is studied to predict the wake modes over a prescribed range of amplitudes and frequencies. The two-dimensional numerical computations of the Navier-Stokes equations are performed using forced periodic boundary condition method in the range of forcing-to-shedding frequency ratios  $f_e / f_s \in [1-2]$ ; covering the harmonic and superharmonic excitation regimes with amplitude ratio in the range  $A / D \in [0-0.5]$ . Symmetric and asymmetric lock-on modes are observed for three different oscillation amplitudes and frequency ratios. The asymmetric 2S mode when  $f_e / f_s = 1$  for  $A/D = [0.35-0.5]$ , P+S mode at  $f_e / f_s = 1.5$  for  $A/D = [0.175, 0.5]$  and S mode at  $f_e / f_s = 2$  for  $A/D = [0.175, 0.5]$  are confirmed. Due to the nonlinearity of the Navier-Stokes equations and the complexity of the infinite dimensional flow dynamics, the primary modes are calculated by the proper orthogonal decomposition (POD) tool. A Galerkin procedure is used to project the Navier-Stokes equations onto a low-dimensional space spanned by the first two POD modes. This method reduces the problem size from an infinite-dimensional space to a finite number of modes (degree-of-freedom) representing the wake dynamics. The vortex shedding dominant modes are invariant under their symmetry groups. The equivariant bifurcation theory is employed to develop the low order model using the symmetry properties of the primary modes. Thus, equivariant bifurcation and normal form theories are combined with numerical computations of the Navier-Stokes equations to precisely describe the spatio-temporal properties of the wake flow modes and their bifurcations. A linear analysis of the analytical low order model near the bifurcation point is performed to predict the bifurcation sequences observed in simulations. The torus-doubling bifurcation for harmonic

excitation, the mode competition for super non-harmonic case at  $f_e / f_s = 1.5$  which leads to the reflection symmetry breaking and for superharmonic case at  $f_e / f_s = 2$  switching of the dominant eigenfunction reflection symmetry are all well predicted with the proposed reduced order model. The results presented in this Thesis are focused on the understanding the physics of the vortex shedding patterns (modes) with respect to the forced oscillation amplitude and frequency ratios.

The second aspect considered in the Thesis is the stability of the two-dimensional wakes to three-dimensional perturbations at  $Re=200$ . Three-dimensional simulations are performed for harmonic forced oscillation case at selected oscillation amplitudes and the results are compared to those obtained from two-dimensional simulations. The results are in good agreement with the 2D model which shows that the 2D wake assumption for the inline forced oscillation is correct. The cylinder motion inhibits the three-dimensional instabilities of the flow causing it to remain two dimensional. Both two- and three-dimensional simulations are also performed to assess the influence of cylinder motion on the wake structure and to propose a physical mechanism for suppression of the Karman vortex shedding. The asymmetric 2S, P+S and symmetric S mode as well as quasi-steady patterns are observed in the numerical results. It is shown that the lift coefficient decreases as the symmetric mode develops in the wake. The lock-on region for various cases is also determined. It is shown that the lock-on region becomes larger by increasing the forcing frequency ratio. Based on the low order model and numerical results the physical mechanism of the vortex shedding and oscillation effects are explained.



## CONDENSÉ EN FRANÇAIS

### Introduction

L'écoulement transverse autour d'un cylindre circulaire a été étudié extensivement à cause de son importance pratique en ingénierie et sa signification fondamentale en mécanique des fluides. Le détachement tourbillonnaire induit des forces fluctuantes, qui causent des vibrations de la structure lorsque synchronisé avec la fréquence naturelle de la structure. Ce phénomène est désigné comme des vibrations induites par vortex (VIV) et peut conduire à de la fatigue ou des dommages structuraux. Les VIV sont observées dans plusieurs applications industrielles comme les gazoducs sous-marins, les colonnes montantes de forage et les câbles de ponts suspendus exposés aux courants marins ou aux vents. D'un point de vue scientifique, des phénomènes physiques différents comme la séparation, le détachement tourbillonnaire, la formation de configuration de sillage, la résonance et le chaos sont observés dans l'écoulement transverse autour d'un cylindre circulaire. La fréquence de vibration dans la direction de l'écoulement est deux fois celle de la vibration dans la direction perpendiculaire à l'écoulement. Le nombre de cycles de contraintes dus à l'oscillation en ligne est deux fois le nombre des oscillations transverses. De plus, les vibrations en ligne sont initiées à de petites vitesses et ont lieu plus souvent. Ainsi, les dommages de fatigue due aux vibrations en ligne et ses effets sur la fatigue dus aux vibrations transverses, sont les motivations pour mieux comprendre le mécanisme physique du phénomène purement en ligne de la VIV. Pour comprendre la dynamique de l'écoulement et sa stabilité, des simulations utilisant l'oscillation forcée d'un cylindre ont été utilisées afin d'étudier la réponse du sillage du mouvement induit. L'interaction entre le détachement tourbillonnaire et le mouvement de la structure peut entraîner des vibrations auto-induites du cylindre et changer la configuration du sillage. La configuration du sillage peut être utilisée pour identifier les instabilités globales qui se développent dans le sillage derrière le cylindre circulaire et suivre la dynamique de son comportement de simple à chaotique.

Afin de mieux comprendre la dynamique du sillage, Williamson et Roshko, (1988) ont excité le sillage par des oscillations périodiques externes forcées. Cette approche est la clé pour comprendre l'interaction sillage-structure pendant les vibrations induites par vortex (VIV). Expérimentalement, l'oscillation forcée transverse est appliquée au cylindre à différentes amplitude et fréquence. Williamson et Roshko ont montré que les configurations de sillage sont dépendantes de la fréquence de forgeage, de l'amplitude ( $A/D$ ), de la direction de l'oscillation et du nombre de

Reynolds. Ainsi, en changeant chacun des paramètres, différentes configurations ou modes définis par leurs symétries peuvent être observés; les modes sont nommés 2P, 2S, P+S et 2P+2S basés sur le nombre et la combinaison de tourbillons sur les côtés du cylindre par cycle forcé. Il y a eu des recherches expérimentales incluant des oscillations forcées dans le sens axial du sillage de l'écoulement avec des combinaisons différentes d'amplitude d'oscillations sans dimension  $A/D$  et  $f_e/f_s$  avec  $f_e$  la fréquence d'excitation et  $f_s$  la fréquence naturelle de détachement. Griffin et Ramberg, (1976) ont été parmi les premiers à étudier le sillage de l'écoulement derrière un cylindre oscillant en ligne dans un écoulement non perturbé. Ils ont réalisé des simulations des oscillations forcées en ligne à travers une plage de ratios de fréquence  $f_e/f_s \in [1.2, 2.5]$  pour  $Re=190$ . Ils ont montré que, durant les oscillations forcées, le détachement tourbillonnaire est affecté par le mouvement du cylindre ; d'où les changements de détachement de tourbillon pour osciller à une fréquence structurale, un phénomène connu comme un accrochage. À la fois, le accrochage primaire lorsque  $f_e = f_s$  et subharmonique avec  $f_s = f_e/2$  ont été observés. Deux modes asymétriques de détachement tourbillonnaire 2S et 2P ont été observés à basses amplitudes pour  $0.06 < A < 0.22$ . Le mode asymétrique 2S correspond à l'allée de tourbillon de Von Karman, tandis que dans le mode 2P, deux paires de tourbillons sont échappés par cycle. Ces structures d'écoulement correspondent aux modes A-I et A-III tels que catégorisés par Ongoren et Rockwell, (1988) qui ont étudié les configurations du sillage d'un cylindre en oscillation forcée avec un angle par rapport à la direction de l'écoulement et des amplitudes d'oscillation sans dimension de 0.13 et 0.3 ainsi que des ratios de fréquences allant de 0.5 à 4.0. Deux modes de base, symétrique et antisymétrique, sont identifiés et classés en cinq sous-groupes. Le mode S correspond au détachement de tourbillon symétrique et les modes A-I, A-II, A-III et A-IV à la formation de tourbillons antisymétriques. Ongoren et Rockwell ont expliqué expérimentalement le changement entre les configurations de sillage et ont montré que les modes de détachement tourbillonnaire peuvent être symétriques, antisymétriques ou chaotiques en fonction de la fréquence de forçage et de l'amplitude d'oscillation.

Les différentes configurations de sillage de tourbillon sont classées en fonction de leurs propriétés de symétrie. Les propriétés de symétrie des configurations de sillage peuvent être utilisées pour une étude analytique de détachement de tourbillon issue d'un mode d'ordre inférieur. Le modèle de Stuart-Landau a été initialement appliqué pour modéliser la bifurcation de Hopf conduisant aux

résultats du détachement asymétrique de Karman par Provansal, (1987a). Il a trouvé que le sillage périodique de Karman est le produit saturé temporel du sillage global et a suggéré que la théorie de la stabilité linéaire peut être appliquée pour trouver la fréquence de saturation au voisinage de la fréquence de seuil. Plus tard, Barkley et al., (2000) ont suggéré un scénario de bifurcation pour décrire le développement et l'interaction entre les deux modes tridimensionnels. Les équations en amplitude tronquées discrètes de Landau incorporent les termes de couplage des modes d'instabilité A et B, et satisfont les propriétés de symétries spatio-temporelles de chaque mode. Afin de modéliser la variation des fréquences des modes de transition, les équations couplées de Landau ont ensuite été étendues dans le plan complexe par Sheard et al., (2003). Le modèle analytique pour étudier l'oscillation forcée en prenant en compte les propriétés de symétrie a été proposé pour la première fois par Mureithi, (2003; 2005). Il a utilisé la théorie de la symétrie équivariante pour étudier le sillage forcé de Von Karman. L'interaction non-linéaire du mode de Von Karman et du mode symétrique a été modélisée par la théorie de la bifurcation symétrique équivariante sous forme d'une paire d'équations discrètes en amplitude de bas ordre. Les coefficients des équations d'amplitude sont déterminés par analyse en décomposition orthogonale aux valeurs propres (POD) des résultats du CFD. Le mode forcé est considéré comme connu et ses effets sur le mode de détachement du tourbillon a été investigué.

Plusieurs recherches ont également été réalisées pour étudier l'effet de l'oscillation sur la transition du sillage en 3D. Williamson, (1996) a montré qu'au nombre de Reynolds de transition  $Re \approx 200$ , les effets de l'écoulement tridimensionnel apparaissent ce qui est montré par une discontinuité en hystérésis dans les valeurs du nombre de Strouhal. Il a été démontré que le caractère tridimensionnel du sillage du cylindre peut être retardé en forçant le cylindre à osciller à des amplitudes modérées. Koopman, (1967) et Griffin et Ramberg, (1976) ont montré que le sillage de l'écoulement est bidimensionnel à des amplitudes d'oscillation supérieures à  $0.1D$  pour un nombre de Reynolds jusqu'à 300-400. Berger, (1967) a montré via une étude expérimentale qu'en appliquant une oscillation transverse contrôlée avec des fréquences synchronisées avec les fluctuations du sillage, un régime laminaire de détachement de tourbillon peut être étendu jusqu'à  $Re=300-350$ . Plus tard, Gioria et Meneghini, (2010) ont montré que le seuil d'amplitude pour lequel la tridimensionnalité est supprimée se situe dans des plages de  $0.03D < A < 0.65D$  pour  $Re=200$ .

L'objectif général de ce travail est d'utiliser la bifurcation équivariante, la forme normale et les théories de stabilité avec des simulations numériques pour étudier la dynamique des sillages. Des simulations par ordinateur du sillage d'un cylindre d'écoulement soumis à des oscillations en ligne sont utilisées pour obtenir un aperçu physique du mécanisme responsable des diverses configurations de sillage et des bifurcations obtenus par combinaison de fréquence et d'amplitude de vibration. Les objectifs sont réalisés en trois phases. La première phase est l'excitation harmonique du cylindre à  $Re=200$  et la réalisation d'analyse de stabilité pour trouver les bifurcations qui ont lieu dans le sillage associée à cette excitation. Le modèle d'ordre réduit de la vitesse- $v$  calculée par POD est utilisé pour développer les équations modales d'amplitude à l'aide de la théorie de la bifurcation équivariante pour prédire la séquence de bifurcation correspondant à l'oscillation en ligne. Dans une seconde phase, les recherches ont été réalisées pour observer les configurations de sillage et construire la carte de la dynamique du coefficient de portance pour des combinaisons d'amplitude d'oscillation et des ratios de fréquences super non-harmonique et harmonique à  $Re=200$ . Aussi, le modèle analytique proposé dans la première phase prédit l'ensemble de bifurcations. Ceci aide à comprendre la façon dont les oscillations en ligne influencent la dynamique des sillages.

Dans une troisième phase, afin de s'assurer que les résultats des simulations 2D sont fiables, des simulations 3D ont été réalisées pour un écoulement à  $Re=200$  et un modèle de décomposition orthogonale aux valeurs propres a été développé pour trouver les modes primaires et leurs transitions causées par les oscillations forcées.

## **Méthodologie**

Tel que mentionné précédemment, une approche utilisée dans ces travaux pour comprendre l'interaction fluide-structure consiste à contrôler le mouvement du cylindre, permettant d'examiner séparément la réponse du sillage.

On réalise une simulation 2D du sillage de l'écoulement à  $Re=200$  avec une condition d'entrée d'écoulement périodique pour calculer les champs de vitesse et de pression. L'approximation du cylindre infini et des conditions aux limites périodiques sont les hypothèses choisies pour résoudre les calculs non-linéaires des équations de Navier-Stokes pour le modèle 2D instationnaire. À cause du caractère non-linéaire et complexe des équations de Navier-Stokes, l'outil de POD est utilisé pour déterminer les degrés de liberté (ou modes) minimum requis pour représenter le champ de

l'écoulement. Les modes dominants calculés par la projection POD-Galerkin du champ de vitesse transverse sont utilisés pour obtenir un système d'équations différentielles ordinaires (ODE) sur le temps. Les deux premiers modes primaires qui existent pour diverses amplitudes d'oscillation sont employés pour modéliser la dynamique du sillage. Chacun de ces modes a ses propres propriétés de symétrie. Les symétries des fonctions propres spatiales correspondant aux modes dominants de vitesse- $v$  sont appliquées aux équations maîtresses du système pour développer les équations d'amplitude modale avec la théorie de la bifurcation. Les coefficients des équations d'amplitude sont calculés avec la méthode des moindres carrés utilisant les *chronos* des deux modes primaires, qui sont transformés en signaux complexes par la transformation de Hilbert. De plus, l'information sur la fréquence de saturation est incluse via les coefficients complexes. Les termes linéaires des équations d'amplitude sont affectés majoritairement par la variation de l'oscillation dans la direction de l'écoulement et ainsi considérés comme les paramètres de bifurcation. En changeant les paramètres de bifurcation, les équations en amplitude de bas ordre peuvent avoir différentes solutions avec moins de symétrie que la symétrie des équations originales. Ce type de bifurcation avec des symétries est désigné comme un mécanisme brisant la symétrie. Plus précisément, la théorie de la bifurcation équivariante est appliquée pour classer les solutions en fonction de leurs symétries. Finalement, l'analyse de la stabilité linéaire du modèle proposé est réalisée à l'aide d'une carte de Poincaré et les ensembles de bifurcations causés par les variations des paramètres de bifurcation sont également étudiés dans des graphiques d'Argand des multiplicateurs de Floquet. La séquence de bifurcations observée en CFD et expérimentalement prédit par une analyse de bifurcation d'un modèle basé sur la symétrie.

Enfin, la structure du sillage et le phénomène d'accrochage sont numériquement étudiés dans la région au voisinage du sillage pour  $Re=200$  avec des amplitudes d'oscillation étendues jusqu'à  $0.5D$  et trois ratios de fréquences  $f_e/f_s = 1, 1.5$  et  $2$ . Le sillage de l'écoulement avec la vitesse, les contours du tourbillon et les transitions des coefficients de portance pour chaque combinaison d'amplitude d'oscillation et de ratios de fréquences forcées sont étudiés et la région d'accrochage est déterminée. Le scénario de bifurcation est appliqué au modèle analytique développé pour étudier la compétition des modes et déterminer les types de bifurcation et sélectionner le nombre d'onde des branches de solution. Les résultats sont comparés avec ceux obtenus numériquement.

Le sillage de l'écoulement tridimensionnel autour d'un cylindre circulaire forcé à osciller dans la direction d'un écoulement non perturbé est également étudié pour vérifier les résultats 2D. Les simulations numériques sont réalisées pour trois amplitudes d'oscillation sélectionnées  $A/D=0.0$ ,  $0.175$  et  $0.5$  avec une fréquence égale à la fréquence naturelle de détachement pour  $Re=200$ . Le modèle réduit de la vitesse transverse et le spectre de puissance du coefficient de portance sont employés pour analyser la dynamique de l'écoulement et des bifurcations qui ont lieu en fonction de l'oscillation en ligne du cylindre. Les résultats sont comparés avec les résultats 2D numériques précédemment obtenus afin de vérifier l'hypothèse du caractère bidimensionnel du sillage de l'écoulement à  $Re=200$  en considérant l'oscillation en ligne.

## Résultats

L'approche de travail a combiné la bifurcation équivariante et les théories de forme normale avec des simulations numériques pour découvrir les facteurs clés sous-jacents à la formation de différentes configurations de sillage. Divers modes de détachement tourbillonnaire sont formés en fonction de la combinaison d'une amplitude d'oscillation et d'une fréquence de forçage dans la direction de l'excitation. Le groupe de symétrie de l'écoulement de base détermine les caractéristiques de ces configurations bifurquées. Les principales contributions de cette thèse sont les suivantes:

1. Développement d'équations d'amplitude modale, en prenant en compte les symétries de forme normale à l'aide de la théorie de la bifurcation équivariante, capable de prédire la dynamique en oscillation en ligne forcée des sillages d'un cylindre.
2. Bifurcation et analyse de stabilité des équations couplées d'amplitude pour prédire les séquences de bifurcation observées dans les résultats CFD.

Le premier article (chapitre 2) inclut les calculs numériques en 2D du sillage d'un cylindre forcé à des oscillations dans la direction de l'écoulement avec des fréquences harmoniques forcées et des amplitudes d'oscillation sélectionnées. Le modèle de bas ordre a aussi été développé pour réduire les degrés de liberté du problème considéré. La décomposition POD-Galerkin a été utilisée pour développer des modèles d'ordre réduit pour le champ de vitesse transverse dans le sillage d'un cylindre circulaire. Les fonctions propres de la vitesse  $v$  ont été ensuite calculées par l'approche POD en utilisant des photos du champ d'écoulement de la simulation CFD. Les modes dominants obtenus ainsi que leurs structures spatiales ont été utilisés pour modéliser les caractéristiques du

sillage sur une vaste plage d'amplitudes d'oscillation et de ratios de fréquences forcées. Deux modes primaires sont considérés invariants sous l'action d'un groupe de symétrie. Les symétries des modes primaires du sillage ont été appliquées pour développer un modèle analytique en utilisant la théorie de la bifurcation équivariante. La dynamique du sillage a été modélisée par un ensemble d'équations différentielles ordinaires qui ont apporté un regard analytique sur le mécanisme physique. Basé sur les résultats CFD, en augmentant l'amplitude d'oscillation, les modes dominants atteignent un état quasi-périodique dans la région de transition et en augmentant plus tard l'amplitude forcée, deux ondes progressives subissent une bifurcation en double tore. Le mouvement du cylindre redynamise le mode asymétrique pour interagir avec le premier mode conduisant à la bifurcation en double-tore. Cependant, le mode S périodique doublement bifurqué a une plus grande amplitude que celle du mode asymétrique ce qui confirme le schéma de vitesse double-périodique symétrique transverse observé en simulation. La troisième harmonique du coefficient de portance existe dans la réponse du sillage d'écoulement à  $A/D=0.5$  à cause du mouvement dans la direction de l'écoulement du cylindre.

L'interaction non-linéaire entre les modes symétriques et asymétriques était qualitativement prédite par le modèle analytique. Les paramètres linéaires de bifurcation ont été changés par le mouvement du cylindre conduisant à briser la symétrie de la bifurcation. La compétition modale entre ces deux modes a été étudiée lorsqu'ils bifurquent simultanément. Dans l'analyse de la stabilité linéaire, la transition des modes primaires a été étudiée par le mouvement des multiplicateurs de Floquet dans le diagramme d'Argand. La paire complexe-conjugué des multiplicateurs de Floquet croise l'axe réel des valeurs négatives et coupe le cycle unitaire à -1 confirmant la bifurcation en double-tore. De plus, l'analyse de stabilité des équations couplées en amplitude a été réalisée dans une carte de Poincaré où deux ondes stables progressives subissent la bifurcation en double-tore. Les modes bifurqués ont des symétries spatiales similaires mais des nombres d'onde différents. Ce modèle peut prédire les séquences de bifurcation observées dans les résultats CFD. Par conséquent, les symétries et longueurs d'onde de chaque mode ont été caractérisés et le mécanisme physique expliquant les instabilités expliqué.

3. Identification des régions d'accrochage et de diverses configurations de détachement tourbillonnaire en stimulant l'oscillation forcée en ligne d'un cylindre circulaire dans la plage de

fréquences  $f_e / f_s \in [1-2]$  constituant les régions d'excitation harmonique et superharmonique avec des ratios d'amplitude appartenant à la plage  $A/D \in [0-0.5]$ .

4. Analyse de bifurcation des équations d'amplitude pour prédire la séquence de bifurcations qui se produit en fonction de la combinaison d'amplitude d'oscillation et des fréquences de forçage.

Avec une méthodologie identique dans le second article présenté au chapitre 3, les simulations des excitations forcées dans la direction de l'écoulement super non-harmoniques et super-harmoniques ont été réalisées. Les diverses configurations du détachement tourbillonnaire ont été observés avec différentes fréquences forcées et des amplitudes d'oscillation au sein de la région d'identification d'accrochage en utilisant les plans de phase et le spectre de puissance du coefficient de portance. Dans le cas de l'excitation harmonique, l'écoulement de base subit une bifurcation de Hopf à  $A/D=0.175$  et puisque la seconde fréquence est inférieure à la fréquence principale, le phénomène de domination a été observé. À  $A/D=0.5$  la transition d'un état quasi-périodique à un état d'accrochage se produit lorsque le mode dominant conserve la symétrie spatial de l'écoulement de base à la moitié de la fréquence de détachement. Pour des ratios de fréquences de forces irrationnelles  $f_e / f_s = 1.5$ , la région d'accrochage devient plus large que celle du cas de l'excitation harmonique et couvre  $A/D=0.175$ . La compétition entre les modes primaires symétrique and antisymétrique conduit à casser la symétrie de réflexion et le mode P+S bifurque du mode d'interaction. Dans le cas d'une excitation super-harmonique avec  $f_e / f_s = 2$ , le mode symétrique S remplace le mode de base asymétrique 2S alors que le mode de vitesse-v change du mode symétrique au mode asymétrique. L'accrochage apparait également avec une plage d'amplitude d'oscillation de  $[0.175-0.5]$ . L'analyse de bifurcation du modèle analytique prédit la symétrie des modes primaires, la longueur d'onde du mode dominant et les séquences de bifurcation ainsi que des résultats numériques CFD. Cependant, la fréquence du second mode n'a pas de correspondance dans le cas super-harmonique. Dans ce cas, plus de deux paramètres de bifurcation sont impliqués ce qui montre la complexité de l'interaction des modes. Aussi, le changement de configuration du détachement tourbillonnaire affecte significativement la force agissant sur le cylindre alors que l'amplitude du coefficient de portance est diminuée dans la configuration symétrique.

5. Étude de la stabilité des sillages bidimensionnels par rapport à des perturbations tridimensionnelles à  $Re=200$  à l'aide d'une analyse POD tridimensionnelle du sillage d'un cylindre circulaire forcé dans la direction de l'écoulement.



Pour finir, l'instabilité secondaire du sillage de l'écoulement a été considérée dans le troisième article présenté au chapitre 4. La simulation tridimensionnelle du sillage de l'écoulement à  $Re=200$  utilisant le modèle SST a été réalisée pour étudier l'effet du mouvement du cylindre sur le détachement du tourbillon. Les simulations tridimensionnelles montrent que la dynamique du sillage de l'écoulement demeure presque bidimensionnelle à  $Re=200$ . Il a été montré que la vibration du cylindre améliore la corrélation dans la direction de l'envergure des tourbillons et supprime les instabilités tridimensionnelles. Ceci suggère que le mouvement du cylindre a un effet stabilisant sur l'écoulement et que les simulations bidimensionnelles apportent de bons résultats et que le sillage de l'écoulement peut être considéré comme bidimensionnel.

### **Recommandations pour les travaux futurs**

La fréquence dominante de la vitesse transverse est une bonne représentation de la fréquence de détachement tourbillonnaire à l'exception du cas super-harmonique pour  $A/D=0.5$ . Puisqu'il y a un couplage non-linéaire entre écoulement en ligne et vitesse transverse, peut-être que le composant de tourbillon est plus représentatif pour l'identification de la fréquence de détachement puisqu'il contient à la fois les effets des vitesses  $u$  et  $v$ . Bien que les excitations forcées harmonique et super-harmonique du sillage d'écoulement sont étudiées, il reste à étudier un certain nombre de problèmes. Le premier est celui de la région d'excitation subharmonique dans laquelle d'après des études précédentes, il semble que le détachement tourbillonnaire dévierait des axes horizontaux et donc l'écoulement deviendrait doublement périodique. Ainsi, si le sillage de l'écoulement est périodique en deux dimensions alors le double-treillis devrait être utilisé pour modéliser la dynamique du sillage de l'écoulement. Une autre limite de cette recherche qui demeure une recommandation pour des travaux futurs est la caractérisation des instabilités secondaires dans le sillage de l'écoulement à des nombres de Reynolds plus élevés. À des nombres de Reynolds plus élevés, l'effet tridimensionnel se manifeste et les effets dans la direction d'envergure peuvent changer la structure du sillage de l'écoulement, donc l'utilisation d'un modèle temporel n'est pas suffisante à cause de dislocations spatiales et un modèle de Ginzburg-Landau devrait être employé. Aussi, des expériences peuvent être réalisées sur une plage élargie de ratios de fréquences et d'amplitudes d'oscillation dans la direction en ligne qui conduit à une cartographie des modes de sillage pour réaliser le graphique de Griffin.

## TABLE OF CONTENTS

DEDICATION .....	III
ACKNOWLEDGMENTS .....	IV
RÉSUMÉ .....	V
ABSTRACT .....	VII
CONDENSÉ EN FRANÇAIS .....	IX
TABLE OF CONTENTS .....	XVIII
LIST OF TABLES .....	XX
LIST OF FIGURES .....	XXI
LIST OF ABBREVIATIONS .....	XXVI
LIST OF APPENDICES .....	XXIX
INTRODUCTION .....	1
Chapter 1 LITERATURE REVIEW .....	5
1.1 The phenomenon of vortex shedding and flow regimes .....	5
1.2 Secondary instabilities in the wake .....	8
1.3 VIV and flow pattern properties .....	16
Chapter 2 ARTICLE 1: BIFURCATION AND STABILITY ANALYSIS WITH THE ROLE OF NORMAL FORM SYMMETRIES ON THE HARMONIC STREAMWISE FORCED OSCILLATION OF THE CYLINDER WAKE .....	21
2.4 Introduction .....	22
2.5 Numerical computations .....	24
2.6 Numerical Solution and POD Modes .....	25
2.7 Derivation of Symmetry Based Model .....	31
2.7.1 Truncation of the amplitude equation up to third order $O(3)$ .....	32
2.7.2 Truncating the amplitude equation up to order $O(7)$ .....	33
2.7.3 Solution branches .....	35
2.7.4 Coefficients calculation using dominant POD modes of the transverse velocity .....	36
2.8 Bifurcation and stability analysis .....	39
2.8.1 Poincare map .....	43
2.9 Conclusion .....	44

Chapter 3	ARTICLE 2: LOCK-ON VORTEX SHEDDING PATTERNS AND BIFURCATION ANALYSIS OF THE FORCED STREAMWISE OSCILLATION OF THE CYLINDER WAKE..	46
3.1	Introduction .....	46
3.2	Numerical computations.....	49
3.3	Numerical Results .....	50
3.3.1	Harmonic excitation .....	50
3.3.2	Super non-harmonic excitation with $f_e/f_s = 1.5$ .....	53
3.3.3	Superharmonic excitation with $f_e/f_s = 2$ .....	55
3.4	Derivation of Amplitude Equations Based on Symmetry .....	59
3.4.1	Basic solution branches .....	61
3.4.2	Coefficients calculation using the $v$ -velocity POD primary modes and bifurcation analysis ...	61
3.5	Conclusion.....	66
Chapter 4	ARTICLE 3: POD ANALYSIS OF THREE-DIMENSIONAL FORCED HARMONIC INLINE WAKE FLOW OF A CIRCULAR CYLINDER.....	68
4.1	Introduction .....	69
4.2	Numerical computations.....	71
4.2.1	Methodology.....	71
4.2.2	POD Analysis of the transverse velocity.....	72
4.3	Results .....	73
4.4	Conclusion.....	84
	GENERAL DISCCUSIONS.....	86
	CONCLUSIONS AND RECOMMENDATIONS FOR FUTURE WORK.....	89
	REFERENCES .....	92
	APPENDICES .....	99

## LIST OF TABLES

Table 2-1: The coefficients of the amplitude equation deduced from the least squares method. ...	38
Table 2-2: Floquet multiplier values at different bifurcation parameters. ....	42
Table 3-1: The coefficients of the amplitude equation deduced from the least square method.....	62

## LIST OF FIGURES

Figure 1-1: Flow separation structure (Sumer and Fredsøe, 2006).....	5
Figure 1-2: Vortex Shedding from sides of cylinder (Sumer and Fredsøe, 2006).....	6
Figure 1-3: Flow regimes over a smooth cylinder (Sumer and Fredsøe, 2006).....	7
Figure 1-4: Experimental curve of Strouhal number vs. Reynolds number (Williamson, 1996). ...	8
Figure 1-5: Flow visualization and sketch of symmetries of modes A and B (Leweke and Williamson, 1998; Williamson, 1996). .....	9
Figure 1-6: Iso-surfaces of streamwise vorticity obtained from PIV measurements showing the symmetries of modes A and B. Light grey surfaces represent the positive vorticity and dark grey represent negative vorticity (Leweke and Williamson, 1998). .....	9
Figure 1-7: Streamline of the flow, shows elliptical shape of vortex core and also stagnation point in the flow (Leweke and Williamson, 1998; Williamson, 1996). .....	10
Figure 1-8: Spanwise vorticity of the 2-D wake flow at Re=200 that shows flow features (Leweke and Williamson, 1998; Williamson, 1996). .....	11
Figure 1-9: Physical mechanism of mode A vortex loops production (Carmo, 2009). .....	11
Figure 1-10: Physical mechanism of mode B streamwise vortices formation in the braid shear layer (Carmo, 2009). .....	12
Figure 1-11: Curves of Neutral stability for 2-D Karman vortex with respect to spanwise perturbations. Upper region relates to long-wavelength instabilities starts at Re=190, lower region corresponds to short-wavelength, initiated at Re=260 (Barkley and Henderson, 1996).....	13
Figure 1-12: Bifurcation diagram of amplitude equations, Solid lines indicate stable states and dash lines transition case of A, B and A+B interaction case. 2-D branch has A=B=0 (Barkley et al., 2000).....	15
Figure 1-13: Different regimes for vortex wake modes showing the 2S, 2P, and P+S mode regimes at Re=1000 (Williamson and Govardhan, 2008). .....	17
Figure 1-14: Typical flow structures of the streamwise forced flow (Griffin and Ramberg, 1976).....	18
Figure 1-15: Flow structure dependence on $f_e/f_s$ and A/D (Ongoren and Rockwell, 1988). .....	19
Figure 2-1: Schematic of 2D domain and structured mesh. ....	24

Figure 2-2: Singular values of $v$ -velocity for stationary cylinder .....	26
Figure 2-3: Singular values of $v$ -velocity for oscillation amplitude $A/D = 0.5$ . .....	26
Figure 2-4: The spatial and temporal basic functions of two dominant modes for $A/D = 0.0$ . (a) first <i>topos</i> (b) first <i>chronos</i> (c) second <i>topos</i> (d) second <i>chronos</i> . .....	26
Figure 2-5: The spatial and temporal basic functions of two dominant modes for $A/D = 0.15$ (a) first <i>topos</i> (b) first <i>chronos</i> (c) second <i>topos</i> (d) second <i>chronos</i> . .....	27
Figure 2-6: The spatial and temporal basic functions of two dominant modes for $A/D = 0.35$ (a) first <i>topos</i> (b) first <i>chronos</i> (c) second <i>topos</i> (d) second <i>chronos</i> . .....	28
Figure 2-7: The spatial and temporal basic functions of two dominant modes for $A/D = 0.5$ (a) first <i>topos</i> (b) first <i>chronos</i> (c) second <i>topos</i> (d) second <i>chronos</i> . .....	28
Figure 2-8: Temporal evolution of two primary modes at different oscillation amplitudes (a,b) fixed cylinder case (c,d) $A/D = 0.15$ (e,f) $A/D = 0.35$ (g,h) $A/D = 0.5$ . .....	29
Figure 2-9: Hilbert transform of lift coefficient for (a) fixed cylinder case (b) $A/D = 0.175$ (c) $A/D = 0.5$ . Lift coefficient frequency peak for (d) fixed cylinder case (e) $A/D = 0.175$ (f) $A/D = 0.5$ .....	30
Figure 2-10: (a) The <i>chronos</i> of modes S and K from CFD, (b) Deduced S and K modes approximated from the least squares method of the dominant <i>chronos</i> data. ....	38
Figure 2-11: Quasi-periodic state of modes S and K at $\xi_0 = 0.0836$ , $\delta_0 = 0.29$ .....	39
Figure 2-12: Quasi-periodic state of modes S and K at $\xi_0 = 0.0826$ , $\delta_0 = 0.46$ .....	39
Figure 2-13: Complex amplitude of bifurcated mode S at $\xi_0 = 0.0826$ , $\delta_0 = 0.46$ .....	40
Figure 2-14: Complex amplitude of bifurcated mode K at $\xi_0 = 0.0826$ , $\delta_0 = 0.46$ .....	40
Figure 2-15: Limit cycle of amplitude term of mode S .....	40
Figure 2-16: Limit cycle of amplitude term of mode K .....	40
Figure 2-17: Movement of Floquet multipliers of mode K and S by variation of bifurcation parameters. ....	43
Figure 2-18: Poincare map of the modes S and K at (a,b) $\xi_0 = 0.0926$ , $\delta_0 = 0.25$ (c,d) $\xi_0 = 0.0836$ , $\delta_0 = 0.29$ and (e,f) $\xi_0 = 0.0826$ , $\delta_0 = 0.46$ .....	44
Figure 3-1: The structured mesh of the 2D domain. ....	49

Figure 3-2: Phase plane of the lift coefficient, lift coefficient power spectrum and the $v$ -velocity first mode <i>chronos</i> for three oscillation amplitudes (a-c) $A/D = 0.0$ , (d-f) $A/D = 0.175$ and (g-i) $A/D = 0.5$ for $f_e/f_s = 1$ . .....	51
Figure 3-3: The velocity contours for oscillation amplitudes $A/D = 0.175$ for $f_e/f_s = 1$ over $T_b = 15T_e$ .....	52
Figure 3-4: The velocity contours for the stationary cylinder (a-c) and forced oscillation amplitudes $A/D = 0.5$ (d-f) for $f_e/f_s = 1$ over two oscillation period. ....	53
Figure 3-5: Phase plane of the lift coefficient, lift coefficient power spectrum and the $v$ -velocity first mode <i>chronos</i> for (a-c) $A/D = 0.05$ , (d-f) $A/D = 0.175$ and (g-i) $A/D = 0.5$ for $f_e/f_s = 1.5$ . ..	54
Figure 3-6: Velocity contours for (a-c) $A/D = 0.05$ , (d-f) $A/D = 0.175$ and (g-i) $A/D = 0.5$ for $f_e/f_s = 1.5$ over two oscillation period. ....	55
Figure 3-7: Phase plane, power spectrum of the lift coefficient and the $v$ -velocity first mode <i>chronos</i> for (a-c) $A/D = 0.05$ , (d-f) $A/D = 0.175$ and (g-i) $A/D = 0.5$ , for $f_e/f_s = 2$ . ....	56
Figure 3-8: Velocity contours with forced oscillation amplitudes (a-c) $A/D = 0.05$ (d-f) $A/D = 0.175$ over two oscillation period and (g-i) $A/D = 0.5$ every oscillation period for $f_e/f_s = 2$ . ....	57
Figure 3-9: The equivorticity contours with frequency ratio (a-c) $f_e/f_s = 1$ (d-f) $f_e/f_s = 1.5$ and (g-i) $f_e/f_s = 2$ for oscillation amplitudes ranging from 0-0.5. ....	58
Figure 3-10: The $v$ -velocity contours with frequency ratios (a-c) $f_e/f_s = 1$ (d-f) $f_e/f_s = 1.5$ and (g-i) $f_e/f_s = 2$ for oscillation amplitudes ranging from 0-0.5. ....	58
Figure 3-11: (a) The <i>chronos</i> of modes S and K from CFD, (b) Deduced S and K modes approximated from the least square method of the dominant <i>chronos</i> data. ....	63
Figure 3-12: Quasi-periodic state of modes S and K at $\xi_0 = 0.0836$ and $\delta_0 = 0.29$ .....	63
Figure 3-13: Quasi-periodic state of modes S and K at $\xi_0 = 0.0826$ and $\delta_0 = 0.46$ .....	63
Figure 3-14: Complex amplitude of bifurcated mode S at $\xi_0 = 0.0826$ , $\delta_0 = 0.46$ . ....	64
Figure 3-15: Complex amplitude of bifurcated mode K at $\xi_0 = 0.0826$ , $\delta_0 = 0.46$ . ....	64
Figure 3-16: Quasi-periodic state of modes S and K at $\xi_0 = 0.0726$ , $\delta_0 = 0.26$ .....	65
Figure 3-17: steady bifurcated modes S and K at $\xi_0 = 0.001$ , $\gamma_0 = 0.0$ , $\alpha_0 = 0.018$ and $\delta_0 = 0.04$ .....	65

Figure 3-18: Complex amplitude of bifurcated mode S at $\xi_0 = 0.0726$ , $\delta_0 = 0.26$ .....	65
Figure 3-19: Complex amplitude of bifurcated mode K at $\xi_0 = 0.0726$ , $\delta_0 = 0.26$ .....	65
Figure 3-20: Steady bifurcated S and K modes at $\xi_0 = -0.0606$ , $\delta_0 = 0.17$ .....	66
Figure 4-1: (a) Schematic of the mesh for 2D domain, (b) Schematic of the mesh for 3D domain.....	71
Figure 4-2: The spectra of the lift and drag coefficients for (a) 2D simulation, (b) 3D simulation.....	74
Figure 4-3: Time series, power spectrum and phase plane of the fluctuating lift coefficient at $Re=200$ for three cases (a-c) $A/D = 0.0$ (d-f) $A/D = 0.175$ and $A/D = 0.5$ with $f_c/f_s = 1$ .....	75
Figure 4-4: Spatio-temporal structure of the 2D POD modes in terms of the $v$ -velocity streamlines with their corresponding <i>chronos</i> values for stationary cylinder case, (a,b) first mode, (c,d) second mode.....	76
Figure 4-5: Spatial structure of the first three pairs of the 3D POD modes with their corresponding <i>chronos</i> values for stationary cylinder case, (a-c) first pair (d-f) second pair and (g-i) third pair.....	77
Figure 4-6: Singular values of the transverse velocity deduced for fixed cylinder case, (a) from 2D POD analysis, (b) from 3D POD analysis.....	78
Figure 4-7: Spatio-temporal structure of the 2D POD modes in terms of the $v$ -velocity streamlines with their corresponding <i>chronos</i> values for $A/D=0.175$ . (a,b) first mode, (c,d) second mode.....	79
Figure 4-8: Spatial structure of the first three pairs of the 3D POD modes with their corresponding <i>chronos</i> values for $A/D=0.175$ , (a-c) first pair (d-f) second pair and (g-i) third pair. ....	80
Figure 4-9: (a) Singular values of the transverse velocity deduced for $A/D=0.5$ (a) from 2D POD analysis, (b) from 3D POD analysis.....	80
Figure 4-10: Spatio-temporal structure of the 2D POD modes in terms of the $v$ -velocity streamlines with their corresponding <i>chronos</i> values for $A/D=0.5$ , (a,b) first mode, (c,d) second mode.....	81
Figure 4-11: Spatial structure of the first three pairs of the 3D POD modes with their corresponding <i>chronos</i> values for $A/D=0.5$ , (a-c) first pair, (d-f) second pair and (g-i) third pair. ....	82
Figure 4-12: The $v$ -velocity contours for $A/D=0.175$ with $f_c/f_s = 1$ for (a-d) $t = t_0, t = t_0 + T_c, t = t_0 + 2T_c$ and $T_b = 15T_c$ .....	83



Figure 4-13: (a-c) The transverse velocity contours with $f_e/f_s = 1$ over two oscillation periods for (a-c) stationary cylinder, (d-f) $A/D=0.5$ .....	83
Figure 4-14: Reconstruction of $v$ -velocity field for oscillation amplitudes $A/D=0.0$ , $A/D=0.175$ and $A/D=0.5$ (a-c) using two first modes of the 2D POD (d-f) using four eigenmodes of the 3D POD.....	84

## LIST OF ABBREVIATIONS

$A/D$	Non-dimensional oscillation amplitude
$A, B$	Complex amplitudes of primary three-dimensional modes
$C_D, C_l$	Drag coefficient, lift coefficient
$D, d$	Diameter of the cylinder
$D_m(\kappa, 2\pi)$	Reflection symmetry
$J$	Jacobian matrix
$K(t), S(t)$	Time dependent amplitudes of mode K, S
$L$	Spanwise length
MTW	Modulated travelling wave
ODE	Ordinary differential equation
$O(2)$	Overall symmetry group of reflection and translation
$P$	Pair of vortices
POD	Proper orthogonal decomposition
$Re, Re_{cr}$	Reynolds number, critical Reynolds number
$[R]_{ijk}$	Time correlation tensor
$S$	Single vortex
$SO(2)$	Translation symmetry
$\widetilde{SO}(2)$	Combination of phase-shift and translation symmetry
$S(t), K(t)$	Temporal amplitudes of modes S and K
$St.$	Strouhal number
$S^1$	Phase-shift symmetry
SVD	Singular value decomposition
$T$	Translation symmetry operator
$T_b, T_e, T_s$	Beating period, oscillation period, shedding period
TW	travelling wave
$U$	Mean flow velocity
$V$	Transverse velocity vector
VIV	Vortex induced vibration

$X$	Space variable
$Z_2(\kappa, \pi)$	Spatio-temporal reflection symmetry
$a_k$	<i>Chronos</i>
$f(y), g(y)$	Spatial eigenfunction of mode S and K
$fD/U$	Non-dimensional frequency
$f_e$	Forcing frequency
$f_s$	Shedding frequency
$f_v$	Non-dimensional natural shedding frequency
$m/n$	Forcing to shedding frequency ratio
$p(a, b, c), q(a, b, c)$ $r(a, b, c), s(a, b, c)$	Polynomials based on invariant functions
$q, r$	Real part of mode S, K oscillation amplitudes
$u, v, w$	Velocity components in $x, y$ and $z$ directions
$v', v_m$	$v$ -velocity perturbation component, mean $v$ -velocity component
$x + iy, z + ih$	Complex Cartesian forms of mode S and K
$\kappa$	Reflection symmetry operator
$\varphi, \psi, \theta$	Imaginary parts of modes S and K oscillation amplitudes, phase difference
$\alpha_1^A, \alpha_1^B, \alpha_2^A$	Real cubic Landau coefficients for modes A and B, real quintic coefficient for mode A from the Sheard study
$c_1^A, c_1^B, c_2^A$	Complex cubic Landau coefficients for modes A and B, complex quintic coefficient for mode A from the Sheard study
$\delta_{core}, \delta_{shearlayer}$	Vortex core size, thickness of shear layer
$\delta_0, \xi_0$	Bifurcation parameters
$\varepsilon$	Bifurcation parameter
$\gamma_1^A, \gamma_1^B$	Coupling coefficients from the Sheard study
$\lambda$	Wavelength

$\mu$	Floquet multiplier
$\sigma$	Growth rate
$\sigma^A + i\omega^A$	Floquet exponent
$\xi_j + i\gamma_j; j = 0, 2$	Linear and cubic complex Landau coefficients for mode S
$\alpha_k + i\delta_k; k = 0, 1$	Linear and cubic complex Landau coefficients for mode K
$\xi_r + i\gamma_r; r = 1, 3$	Complex coupling coefficients for mode S
$\eta_j + i\kappa_j; j = 0, 1, 2, 3$	
$\alpha_n + i\delta_n; n = 2, 3$	Complex coupling coefficients for mode K
$\beta_p + i\mu_p; p = 0, 1, 2, 3$	
$\Psi_k$	<i>Topos</i>
$\tau$	Period
$\omega$	Angular velocity
2D, 3D	Two-dimensional, three-dimensional

**LIST OF APPENDICES**

APPENDIX A – MATHEMATICAL FORMULATION OF POD.....	99
APPENDIX B– INTRODUCTION TO BIFURCATION AND LINEAR STABILITY ANALYSIS .....	103
APPENDIX C – INVARIANT AND EQUIVARIANT DERIVATION .....	112

## INTRODUCTION

The flow past a circular cylinder has been studied extensively due to its practical importance in engineering and fundamental significance in fluid mechanics. The vortex shedding induces forces that may result in transverse and inline oscillations. This phenomenon is known as vortex induced vibration (VIV). VIV occurs in a large variety of engineering fields such as civil and mechanical engineering where cylindrical structures are commonly used. Examples are undersea pipelines, drilling risers, transmission lines and suspension bridges cables exposed to ocean or wind currents. If the vortex shedding frequency is close to the natural frequency of the structure, the resulting resonance can generate large amplitude oscillations causing structural failure. The stresses acting on the pipes due to the vibrations lead to accumulation of fatigue damage. On the scientific side, different physical phenomena, such as flow separation, vortex shedding, pattern formation, resonance and chaos are observed in the flow around a circular cylinder. Thus an accurate understanding of the physics of VIV is needed.

The inline vibration frequency is twice the cross flow frequency, which means that the number of stress cycles due to inline oscillation is double the number for transverse oscillation. The inline vibrations are also initiated at lower velocity. Thus, the inline oscillation fatigue damage and its effect on the cross flow motion and hence fatigue damage in transverse direction, are the motivations to study the pure inline VIV phenomena by forced streamwise excitation.

### Objectives

The goal of the present work is to use the equivariant bifurcation, normal form and stability theories coupled with numerical simulations to study the wake flow dynamics. Computational simulations of the wake flow subjected to inline cylinder motion are employed to obtain physical insight into the mechanisms responsible for the various pattern formations bifurcated from the combination of varying frequency and amplitude of vibration. The objectives are achieved in three phases. The first is the harmonic excitation of the wake flow at  $Re=200$  and stability analysis to determine the bifurcations and transitions of the wake associated with the inline excitation. A reduced order model of the  $v$ -velocity calculated from POD modes is used to develop the modal amplitude equations using equivariant bifurcation theory. The model serves to predict the sequence of bifurcation corresponding to the inline oscillation. In the second phase, the investigations have

been performed on the wake patterns and a map of the lift coefficient dynamics for combination of oscillation amplitude and super non-harmonic and harmonic forcing frequency ratios at  $Re=200$ . The set of bifurcations are predicted by the analytical model proposed in the first phase. This helps to understand how inline oscillation influences the wake dynamics.

In the third phase, to ensure that the results of the two-dimensional simulations are reliable, three dimensional simulations are carried out for flow at  $Re=200$  and proper orthogonal decomposition performed to find the primary modes and their transition due to the forced oscillation. The results confirm the validity of the 2D investigations.

## **Outline of the dissertation**

As previously mentioned, the approach used in this work aimed at understanding the fluid-structure interaction by controlling the motion of the cylinder, allowing the wake response to be examined separately. The forced oscillation results provide insights useful in the prediction of the motion of the free oscillating cylinder. The results exhibit the hydrodynamic forces acting on the cylinder for combinations of oscillation amplitudes and frequencies in the regime where pure inline VIV is encountered. This chapter contains the objectives and outline of the work. Chapter 1 gives some background information on the phenomenon of vortex shedding, its importance in fluid-structure interaction and vortex induced vibration. The different vortex shedding patterns generated corresponding to the parameters such as Reynolds number for free vibration and forcing frequency ratio, oscillation amplitude for forced vibrations are described. Chapter 1 also gives an overview of the works related to the forced vibration of the circular cylinder and studies of the deduced patterns considering their symmetry properties for both the inline and cross flow excited vibrations.

In the first paper presented in Chapter 2, two-dimensional simulations of the wake flow for periodic inlet flow representing harmonic excitation are carried out to compute the velocity and pressure fields. The infinite-cylinder approximation and periodic boundary conditions are the assumptions considered in solving the nonlinear Navier-Stokes equations for the unsteady 2D model of forced excitation. Since the Navier-Stokes equations are nonlinear and complex, the proper orthogonal decomposition (POD) tool is used to determine the minimum degrees-of-freedom (or modes) required to represent the flow field. The dominant modes calculated by POD-Galerkin-projection of the transverse velocity field are used to obtain a system of ordinary differential equations (ODE) in time. The amplitude and frequency variation cause formation of various vortex patterns. These

patterns have unique symmetry properties. The symmetries of the vortex shedding patterns play an important role in the analysis of the nonlinear dynamics that has been observed, including different solution branches formed due to the varying amplitude and frequency of the oscillation. The symmetry of observed patterns is applied to the governing equations of the system that produce them. The dominant  $v$ -velocity modes with corresponding symmetric spatial eigenfunctions representing the wake dynamics are used to develop the modal amplitude equations through symmetry-equivariant theory. The low order amplitude equations can have different solution branches with less symmetry than the symmetry of the original equations with respect to the bifurcation parameter values. This type of bifurcation with symmetries is known as symmetry-breaking. More precisely, the equivariant bifurcation theory is applied to classify solutions with respect to their symmetries. Finally, the linear stability analysis of the proposed model is performed in Poincare space and the set of bifurcations due to the bifurcation parameter variation are also investigated in the Argand plot of the Floquet multipliers.

The results of the second paper are presented in Chapter 3. This chapter contains the various vortex shedding patterns that are observed for the combination of oscillation amplitudes and forcing frequency ratios. The oscillation amplitude variation with frequency ratio changes at fixed Reynolds number cover the motion parameter space responsible for different patterns. The magnitude of the lift coefficient can be investigated to describe the changes of the force related to the pattern switching caused by the streamwise motion of the cylinder. The presence of higher harmonics of the lift coefficient during harmonic excitation and the reduction of the lift coefficient magnitude in the forced superharmonic oscillation by switching from asymmetric to symmetric patterns are also reported in the second paper. Applying the equivariant bifurcation theory to the proposed model corresponding to determining the different wake configurations and bifurcations is also outlined. In general, different possible solutions can emerge from the homogenous state with respect to the symmetries of the model. The bifurcation analysis is applied to the newly developed analytical model to study the mode competition and determine the types of bifurcations and wavenumber selection of the solution branches. The main findings from the comparison of the results of analytical model with CFD are presented.

The third paper contains 3D simulations of the wake flow presented in Chapter 4. The three-dimensional simulations are done to verify the 2D results. The reduced transverse velocity model



and power spectrum of the lift coefficient are used to analyze the wake dynamics and bifurcations occurring with respect to the cylinder inline oscillation. The results are validated by comparing with the obtained 2D numerical studies. It is shown in this chapter that the cylinder motion has a stabilization effect on the wake dynamics and delays the secondary transition to three-dimensional flow. Thus two-dimensional simulations are enough to model the temporal instability of the wake flow at  $Re=200$ . Chapter 5 draws the conclusions and presents some discussions on future research. The mathematical formulation of POD, introduction to bifurcation and linear stability analysis and derivation of the invariants and equivariant functions of the amplitude equations are presented in Appendices A, B and C.

## Chapter 1 LITERATURE REVIEW

### 1.1 The phenomenon of vortex shedding and flow regimes

Flow approaching a circular cylinder is forced to deviate from its uniform straight path to move around the cylinder. At very low Reynolds numbers, the flow is tangent to the surface of the cylinder and streamlines are symmetric. At  $Re < 4$ , the flow field is steady and known as creeping flow. As Reynolds number increases, inertia force effects increase in comparison to viscous forces. As the inner boundary layer has lower velocity, it is more sensitive to the pressure gradient and thus the stagnation or reverse flow starts from this region. The boundary layer separates due to the adverse pressure gradient generated because of the divergent geometry of the flow on the rear side of the cylinder. The vorticity in the boundary layer is fed into the shear layer forcing the latter to roll up into a vortex. Thus, the shear layer is formed as shown in Figure 1-1. In the same way, a vortex rotating in the opposite direction is formed on the other side of cylinder.

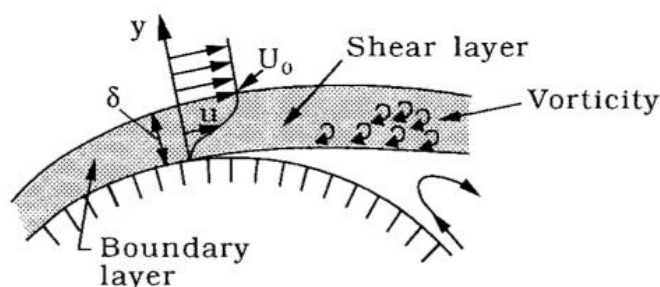


Figure 1-1: Flow separation structure (Sumer and Fredsøe, 2006).

For  $5 < Re < 40$ , the boundary layers separate on both sides of the cylinder and form vortices with opposite directions, however boundary layer remains laminar as shown in Fig 1-3(a). Beyond  $Re = 40$ , the kinetic energy of the flow is not high enough to overcome the downstream pressure field. The pair of vortices is unstable to small perturbations. One vortex therefore grows larger than the other and could draw the weak one across the wake as shown in Figure 1-2. The smaller vortex cuts off the larger vortex's boundary layer, which causes the larger vortex to be shed as a free vortex, which is convected downstream by a local flow velocity.

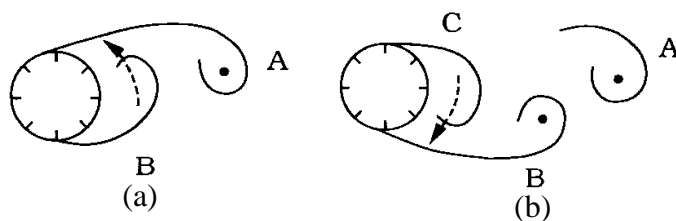


Figure 1-2: Vortex Shedding from sides of cylinder (Sumer and Fredsøe, 2006).

Following convection of the free vortex, a new vortex starts to form and this process continues periodically. The flow Hopf bifurcation to a time-periodic state in which the vortices shed on opposite sides of the cylinder periodically is the primary instability leading to the so called Karman wake. Both vortex street and boundary layer over the cylinder are laminar in this flow regime. In the laminar regime, the vortex shedding dynamics is similar to a simple harmonic oscillator. This regime was first modeled using the Landau equation showing the supercritical Hopf bifurcation leading to the Karman wake. The wake is two-dimensional for  $47 < \text{Re} < 190$ . The non-dimensional shedding frequency called the Strouhal number is defined as

$$St = \frac{f_v D}{U}, \quad (1.1)$$

$St$  is a function of Reynolds number for a fixed cylinder (Provansal et al., 1987a).

For  $200 < \text{Re} < 300$ , as shown in Figure 1-3(d), transition to turbulence starts in the wake region, although the boundary layer over the cylinder is completely laminar. Increasing Reynolds number causes this transition to move upstream (Bloor, 1964). For  $300 < \text{Re} < 3 \times 10^5$ , which is called the subcritical regime, the wake is completely turbulent, however, the boundary layer over the cylinder remains still laminar, as depicted in Figure 1-3(e). The reason being that the turbulence intensity is not strong enough to reach the separation point. Between  $3 \times 10^5 < \text{Re} < 3.5 \times 10^5$ , the transition point reaches the separation point, but perturbations remain weak on both sides of the cylinder. By increasing  $\text{Re}$ , transition starts from the separation point on one side of the cylinder and moves upstream over the cylinder toward the stagnation point. As the boundary layer separation point is turbulent on one side and laminar on the other, the flow regime becomes more asymmetric. This asymmetric flow regime causes the generated lift force to be asymmetric as well and so its direction changes alternately. This region shown in Figure 1-3(f) is called the critical regime.

The next flow regime where  $3 \times 10^5 < \text{Re} < 1.5 \times 10^6$  is called supercritical. In this region, as shown

in Figure 1-3(g), the boundary layer separation is completely turbulent on both sides of the cylinder, but transition to a turbulent boundary layer remains incomplete, so the turbulent transition region is located between the separation point and the stagnation point. The boundary layer in this case, is partly laminar and partly turbulent. The next regime in the region of  $1.5 \times 10^6 < Re < 4.5 \times 10^6$  is called the upper-transition regime. In this regime, as shown in Figure 1-3(h), turbulence penetrates in the boundary layer structure on one side of the cylinder completely, while on the other side it is partly laminar and partly turbulent.


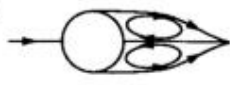







a)		No separation. Creeping flow	$Re < 5$
b)		A fixed pair of symmetric vortices	$5 < Re < 40$
c)		Laminar vortex street	$40 < Re < 200$
d)		Transition to turbulence in the wake	$200 < Re < 300$
e)		Wake completely turbulent. A: Laminar boundary layer separation	$300 < Re < 3 \times 10^5$  Subcritical
f)		A: Laminar boundary layer separation B: Turbulent boundary layer separation; but boundary layer laminar	$3 \times 10^5 < Re < 3.5 \times 10^5$ Critical (Lower transition)
g)		B: Turbulent boundary layer separation; the boundary layer partly laminar partly turbulent	$3.5 \times 10^5 < Re < 1.5 \times 10^6$  Supercritical
h)		C: Boundary layer comple- tely turbulent at one side	$1.5 \times 10^6 < Re < 4 \times 10^6$ Upper transition
i)		C: Boundary layer comple- tely turbulent at two sides	$4 \times 10^6 < Re$ Transcritical

Figure 1-3: Flow regimes over a smooth cylinder (Sumer and Fredsøe, 2006).

Finally at the region where  $Re > 4.5 \times 10^6$  the boundary layer over the cylinder becomes completely turbulent on both sides. This regime as shown in Fig 1-3(i) is called the transcritical regime (Roshko, 1961; Schewe, 1983).

## 1.2 Secondary instabilities in the wake

As mentioned above, for  $Re > 190$ , the wake becomes unstable to infinitesimal three-dimensional fluctuations and the vortices are no longer two-dimensional. This transition is known as a secondary instability and is the beginning of the route to turbulence in the wake. The limits of these instabilities were identified by discontinuities in the curve of Strouhal number versus Reynolds number of Figure 1-4 where different three-dimensional structures observed.

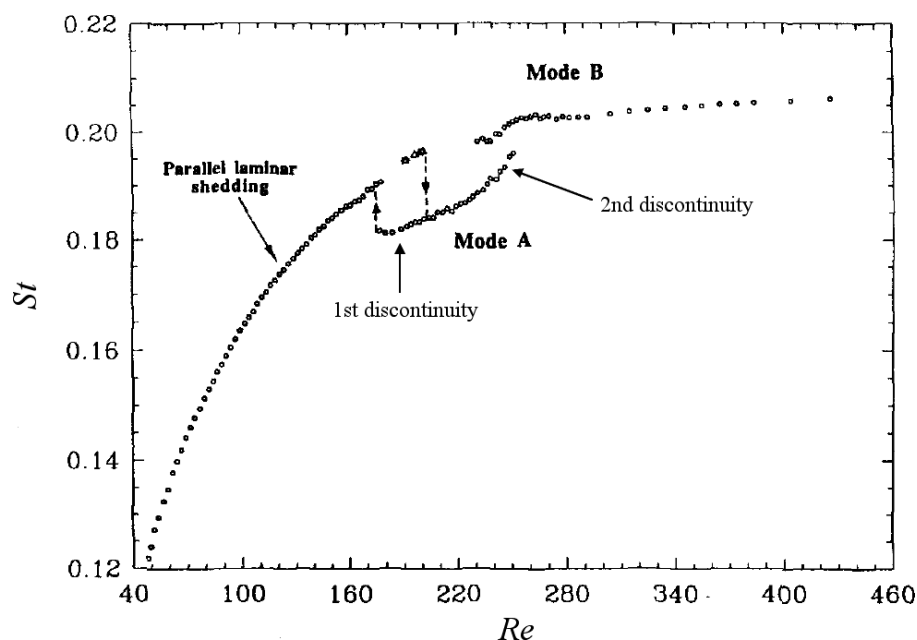


Figure 1-4: Experimental curve of Strouhal number vs. Reynolds number (Williamson, 1996).

The first mode, called A, undergoes subcritical bifurcation around Reynolds number 190 with spanwise wavelength 4 diameters. The second mode, called B, bifurcates through supercritical route around Reynolds number 260 with spanwise wavelength close to 1 diameter. The vortex dislocations were observed in the range of  $160 < Re < 230$  in conjunction with mode A. But once mode B structures started to develop in the wake, these dislocations disappeared. Thus, the discontinuities in the  $St$  versus  $Re$  plot correspond to the presence of different three-dimensional structures in the wake. Both modes A and B as shown in Figure 1-5 had distinct spatio-temporal symmetries.

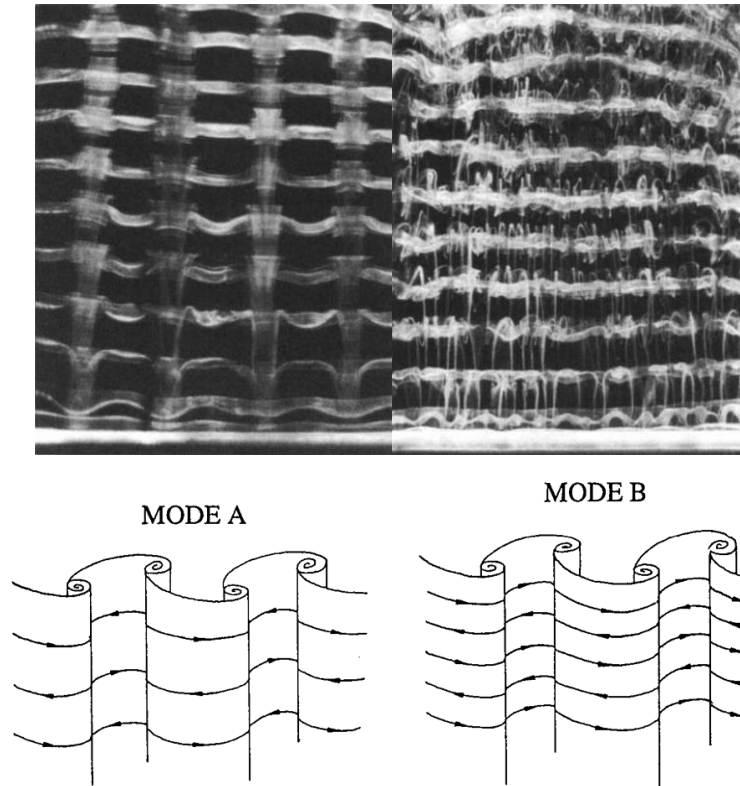


Figure 1-5: Flow visualization and sketch of symmetries of modes A and B (Leweke and Williamson, 1998; Williamson, 1996).

The nonlinear response of the wake around the cylinder to three-dimensional perturbations, which leads to the modes A and B with specific symmetry were observed in numerical computations given in Figure 1-5 and 1-6.

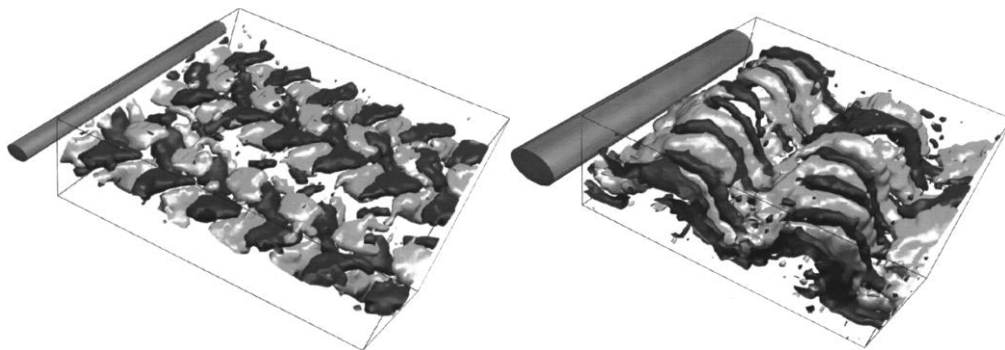


Figure 1-6: Iso-surfaces of streamwise vorticity obtained from PIV measurements showing the symmetries of modes A and B. Light grey surfaces represent the positive vorticity and dark grey represent negative vorticity (Leweke and Williamson, 1998).

The numerical stability analysis of the periodic wake of a circular cylinder was performed by Floquet theory using a Galerkin-projection to get the reduced order model of flow through the transition regime  $140 < \text{Re} < 300$ . The stability computations determine the structure of the critical eigenmode (Floquet mode) that drives the instability. The two-dimensional wake instability leading to the formation of critical Floquet mode corresponds to Mode A at  $\text{Re}=188.5$  was investigated. The second branch of modes called B which arises from the instability at  $\text{Re}= 259$  was predicted by the Floquet stability analysis (Barkley and Henderson, 1996). These results were supported by previous experiments (Brede et al., 1996). A simple phenomenological model based on the Landau and Ginzburg-Landau equations to describe the three-dimensional instabilities were also developed by Noack and Eckelman, (1994).

The base flow is a superposition of rotation and strain of the vortex cores as shown in Figure 1-7 where streamlines are ellipses. The flow is an exact solution of the Navier-Stokes equations. Then, two length-scales of the wake are the core size of Karman vortices and the width of the braids between the rollers shown in Figure 1-8. The ratio of vortex core size to shear layer thickness is equal to  $\delta_{\text{core}} / \delta_{\text{shear layer}} = \lambda_A / \lambda_B$ , which suggests that there may be a connection between the two wake feature and modes A and B. A perturbation of the flow displaces the center of rotation in the direction of maximum stretching and causes instability associated with mode A. There is also a stagnation point in the braid shear layer, which represents hyperbolic flow. In the braid region, the flow again results from superposition of rotation and strain, but contrary to the elliptic flow, the strain dominates over the rotation. In experiments, mode B vortex structures are observed in the hyperbolic flow region.

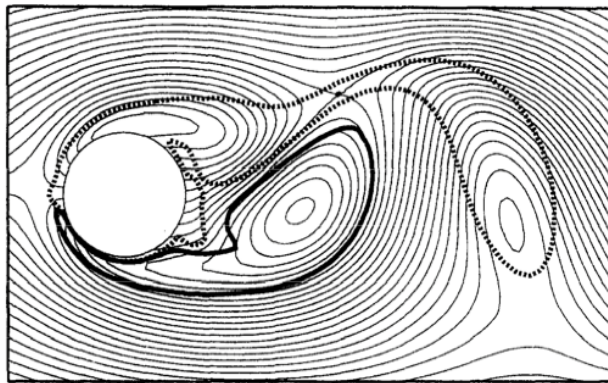


Figure 1-7: Streamline of the flow, shows elliptical shape of vortex core and also stagnation point in the flow (Leweke and Williamson, 1998; Williamson, 1996).

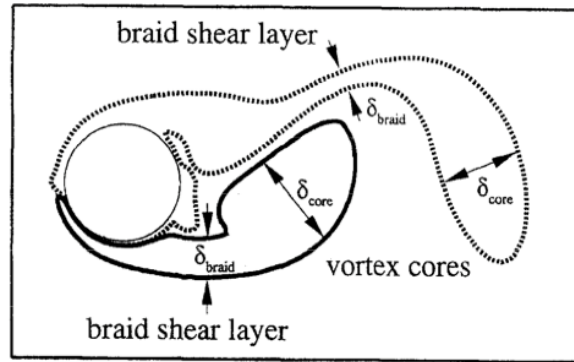


Figure 1-8: Spanwise vorticity of the 2-D wake flow at  $Re=200$  that shows flow features (Leweke and Williamson, 1998; Williamson, 1996).

Thus, mode A originates from an elliptical instability in the wake cores while mode B results from a hyperbolic instability in the braid shear layers. As shown in Figure 1-9 the spanwise-periodic deformation of the core vorticity causes streamwise stretching in the braid regions. Since the wake has spanwise vortices with opposite signs, the sign of the streamwise vorticity will also alternate. Therefore the resulting pattern has a different sign of streamwise vorticity on either side of the wake. This transition from two-dimensional wake to mode A is hysteretic.

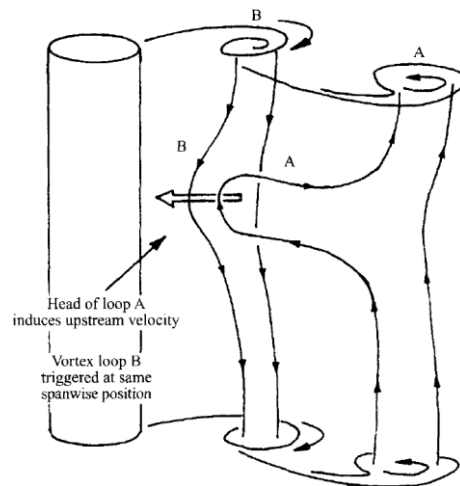


Figure 1-9: Physical mechanism of mode A vortex loops production (Carmo, 2009).

The streamwise vorticity of mode B generated at a given cycle induces waviness at the subsequent shear layer due to the Biot-Savart induction as shown in Figure 1-10. This waviness is combined with the strain field to form additional streamwise vorticity in phase with that generating the waviness; Thus the streamwise vortex from a previous braid has the same sign as the vortex in the



subsequent braid. This determines the symmetry of mode B shown in Figure 1-5.

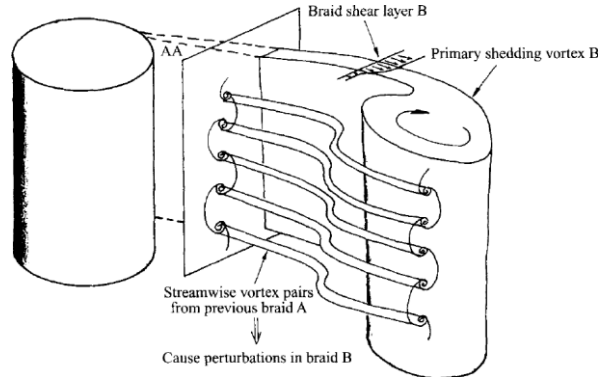


Figure 1-10: Physical mechanism of mode B streamwise vortices formation in the braid shear layer (Carmo, 2009).

The transition from two-dimensional to three-dimensional states due to the secondary instabilities can be modeled by combination of two self-excited global modes. The flow velocity perturbations  $u(x, t)$  can then be expressed as

$$u(x, t) = U(t)\varphi_0(x, t) + A(t)\varphi_1(x, t) \quad (1.2)$$

where  $\varphi_0$  is the primary and  $\varphi_1$  is the secondary instability mode. Both  $\varphi_0$  and  $\varphi_1$  are assumed to be time periodic with unit norm. The time-dependent amplitudes are given by  $U(t)$  and  $A(t)$ . The primary instability mode  $\varphi_0$  is assumed to be at a finite-amplitude  $|U_0|$  and the amplitude of the secondary instability is given by  $A(t) \propto e^{\sigma t}$  where  $\sigma$  is the growth rate. When  $\sigma < 0$  the flow is linearly stable and for  $\sigma = 0$  the instability starts. The energy transfer from two-dimensional primary mode to mode A is deduced directly from the nonlinear form of the Navier-Stokes equations.

$$U_n = U_0 - \sum_{j=1}^{\infty} \alpha_{0j} A_n^{2j} \quad (1.3)$$

where  $A_n$  is the amplitude of the secondary mode A, and  $U_0$  is the amplitude of the primary mode of the two-dimensional wake. The evolution of  $A_n$  near the linear instability can be expressed as  $A_{n+1} = \mu_1 A_n$ , where  $\mu_1 = \exp(\sigma T_n)$  is the linear growth rate and  $T_n$  is the length of period number  $n$ . The saturated amplitude and frequency relation of mode A are calculated from

$$A_{n+1} = (\mu_1 - \sum_{j=1}^{\infty} \alpha_{1j} A_n^{2j}) A_n \quad (1.4(a))$$

$$f_n = f_0 - \sum_{j=1}^{\infty} \gamma_{0j} A_n^{2j} \quad (1.4(b))$$

The coefficients are function of the bifurcation parameter  $\epsilon = (Re - Re_{cr}) / Re_{cr}$  where  $Re_{cr}$  is the critical Reynolds number for the onset of vortex shedding. Near the threshold the linear growth rate is approximately  $\mu_1 = 1 + \frac{d\mu_1}{d\epsilon} \epsilon$ . In this regime  $\alpha_{1j}$  is assumed constant since their variations are  $O(\epsilon^2)$ . Negative  $\alpha_{11}$  leads to a subcritical bifurcation of mode A. At  $Re=260$  and spanwise length of  $L = 0.822d$ , the other secondary instability mode B is formed via supercritical bifurcation with no frequency shift. The regions of instability for modes A and B are presented in Figure 1-11. There is a good agreement between computations based on linear theory and experimental measurements of the critical Reynolds number and wavelength (Barkley and Henderson, 1996; Williamson, 1996).

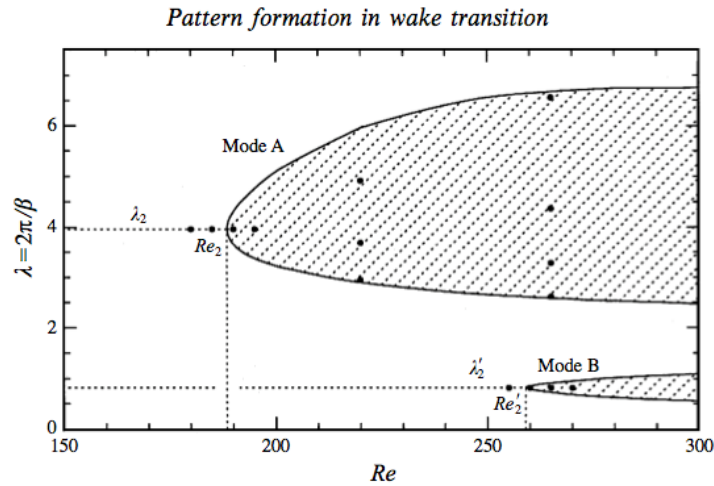


Figure 1-11: Curves of Neutral stability for 2-D Karman vortex with respect to spanwise perturbations. Upper region relates to long-wavelength instabilities starts at  $Re=190$ , lower region corresponds to short-wavelength, initiated at  $Re=260$  (Barkley and Henderson, 1996).

The nonlinear interaction between modes A and B was studied as a possible scenario for the bifurcation to three-dimensional flow in the wake of a circular cylinder for Reynolds number up to 300. This scenario was based on the amplitude equations. The amplitude equations were developed

based on the Landau equation by considering the symmetries of mode A and B. The A and B modes symmetries are

$$\begin{aligned} u_A(x, y, z, t) &= u_A(x, -y, z, t + T/2), \\ v_A(x, y, z, t) &= -v_A(x, -y, z, t + T/2), \\ w_A(x, y, z, t) &= w_A(x, -y, z, t + T/2). \end{aligned} \quad (1.5(a))$$

$$\begin{aligned} u_B(x, y, z, t) &= u_B(x, -y, z + \lambda^B/2, t + T/2), \\ v_B(x, y, z, t) &= -v_B(x, -y, z + \lambda^B/2, t + T/2), \\ w_B(x, y, z, t) &= w_B(x, -y, z + \lambda^B/2, t + T/2). \end{aligned} \quad (1.5(b))$$

Thus, mode A has the spatio-temporal symmetry consisting of reflection symmetry with evolution of half a period while mode B is invariant under the combination of reflection in  $y$ , translation in  $z$  by  $1 = \lambda^B/2$  and evolution of half a period. Assuming that there exist a point both modes occur simultaneously, together with the wavelength ratio of A and B modes and their symmetries, the general form of the amplitude equations can be obtained. Invariants<sup>1</sup> and equivariants<sup>2</sup> satisfying the symmetry properties of interaction of mode A and B are defined. The general evolution equation is

$$A_{n+1} = p(a, b, c)A_n + q(a, b, c)\overline{A_n}^{2m-1}B_n^2 \quad (1.6(a))$$

$$B_{n+1} = r(a, b, c)B_n + s(a, b, c)A_n^{2m}\overline{B_n} \quad (1.6(b))$$

where  $p, q, r$  and  $s$  are arbitrary real polynomial functions including invariants. The general form of the equations truncated to third order as

$$A_{n+1} = \mu^A A_n + \alpha_1^A |A_n|^2 A_n + \gamma_1^A |B_n|^2 A_n \quad (1.7(a))$$

$$B_{n+1} = \mu^B B_n + \alpha_1^B |B_n|^2 B_n + \gamma_1^B |A_n|^2 B_n \quad (1.7(b))$$

The Floquet multipliers  $\mu^A$  and  $\mu^B$  are obtained from linear relations

---

<sup>1</sup> Invariant: a property of a class of mathematical objects that remains unchanged when transformations of a certain type are applied to the objects.

<sup>2</sup> Equivariant: In mathematics, an equivariant map is a function between two sets that commutes with the action of a group.

$$\mu^A(Re) = 1 + 0.0091(Re - 189) \quad (1.8(a))$$

$$\mu^B(Re) = 1 + 0.021(Re - 259) \quad (1.8(b))$$

By knowing the Floquet multipliers, the Landau coefficients can be determined from the direct numerical computations. Linearizing equation (1.7(b)) about  $B_n = 0$ , the coupling coefficient  $\gamma_1^B$  can be calculated. The coupling term  $\gamma_1^A$  in the absence of mode A,  $A_n = 0$  is calculated in the similar way. The model represented the destabilizing effect of mode A on mode B and stabilizing effect of mode B on mode A. The existence of mode B below the linear instability  $Re=259$  and the energy shift between modes over a range of Reynolds number were also predicted. The low order nonlinear modes interaction model considers amplitude effects, so phase of the modes are not considered in interaction phenomenon and assumed to be fixed; however, results have a good agreement with experiments, showing that the dynamics of the mode amplitudes have main role in mode interaction as shown in Figure 1-12 (Barkley et al., 2000).

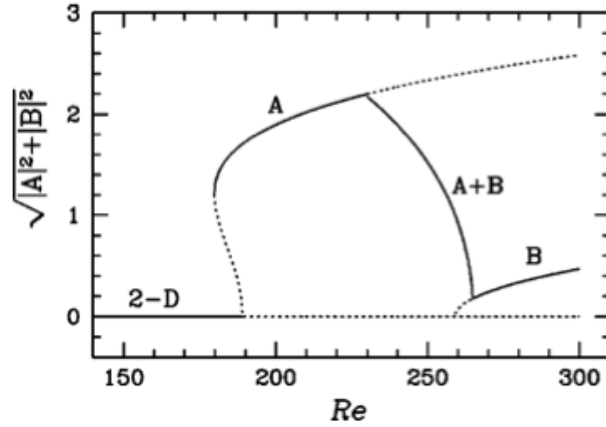


Figure 1-12: Bifurcation diagram of amplitude equations, Solid lines indicate stable states and dash lines transition case of A, B and A+B interaction case. 2-D branch has  $A=B=0$  (Barkley et al., 2000).

This model was later extended to predict the Strouhal-Reynolds number profile over the three-dimensional transition including the frequency information by adding the complex coefficients to the model.

$$\frac{dA}{dt} = [\sigma^A(Re) + i\omega^A]A + \alpha_1^A(1 + ic_1^A)|A|^2 A + \gamma_1^A(1 + id_1^A)|B|^2 A + \alpha_2^A(1 + ic_2^A)|A|^4 A \quad (1.9(a))$$

$$\frac{dB}{dt} = \left[ \sigma^B (Re) + i\omega^B \right] B + \alpha_1^B (1 + ic_1^B) |B|^2 B + \gamma_1^B (1 + id_1^B) |A|^2 B \quad (1.9(b))$$

where  $A$  is the complex amplitude of the perturbation and  $\sigma^A (Re) + i\omega^A$  is the eigenvalue obtained from the linear stability analysis, called a Floquet exponent. The lower order coefficients of the equations were calculated from three-dimensional numerical simulations, whereas the higher order coefficients were taken from experimental data using the method of Barkely. This model accurately predicts the discontinuous nature of the curve of  $St.$  versus  $Re$  plotted in Figure 1-4. The shedding frequencies of both modes are well predicted by the model for  $Re \leq 260$ . For higher Reynolds number, the Strouhal number observed in experiments differs from the predicted one by this model, probably due to the longer spanwise instabilities that lower the shedding frequency value (Sheard et al., 2003).

### 1.3 VIV and flow pattern properties

As noted above, the anti-symmetric vortex shedding induced by destabilizing the wake, causes the velocity and pressure perturbations around the cylinder, which generate forces in the inline -drag- and transverse directions – lift. When vortices are shed in the wake, the lift forcing frequency equals the frequency of vortex shedding. This is expected since from each side of the cylinder one vortex is shed once per cycle while the drag frequency is twice the frequency of the lift force since the vortices induce identical perturbations in the drag direction. Due to the existence of these forces imposed by the vortex shedding of the flow, the cylinder vibrates. This vibration, which is the structural response, is called vortex-induced vibration (VIV). Since the movement of the cylinder alters the flow field and the flow field is in turn responsible for the forces exerted on the cylinder, VIV is a strongly nonlinear phenomenon. When the fluid velocity increases, it reaches a range where the vortex shedding frequency approaches the natural frequency of the cylinder eventually leading to synchronization so called Lock-on.

Different regimes with specific symmetry properties exist for the flow behind the cylinder. For low Reynolds numbers the flow is steady and a Karman vortex street is formed, in which a single vortex is shed in each half a cycle and so is called the 2S mode. The 2S-mode of shedding, coupled with the cylinder motion where energy transfers between cylinder and flow may lead to an even more dynamic and organized motion with unique symmetry properties.

In the free vibration case, a small increase of flow speed leads to large changes in the cylinder oscillation amplitude accompanied by a change in the pattern of vortex shedding. This switching between modes and amplitude variation makes studying the free vibration a difficult problem. Understanding the fluid forces associated with VIV requires an understanding of the wake structure behind the cylinder. Thus, the forced oscillation study is an effective method for prediction of the free vibration dynamics by mapping the wake behind the cylinder. Forced excitation in the transverse direction leads to formation of different wake modes showing the relation between the cylinder controlled motion and the wake structure. The map shown in Figure 1-13 defines various wake patterns with respect to the amplitude of oscillations and reduced velocities. The 2S mode, as mentioned above, is the Karman vortex street. The 2P form represents a pair of vortices shed each half cycle and P+S is a state where a pair of vortices and a single one are shed each cycle (Williamson and Roshko, 1988). Changes in the phase of the lift force due to the cylinder motion results in a change in the direction or magnitude of the energy transfer which leads to a different mode shape (Blackburn and Henderson, 1999).

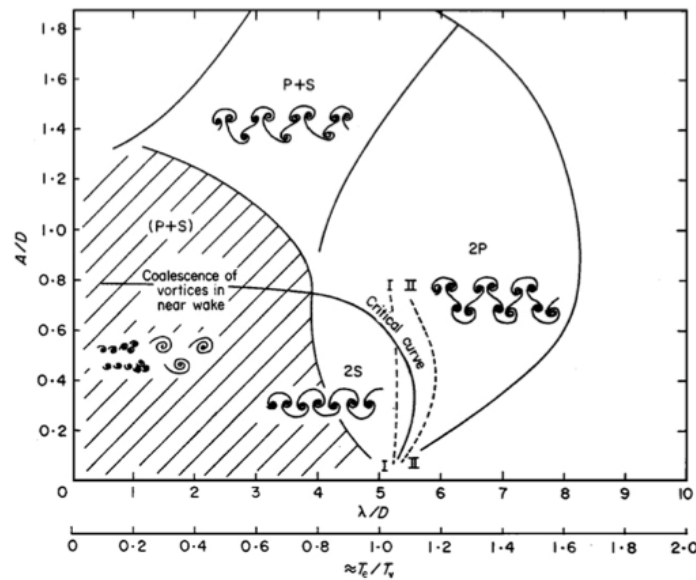


Figure 1-13: Different regimes for vortex wake modes showing the 2S, 2P, and P+S mode regimes at  $Re=1000$  (Williamson and Govardhan, 2008).

Streamwise excitation can also have a significant effect of the flow pattern. Since the drag fluctuation induced by the wake has a frequency twice that of the fluctuating lift, the streamwise oscillation has lower amplitude and higher frequency, which may cause a comparable impact on

the fatigue life of the structure. In some cases there is a phase shift between the vortex shedding and the structural motion which alters the level of energy transfer to and from the structure and may explain the pattern deduced from the mode competition.

The different flow patterns for the inline forced oscillations in the lock-on region describe the nonlinear behavior of the flow which is affected by the combination of  $A/D$  and  $f_e/f_s$ . The lock-on region covers the  $f_e/f_s$  and  $A/D$  ranges from 1.74 to 2.2 and 0.06 to 0.12, respectively. As a result of the various combinations of amplitude and frequency ratio one or more complex phenomena such as hysteresis, bifurcation and synchronization may occur leading to different flow patterns, similarly to the transverse forced oscillation case. The two different flow patterns corresponding to A-I and A-III modes were investigated. A-I consists of one row of single vortices and A-III one row of vortex pairs as shown in Figure 1-14 (Griffin and Ramberg, 1976).

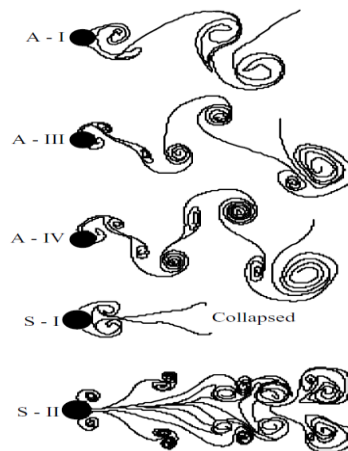


Figure 1-14: Typical flow structures of the streamwise forced flow (Griffin and Ramberg, 1976).

Later, flow patterns for  $A/D=0.5-0.67$  and  $f_e/f_s=0-3.1$  were observed and categorized in five modes as shown in Figure 1-14. These modes are designated as S-I, A-I, A-III and S-II (Ongoren and Rockwell, 1988). The dependence of the flow structure on frequency ratio and amplitude are presented in Figure 1-15. Apart from  $Re$ , initial conditions such as turbulence level, roughness of cylinder may affect the flow pattern.

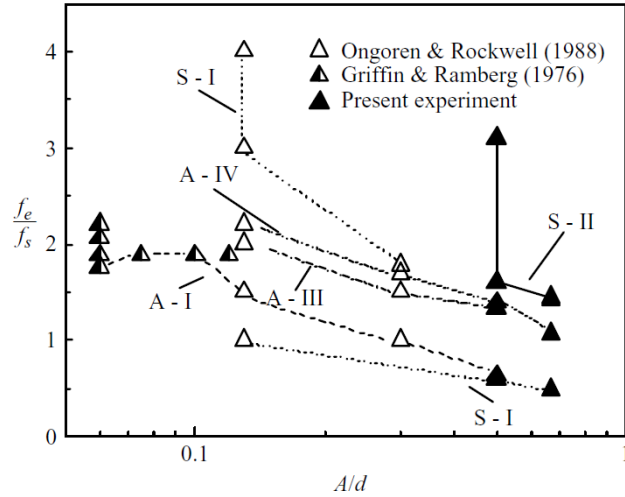


Figure 1-15: Flow structure dependence on  $f_e/f_s$  and  $A/D$  (Ongoren and Rockwell, 1988).

For forced inline oscillations, as the frequency of oscillation is increased with all other parameters remaining fixed, a transition from an antisymmetric to a symmetric flow pattern is observed. At higher forcing amplitudes, this transition regime is chaotic which results from a competition between antisymmetric and symmetric shedding modes. Later, quantitative inline oscillations at  $Re=190$ ,  $f_e/f_s=1.74-2.2$  and  $A/D=0.06-0.012$  were performed showing that the lock-on region widens with increasing  $A/D$  (Griffin and Ramberg, 1974).

Wake spatio-temporal symmetry is dependent on the forcing to natural shedding frequency ratio and amplitude of oscillation. Thus, symmetry plays an important role in the dynamics of the forced flow. Later, discrete low order amplitude equations based on the symmetry-equivariant theory were developed to explain the nonlinear dynamics of the wake mode interaction. The vortex-structure interaction was studied by introducing known perturbations with specific symmetry and investigating their effects on the wake dynamics. The evolution equation was defined by considering the symmetries of the two dominant modes. The first Karman shedding mode has spatio-temporal symmetry  $Z_2(\kappa, \pi)$  meaning that it is invariant for the combination of reflection with half a cycle translation while the second is the forcing mode with symmetry  $D_m(\kappa, 2\pi/m)$ , which is the combination of reflection and translation symmetry in wavelength. The required parameters of the low order model were determined from the POD decomposition of the temporal velocity field of the CFD results. A qualitative analysis of these equations at  $Re=200$



and 1000 predicted the expected bifurcations deduced from symmetry breaking such as period-doubling by changing the inline amplitude of the oscillation. It was also observed that a strong subharmonic lock-on occurs at the ratio where the forcing over vortex shedding frequency is in the range of  $1 < m/n < 2$ . Possible changes in the wake symmetry of harmonic forcing were supported by numerical and experimental results (Mureithi, 2003; Mureithi and Rodriguez, 2005).

**Chapter 2 ARTICLE 1: BIFURCATION AND STABILITY ANALYSIS  
WITH THE ROLE OF NORMAL FORM SYMMETRIES ON THE  
HARMONIC STREAMWISE FORCED OSCILLATION OF THE  
CYLINDER WAKE**

Nabatian N. and Mureithi N. W. (2014) submitted to “International Journal of bifurcation and chaos” in March 27, 2014.

**Abstract**

The vortex shedding over a cylinder is affected by the cylinder oscillation. The dynamics of the cylinder wake subjected to the harmonic inline oscillation is investigated in this work. 2D numerical computations are performed for  $Re=200$  to find the effect of inline oscillation amplitude on the vortex structure and flow pattern which lead to the variation of cylinder lift, drag and wake shedding Strouhal number. Two primary modes of the transverse velocity field are considered to model and predict the nonlinear interaction of 2D vortex shedding modes. The normal form symmetries have the main role in the pattern formation. The interaction of two steady modes in the presence of  $O(2) \times S^1$  symmetry is described by equivariant bifurcation theory. More precisely the equivariant bifurcation theory is applied to classify the solutions with respect to their symmetries. Considering the symmetries, the mode interaction amplitude equations are developed with the frequency saturation information included by the addition of complex coefficients. The present model is expanded up to 7th power, in order to include the spatio-temporal effects. The coefficients of the amplitude equations are obtained from 2D simulations of the cylinder wake flow.

The physical significant effect of the inline cylinder oscillation on the wake dynamics is captured by the variation of the two linear coefficients of the model. The model describes the development and interaction of the two primary modes of the forced excitation at different oscillation amplitudes. The bifurcation analysis of this model predicts the bifurcation sequences occur due to the variation of the two linear bifurcation parameters affected by cylinder oscillation. Similarly to the numerical results, as the amplitude of oscillation increases, two limit cycles of the model undergo the symmetry-breaking bifurcation leading to a quasi-periodic state. For  $A/D = 0.5$ , the

quasi-periodic state undergoes a torus doubling bifurcation. The dominant frequency of the bifurcated S mode matches the lift coefficient shedding frequency for  $A/D = 0.5$  obtained from the numerical computation. The modulated travelling waves bifurcated from the model have mode S as the basic  $v$ -velocity mode which verifies the symmetric period-doubled quasi-steady transverse velocity pattern observed in CFD simulation. The final part is a complete stability analysis of the coupled amplitude equations describing mode interaction in the Poincare map. The presented model can accurately predict the bifurcation sequence of the forced cylinder wake dynamic transitions investigated in the numerical results.

*Keywords:* Normal form symmetry; equivariant bifurcation theory; torus doubling bifurcation.

## 2.4 Introduction

The wake behind a cylinder is created via a Hopf bifurcation in the first instability region (Leweke and Williamson, 1998; Ryan et al., 2005; Williamson, 1996). The forces generated from vortex shedding can oscillate the structure. The amplitude oscillation usually excites the two primary modes of the wake. Two global modes can occur: a reflection symmetric mode in which the pair of vortices shed symmetrically and the Karman mode which has spatio-temporal symmetry. The symmetric mode is intrinsically unstable and is quickly replaced by Karman mode, unless it is stabilized by cylinder motion. The interaction between the vortex shedding and structure motion can lead to self-excited vibration of the cylinder and changing of the wake pattern. The wake pattern formation can be used to identify the global instabilities that develop in the wake behind a circular cylinder and follow its dynamics from simple to chaotic behavior. According to the complex dynamics of the fluid-structure interaction, the cylinder motion can be controlled to study the wake response to the prescribed motion.

Thus, the forced oscillation of the wake is an approach to study the cylinder oscillation effect on the wake pattern. The periodic vortex street created due to the wake instability is saturated. Thus, for Reynolds number not too far above the critical Reynolds number, the changes of the shedding frequency and  $Re$  are smooth, suggesting that linear Floquet instability theory is applicable for vortex shedding dynamic analysis (Barkley and Henderson, 1996; Ding et al., 2003; Park et al., 1994; Wooden and Sinha, 2007). The nonlinear interaction of the wake modes was modeled using Stuart-Landau equation by Provansal et al., (1987b). The Landau coefficients were calculated from

the 2D simulations (Le Gal et al., 2001).

To better understand the wake dynamics, Williamson and Roshko, (1988) excited the wake by external periodic forcing. This approach is the key to understanding the wake-structure interaction during vortex induced vibration (VIV). In experiments, the known transverse forced oscillation is subjected to the cylinder at different forcing amplitude and frequency ranges. Williamson and Roshko showed that the vortex shedding patterns are dependent on the forcing frequency, amplitude ( $A/D$ ), direction of oscillation and Reynolds number. Therefore, by changing each parameter different modes defined by their symmetries may be observed; the modes were labeled 2P, 2S, P+S and 2P+2S based on the number and combination of the vortices shed on the sides of the cylinder per forcing cycle. They also observed the transition from 2S to 2P mode which causes a half period shift between the cylinder motion and fluid forces (Lam et al., 2010; Lentini et al., 2006).

Barkley et al., (2000) proposed the equivariant bifurcation scenario for development of the coupled evolution amplitude equations describing the 3D wake mode interaction. The higher order terms may have some complicated spatio-temporal effects on dynamics, which were ignored in their model. Later, Sheard et al., (2003) expanded the amplitude equations by coupled Landau equations including frequency information by the addition of complex coefficients. The model predicts the nature of the Strouhal–Reynolds number profile of the circular cylinder wake at transition deduced from the interaction of 3D wake modes (Blackburn et al., 2004b; Blackburn et al., 2004c).

Mureithi et al., (2003) used the symmetry-equivariant theory to study the forced Karman wake. The nonlinear interaction of the Karman and symmetric mode is modeled by symmetry equivariant bifurcation theory in the form of a pair of low order discrete amplitude equations. A qualitative analysis of these equations shows that the Karman mode bifurcation is affected by the forced amplitude ratio. Both subharmonic and superharmonic excitations of the Karman wake were studied experimentally. A quantitative analysis was also done by numerical simulation of the 2D wake model. Mureithi and Rodriguez, (2005) performed CFD computations of the wake flow undergoing periodic excitation. The dominant modes were determined by proper orthogonal decomposition (POD) analysis (Borggaard et al., 2007; Cao et al., 2001; Konstantinidis et al., 2007; Noack et al., 2003; Rowley, 2005) and coefficients of the amplitude equations obtained. They observed the period doubling for the inline excitation as the dominant phenomena, which confirms

the Williamson experiment (Mureithi et al., 2010).

In the present work, the dynamics of the wake flow for  $Re=200$  when forced to oscillate in the inline direction at the vortex shedding frequency is studied by developing a model using the equivariant bifurcation theory. The coefficients of the amplitude equations are considered complex to include the frequency saturation and solved for higher orders to cover the spatio-temporal effects. The first two primary modes which exist for various oscillation amplitudes are employed to model the wake dynamics. The linear terms of the amplitude equations are affected by the variation of the streamwise oscillation and thus considered as the bifurcation parameters. The goal of this work is to find the sequence of bifurcations observed in CFD and previous experimental results through bifurcation analysis of the symmetry-based model.

## 2.5 Numerical computations

The two-dimensional flow over a circular cylinder under forced inline oscillation is simulated using ANSYS CFX. Simulations were done for  $Re=200$  at two dimensional domain given in Figure 2-1. The excitation frequency is equal to the natural shedding frequency and oscillation amplitude ratio varies from zero to  $0.5D$ . Convergence tests were performed for the fixed cylinder case and the measured force coefficients and Strouhal number were found to be in good agreement with the previous numerical and experimental results presented by Mureithi, (2005).

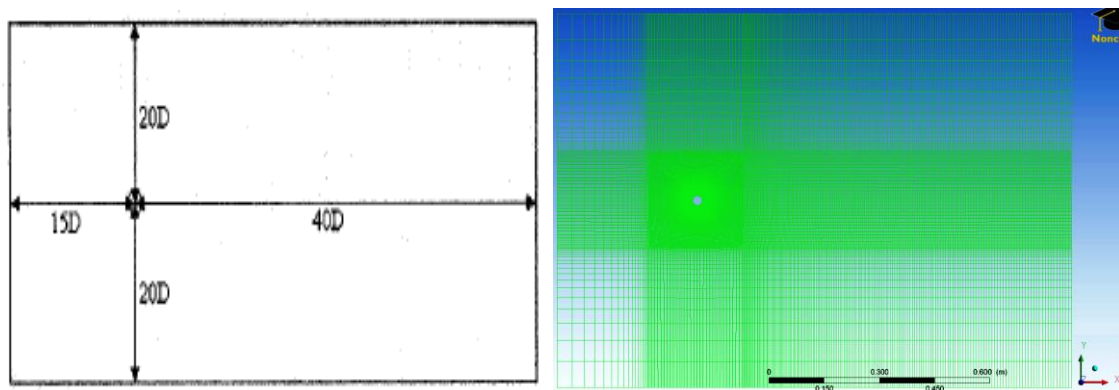


Figure 2-1: Schematic of 2D domain and structured mesh.

The forced vibration is implemented as a boundary condition instead of using a moving mesh. It is equivalent to setting a rigid cylinder in an oscillated flow field. The oscillating inlet flow is then  $u = U + A\omega\sin(\omega t)$ , where  $A$  is the amplitude of oscillation,  $\omega = 2\pi f_e$  is the oscillation frequency

with  $f_e/f_s = 1$  and  $u$  is the streamwise component of fluid velocity. The transverse velocity of the forced wake flow is stored in a matrix. The POD method is applied to analyze the recorded data of the  $v$ -velocity perturbations in 100 nodes on the line 10D downstream of the flow for 40 steady cycles. First, the mean value of each column is subtracted to find the velocity perturbation value as in Eq. (2.1) and the results are stored in the matrix A.

$$v'(y, t) = v(y, t) - v_m(y, t), \quad (2.1)$$

The perturbation velocity matrix can then be written as:

$$v'(y, t) = \sum_{k=1}^{100} a_k(t) \psi_k(y), \quad (2.2)$$

where each mode includes a spatial eigenvector  $\psi_k(y)$ , called *topos* and a temporal one  $a_k(t)$ , called *chronos*. The *chronos*  $a_k(t)$  describes each point time history velocity and  $\psi_k(y)$  represents the velocity profile of 100 points at a specific time. The matrix A (5500,100) for each case of the forced oscillation is reduced by singular value decomposition (SVD) to identify the *topos* and *chronos* of the primary modes in the following method. The different *topos* and *chronos* for various amplitudes of oscillation show different behaviors of the flow field, under the effect of cylinder oscillations. Since POD gives the normalized *topos*, *chronos* contains the amplitude evolution of the mode.

## 2.6 Numerical Solution and POD Modes

The eigenvalue spectrum of transverse velocity given in Figure 2-2 clearly shows that the first two modes contain 99% of the energy. Since the fluctuating  $v$ -velocity data is complex each dominant mode represents pair of similar patterns shifted spatially. Each pair mode represents a travelling wave corresponding to the convective nature of the flow. The singular values of Figure 2-3 related to the perturbed  $v$ -velocity for  $A/D = 0.5$  are still concentrated around the first two modes and these modes have similar spatial structures to those derived for the stationary cylinder.

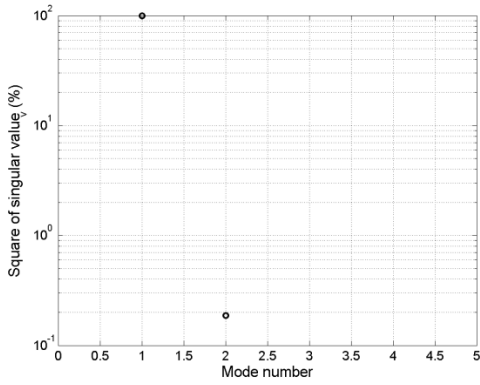


Figure 2-2: Singular values of  $v$ -velocity for stationary cylinder

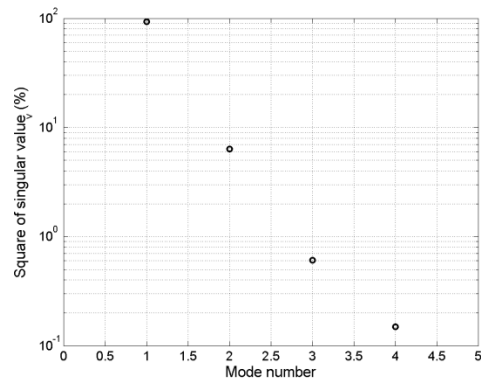


Figure 2-3: Singular values of  $v$ -velocity for oscillation amplitude  $A/D = 0.5$ .

The symmetry properties of each *topos* are utilized to identify each eigenmode clearly. As shown in Figure 2-4(a) the first mode *topos* is symmetric with the dominant frequency equal to the non-dimensional natural shedding frequency  $f_v$ , while Figure 2-4(c) represents the antisymmetric spatial pattern with the frequency  $2f_v$ .

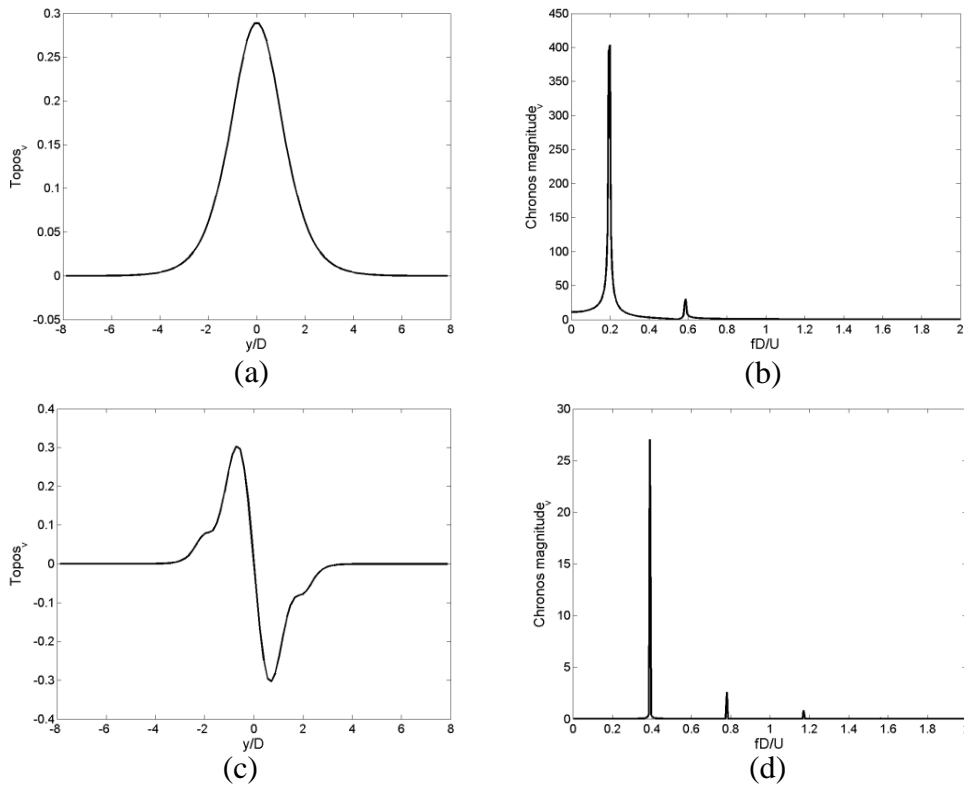


Figure 2-4: The spatial and temporal basic functions of two dominant modes for  $A/D = 0.0$ . (a) first *topos* (b) first *chronos* (c) second *topos* (d) second *chronos*.

For forcing amplitude  $A/D=0.15$ , the quasi periodic nature of both modes observed in Poincare plane of Figure 2-18(c) and 2-18(d) are also found in Figure 2-5(b) and 2-5(d) due to the existence of the other peaks in addition to  $f_v$  and  $2f_v$ . For the case of  $A/D=0.5$ , the torus state is then replaced by period-doubled torus where the dominant dimensionless frequency of the first symmetric mode becomes 0.1, same as the bifurcated lift coefficient frequency (see Figures 2-7(a)-2-7(d)).

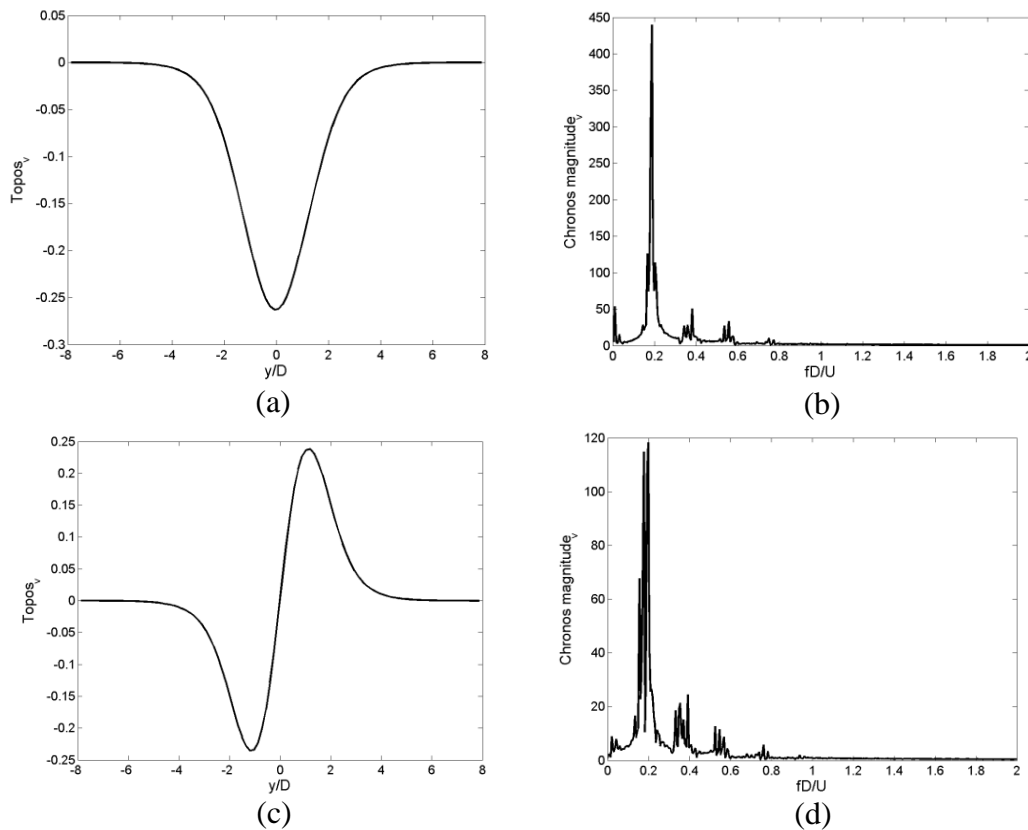
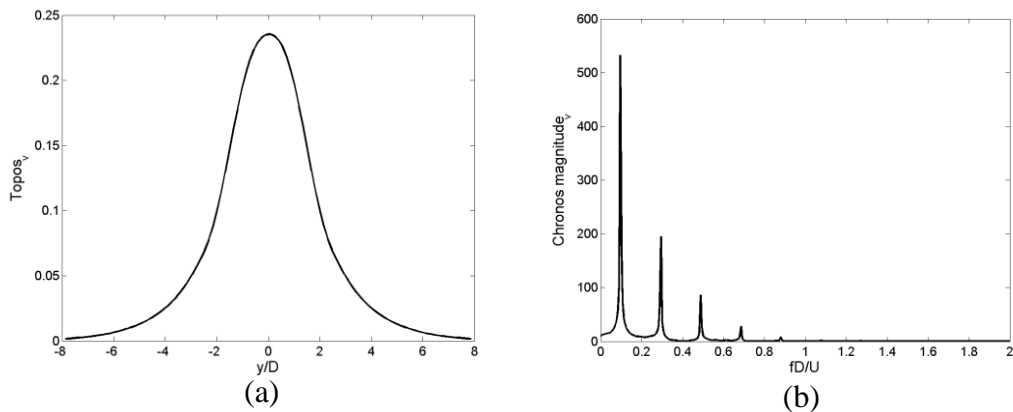


Figure 2-5: The spatial and temporal basic functions of two dominant modes for  $A/D=0.15$  (a)

first *topos* (b) first *chronos* (c) second *topos* (d) second *chronos*.





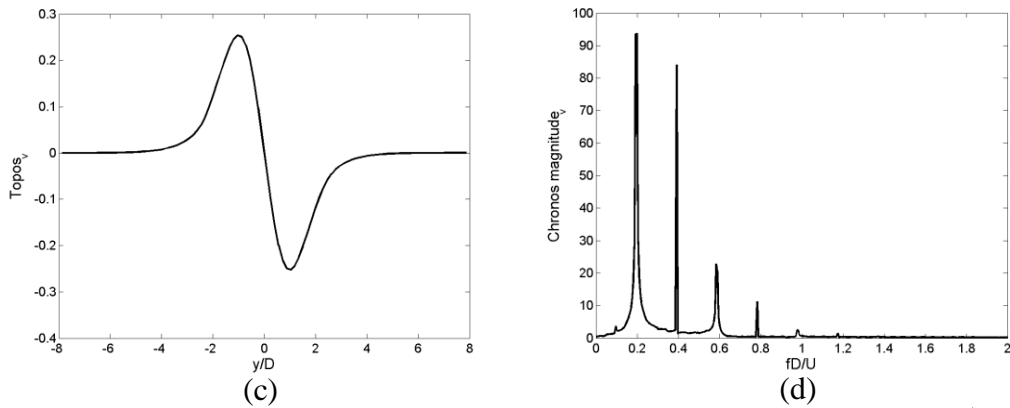


Figure 2-6: The spatial and temporal basic functions of two dominant modes for  $A/D = 0.35$  (a) first *topos* (b) first *chronos* (c) second *topos* (d) second *chronos*.

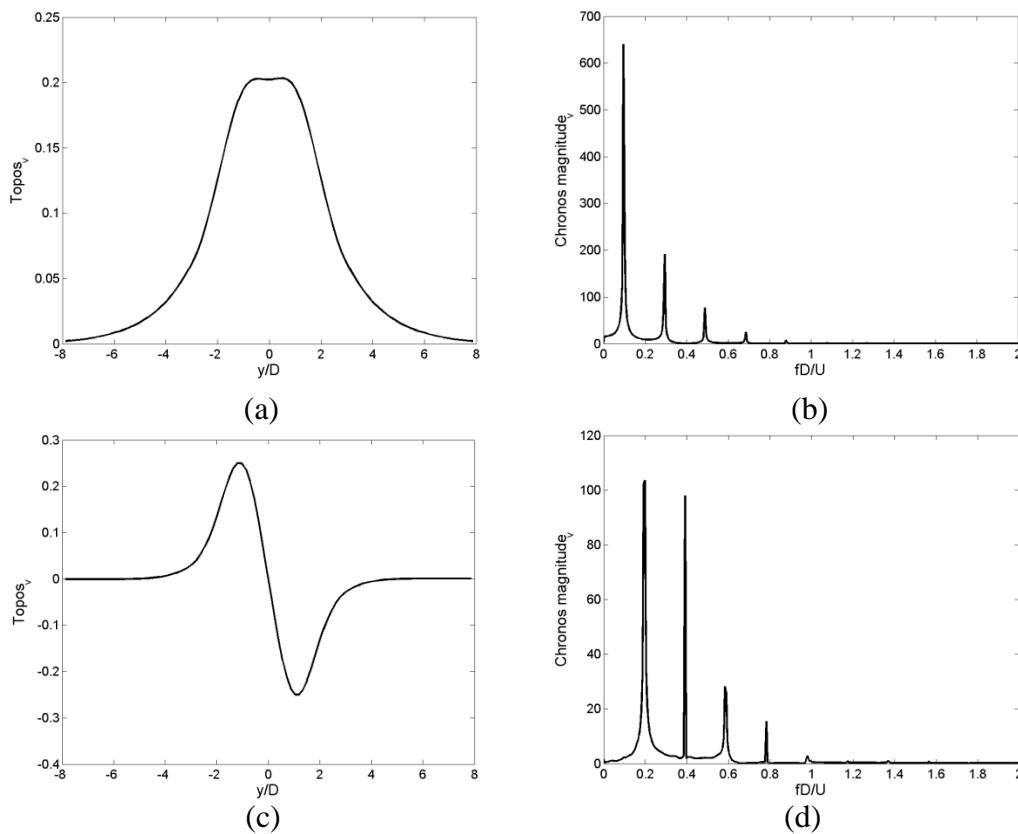


Figure 2-7: The spatial and temporal basic functions of two dominant modes for  $A/D = 0.5$  (a) first *topos* (b) first *chronos* (c) second *topos* (d) second *chronos*.

The eigenmodes in terms of contours computed for the 40 cycle of the  $v$ -velocity are given in Figures 2-8(a)-2-8(h) representing the competition between the symmetric and antisymmetric modes. For  $A/D = 0.5$ , the torus doubling bifurcation is observed.

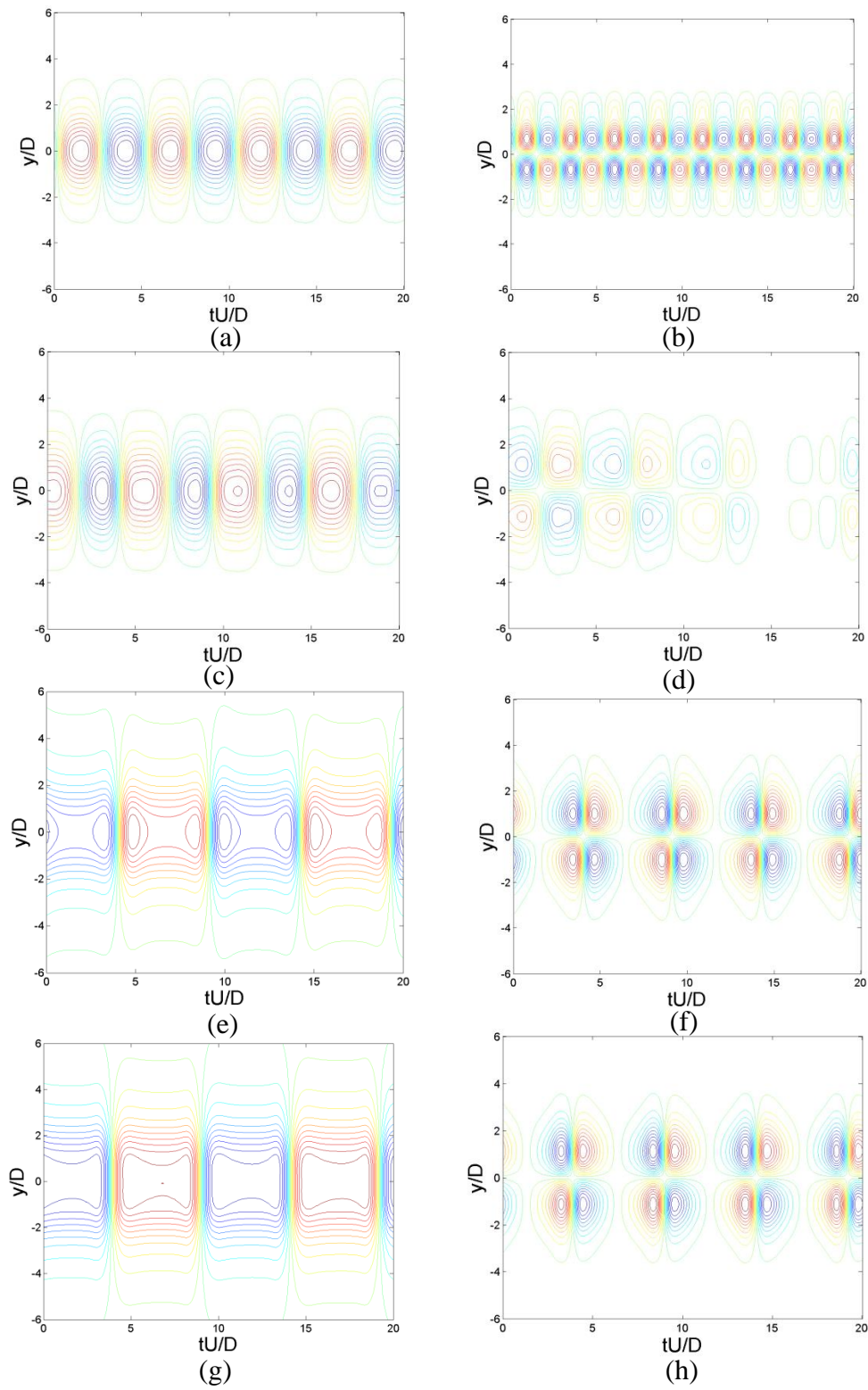


Figure 2-8: Temporal evolution of two primary modes at different oscillation amplitudes (a,b) fixed cylinder case (c,d)  $A/D = 0.15$  (e,f)  $A/D = 0.35$  (g,h)  $A/D = 0.5$ .

Although the antisymmetric pair mode is energized as shown in Figure 2-7(d) due to the inline oscillation, the energy of the first pair mode is again higher than the second one. Hence, the basic  $v$ -velocity pattern is symmetric but with a larger spacing between vortices as shown in Figure 2-8(g) corresponding to the lower Strouhal number,  $St. = 0.1$ .

The dependence of the lift coefficient dynamics on the amplitude oscillation is shown in Figure 2-9. As the amplitude of oscillation increases, the steady periodic lift coefficient becomes quasi-periodic.

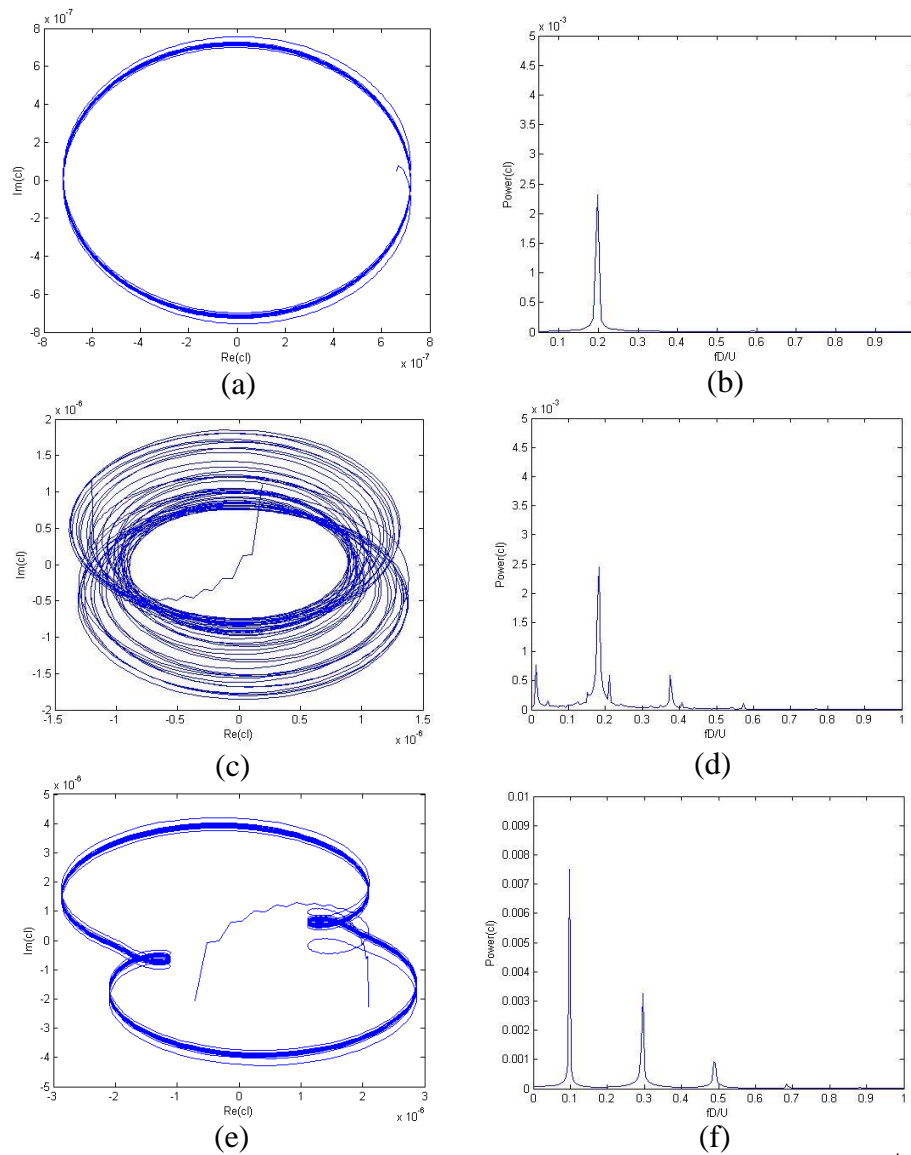


Figure 2-9: Hilbert transform of lift coefficient for (a) fixed cylinder case (b)  $A/D = 0.175$  (c)  $A/D = 0.5$ . Lift coefficient frequency peak for (d) fixed cylinder case (e)  $A/D = 0.175$  (f)  $A/D = 0.5$

The dominant peak of the lift coefficient for  $A/D=0.5$  is precisely equal to the peak of the  $v$ -velocity first mode given in Figure 2-7(b). The presence of the other peaks in Figure 2-9(f) in addition to the dominant one confirms the quasi-periodic dynamics of the lift coefficient. The model comparison plotted in Figures 2-18(e) and 2-18(f) on the Poincare map indicates the same period-2 state.

## 2.7 Derivation of Symmetry Based Model

As shown in the  $v$ -velocity singular values of Figures 2-2 and 2-3, the harmonic streamwise oscillation excites two dominant modes of the  $v$ -velocity while the other modes remain stable. These two modes contribute to a one spatial dimension pattern deduced under the bifurcation parameter variation due to the oscillation amplitude. The general solution describing the 1D oscillatory pattern, that sets in at the bifurcation point with defined temporal and spatial periods can be expressed as

$$v(x, y, t) = S(t)e^{i(\frac{x}{\lambda_s} + \omega_s t)} f(y) + K(t)e^{i(\frac{x}{\lambda_k} + \omega_k t)} g(y) + h.o.t, \quad (2.3)$$

where  $S(t)$  and  $K(t)$  are the time dependent amplitudes and  $f(y)$ ,  $g(y)$  are the corresponding eigenfunctions. Here  $h.o.t$  indicates the higher harmonic terms whose amplitudes can be included in terms of the amplitudes of the primary modes S and K. The wavelength ratio is  $\lambda_s/\lambda_k = \omega_k/\omega_s = m/n = 2$ . Therefore, Eq. (2.3) can be written as

$$v(x, y, t) = S(t)e^{i(kx + \omega t)} f(y) + K(t)e^{2i(kx + \omega t)} g(y) + h.o.t, \quad (2.4)$$

where the complex amplitudes (S, K) satisfy equations that are equivariant with respect to the related action of the symmetry group. Each mode has its own symmetry group. The S mode satisfies the following symmetry properties

$$v(x, y, t) = v(x, -y, t) = v(x + \lambda_s, y, t) = v(x, y, t + \tau_s), \quad (2.5)$$

and K mode has symmetries:

$$v(x, y, t) = v(x, -y, t + \tau_k/2) = v(x + \lambda_k/2, -y, t) \quad (2.6)$$

where  $\tau_s = \frac{2\pi}{\omega_s}$ ,  $\tau_k = \frac{2\pi}{\omega_k}$ . Thus the overall symmetry group of the system is

$$\begin{aligned}
\kappa : y \rightarrow -y &\Rightarrow \kappa(S, K) = (S, -K) \\
T : x \rightarrow x + l\lambda_s &\Rightarrow T(S, K) = (Se^{inl}, Ke^{iml}) \\
\theta : t \rightarrow t + \theta \lambda_s / 2\pi &\Rightarrow \theta(S, K) = (Se^{in\theta}, Ke^{im\theta})
\end{aligned} \tag{2.7}$$

The symmetry  $\kappa$  acts through reflection represented as  $Z_2(\kappa)$ ,  $T$  acts through translation represented as  $SO(2)$  and  $\theta$  phase shift symmetry, represented by  $S^1$ . Thus, the overall symmetry is  $SO(2) \times Z_2(\kappa) \times S^1 = O(2) \times S^1$ . To derive the amplitude equations, equivariance under the translations in  $x$  and  $t$  and reflections lead to the invariants:

$$|S|^2, |K|^2, (K^n \bar{S}^m)^2 \tag{2.8}$$

and four equivariants as:

$$(S, K^{2n} \bar{S}^{2m-1}), (K, S^{2m} \bar{K}^{2n-1}) \tag{2.9}$$

The derivation of the invariants and equivariants is presented in appendix C. The most general form of the amplitude equations is the following:

$$\begin{aligned}
\frac{dS}{dt} = & [(\xi_0 + i\gamma_0) + (\xi_1 + i\gamma_1)|K|^2 + (\xi_2 + i\gamma_2)|S|^2 + (\xi_3 + i\gamma_3)(K^n \bar{S}^m)^2]S + \\
& [(\eta_0 + i\kappa_0) + (\eta_1 + i\kappa_1)|K|^2 + (\eta_2 + i\kappa_2)|S|^2 + (\eta_3 + i\kappa_3)(K^n \bar{S}^m)^2]K^{2n} \bar{S}^{2m-1}
\end{aligned} \tag{2.10(a)}$$

$$\begin{aligned}
\frac{dK}{dt} = & [(\alpha_0 + i\delta_0) + (\alpha_1 + i\delta_1)|K|^2 + (\alpha_2 + i\delta_2)|S|^2 + (\alpha_3 + i\delta_3)(K^n \bar{S}^m)^2]K + \\
& [(\beta_0 + i\mu_0) + (\beta_1 + i\mu_1)|K|^2 + (\beta_2 + i\mu_2)|S|^2 + (\beta_3 + i\mu_3)(K^n \bar{S}^m)^2]\bar{K}^{2n-1} S^{2m}
\end{aligned} \tag{2.10(b)}$$

Since the coefficients of the amplitude equations are complex, the frequency variation of the transition modes can be analyzed. The solution branch types and their stabilities can be determined as functions of coefficient values.

### 2.7.1 Truncation of the amplitude equation up to third order $O(3)$

The mode interaction equations first truncated up to third order are

$$\frac{dS}{dt} = [(\xi_0 + i\gamma_0) + (\xi_1 + i\gamma_1)|K|^2 + (\xi_2 + i\gamma_2)|S|^2]S \tag{2.11(a)}$$

$$\frac{dK}{dt} = [(\alpha_0 + i\delta_0) + (\alpha_1 + i\delta_1)|K|^2 + (\alpha_2 + i\delta_2)|S|^2]K \tag{2.11(b)}$$

The real part of the first complex coefficient describes the growth rate of each mode due to the linear instabilities of the cylinder wake. The cubic terms of the Landau model describe the saturation of the modes S and K. The coupling terms describe the mode interaction effect. If the sign of the cubic term is positive, the bifurcation is supercritical and if negative, it represents the subcritical one. These equations can be put into amplitude and phase form by writing  $S = qe^{i\psi}$ ,  $K = re^{i\phi}$  where  $q, r > 0$  and  $0 \leq \phi, \psi < 2\pi$ . Separating out the real and imaginary parts of the equations lead to

$$\frac{dq}{dt} = (\xi_0 + \xi_1 r^2 + \xi_2 q^2)q \quad (2.12(a))$$

$$\frac{dr}{dt} = (\alpha_0 + \alpha_1 r^2 + \alpha_2 q^2)r \quad (2.12(b))$$

$$\omega_{sat,s} = \frac{d\psi}{dt} = \gamma_0 + \gamma_1 r^2 + \gamma_2 q^2 \quad (2.12(c))$$

$$\omega_{sat,k} = \frac{d\phi}{dt} = \delta_0 + \delta_1 r^2 + \delta_2 q^2 \quad (2.12(d))$$

The individual imaginary part represents the saturated frequency for each mode. The phase equations  $d\phi/dt$  and  $d\psi/dt$  do not appear in the amplitude equations and depend only on  $q$  and  $r$ , so if  $q$  and  $r$  are stable to perturbation, they will be too. This means that for stability analysis just the amplitude equations are considered. But to see the frequency effects on the amplitude equation, the amplitude equation is expanded up to higher order and the stability analysis is considered for this case.

### 2.7.2 Truncating the amplitude equation up to order $O(7)$

The phases of modes only affect the dynamics through the terms involving  $m$  and  $n$  and by truncations up to low orders, their effect is ignored. The frequencies of these modes will vary along the transition between the solution branches, as they undergo the bifurcation. As mentioned, the amplitude equations at third order are not sufficient to describe the hysteresis. Hence, the amplitude equations are expanded up to 7<sup>th</sup> order.

$$\begin{aligned} \frac{dS}{dt} = & [\xi_0 + i\gamma_0 + (\xi_1 + i\gamma_1)|K|^2 + (\xi_2 + i\gamma_2)|S|^2 + (\xi_3 + i\gamma_3)(K\bar{S}^2)^2]S + \\ & [\eta_0 + i\kappa_0 + (\eta_1 + i\kappa_1)|K|^2 + (\eta_2 + i\kappa_2)|S|^2]K^2\bar{S}^3 \end{aligned} \quad (2.13(a))$$

$$\begin{aligned} \frac{dK}{dt} = & [\alpha_0 + i\delta_0 + (\alpha_1 + i\delta_1)|K|^2 + (\alpha_2 + i\delta_2)|S|^2 + (\alpha_3 + i\delta_3)(K\bar{S}^2)^2]K + \\ & [\beta_0 + i\mu_0 + (\beta_1 + i\mu_1)|K|^2 + (\beta_2 + i\mu_2)|S|^2]\bar{K}S^4 \end{aligned} \quad (2.13(b))$$

The complex equations can be rewritten in polar form by setting  $S = qe^{i\psi}$ ,  $K = re^{i\varphi}$  and separating out the real and imaginary parts of the equations to get

$$\begin{aligned} \frac{dq}{dt} = & [\xi_0 + \xi_1 r^2 + \xi_2 q^2 + (\xi_3 \cos 2\theta - \gamma_3 \sin 2\theta)r^2 q^4]q + \\ & [(\eta_0 + \eta_1 r^2 + \eta_2 q^2) \cos 2\theta - (\kappa_0 + \kappa_1 r^2 + \kappa_2 q^2) \sin 2\theta]r^2 q^3 \end{aligned} \quad (2.14(a))$$

$$\begin{aligned} \frac{dr}{dt} = & [\alpha_0 + \alpha_1 r^2 + \alpha_2 q^2 + (\alpha_3 \cos 2\theta - \delta_3 \sin 2\theta)r^2 q^4]r + \\ & [(\beta_0 + \beta_1 r^2 + \beta_2 q^2) \cos 2\theta + (\mu_0 + \mu_1 r^2 + \mu_2 q^2) \sin 2\theta]r q^4 \end{aligned} \quad (2.14(b))$$

$$\begin{aligned} \frac{d\psi}{dt} = & \gamma_0 + \gamma_1 r^2 + \gamma_2 q^2 + [\gamma_3 \cos 2\theta + \xi_3 \sin 2\theta]r^2 q^4 + \\ & [(\eta_0 + \eta_1 r^2 + \eta_2 q^2) \sin 2\theta + (\kappa_0 + \kappa_1 r^2 + \kappa_2 q^2) \cos 2\theta]q^2 r^2 \end{aligned} \quad (2.14(c))$$

$$\begin{aligned} \frac{d\varphi}{dt} = & \delta_0 + \delta_1 r^2 + \delta_2 q^2 + [\delta_3 \cos 2\theta + \alpha_3 \sin 2\theta]r^2 q^4 + \\ & [(\mu_0 + \mu_1 r^2 + \mu_2 q^2) \cos 2\theta - (\beta_0 + \beta_1 r^2 + \beta_2 q^2) \sin 2\theta]q^4 \end{aligned} \quad (2.14(d))$$

Combining (2.14(c)) and (2.14(d)) gives

$$\begin{aligned} \frac{d\theta}{dt} = & \delta_0 - 2\gamma_0 + (\delta_1 - 2\gamma_1)r^2 + (\delta_2 - 2\gamma_2)q^2 + [(\delta_3 - 2\gamma_3) \cos 2\theta + \\ & (\alpha_3 - 2\xi_3) \sin 2\theta]r^2 q^4 + [(\mu_0 + \mu_1 r^2 + \mu_2 q^2) \cos 2\theta - (\beta_0 + \beta_1 r^2 + \beta_2 q^2) \sin 2\theta]q^4 - \\ & 2[(\eta_0 + \eta_1 r^2 + \eta_2 q^2) \sin 2\theta + (\kappa_0 + \kappa_1 r^2 + \kappa_2 q^2) \cos 2\theta]q^2 r^2 \end{aligned} \quad (2.14(e))$$

where  $\theta = \varphi - 2\psi$  is the phase difference and therefore the system is in fact three dimensional. As shown in Eq. (2.14(e)) the evolution of the individual phases are functions of  $r, q$  and  $\theta$ . Therefore, the fixed points of Eq. (2.14(e)) with  $\varphi, \psi \neq 0$  corresponds to periodic solution of Eq. (2.13(a)) and (2.13(b)) while the limit cycles of Eq. (2.14(e)) relate to the tori in the set of Eq. (2.13).

### 2.7.3 Solution branches

As the symmetry group  $O(2) \times S^1$  is continuous, there exist an infinite number of solutions when the symmetry is broken. Using the equivariant bifurcation theory the maximal subgroups with lower order symmetries and fixed-point dimensions are identified. The steady solution branches of the amplitude equations of  $O(3)$  by  $dq/dt = dr/dt = 0$  leads to three types: (i) Trivial solution, where  $q = r = 0$ , (ii) Pure modes. These solutions are

$$q = 0, r^2 = \frac{-\alpha_0}{\alpha_1}, \frac{d\varphi}{dt} = \delta_0 - \frac{\delta_1 \alpha_0}{\alpha_1} \quad (2.15(a))$$

$$r = 0, q^2 = \frac{-\xi_0}{\xi_2}, \frac{d\psi}{dt} = \gamma_0 - \frac{\gamma_2 \xi_0}{\xi_2} \quad (2.15(b))$$

The general form of Eq. (2.15(b)) is  $v(x, y, t) = \sqrt{-\xi_0/\xi_2} e^{i(kx + \omega t + \varphi_0)} f(y)$  which has isotropy group  $\widetilde{SO}(2) \times Z_2(\kappa)$ . The definition of  $\widetilde{SO}(2) = \{(\theta, -\theta) : 0 \leq \theta \leq 2\pi\}$  is that a translation through  $\theta$  has the same effect as a phase shift  $-\theta$ . Also, the pure mode K solution is  $v(x, y, t) = \sqrt{-\alpha_0/\alpha_1} e^{2i(kx + \omega t + \psi_0)} g(y)$  with isotropy group  $\widetilde{SO}(2) \times Z_2(\kappa, \pi)$ . The pure modes are travelling waves and have one dimensional fixed point subspace. They maintain the spatio-temporal symmetry at all times, while oscillating periodically. (iii) Mixed modes. These solutions can be calculated by solving the coupled set of equations (2.12). The fixed point amplitude values are

$$q^2 = \frac{\alpha_0 \xi_1 - \alpha_1 \xi_0}{\alpha_1 \xi_2 - \alpha_2 \xi_1} \quad (2.16(a))$$

$$r^2 = -\frac{1}{\xi_1} \left[ \xi_0 + \xi_2 \left( \frac{\alpha_0 \xi_1 - \alpha_1 \xi_0}{\alpha_1 \xi_2 - \alpha_2 \xi_1} \right) \right] \quad (2.16(b))$$

The phase speeds of the mixed travelling waves can be calculated by substituting the values of  $r$  and  $q$  in Eq. (2.12(c)) and (2.12(d)). The corresponding flow field will be:

$$v(x, y, t) = q_{TW} e^{i(k_s x + \omega_s t + \psi_0)} f(y) + r_{TW} e^{i(k_s x + \omega_s t + \varphi_0)} g(y) \quad (2.17)$$

The mixed solution has maximum  $\widetilde{SO}(2)$  symmetry subgroup. Since the relative phase equation does not exist, it is not possible to distinguish the steady periodic solutions from the mixed



modulated waves (torus). As mentioned earlier, in order to determine the types of mixed modes, the amplitude equations should be expanded up to higher orders. For the O (7) truncated amplitude equations, the steady state solution branches are again found by setting  $dq/dt = dr/dt = d\theta/dt = 0$ . In addition to the trivial solution, two types of solution branches are possible. The basic steady solution branches can be listed as:

- 1- Pure mode which is similar to the low order model O(3). This solution is given by  $(S, K) = \left( \sqrt{-\xi_0/\xi_2} e^{i\psi} f(y), 0 \right)$  that is calculated by solving the set of Eq. (2.12) determining the amplitude and phase of the pure mode.
- 2- Mixed modes. There are two types of mixed modes.
  - Travelling waves (TW). These are solutions of the form  $(qe^{i\psi}, re^{2i\psi})$ . The solutions are deduced from solving the set of Eq. (2.14) to get the fixed points. Since  $d\varphi/dt = 2d\psi/dt \neq 0$ , but  $d\theta/dt = 0$ , the travelling waves are the periodic orbits within the Eq. (2.13(a)) and (2.13(b)).
  - Modulated travelling waves (MTW). MTW correspond to tori when  $d\theta/dt \neq 0$ .

## 2.7.4 Coefficients calculation using dominant POD modes of the transverse velocity

The amplitude equation coefficients are calculated using the *chronos* of two primary modes obtained from the POD analysis. The equations have been developed in the case of complex amplitudes, so the data are transformed into complex signals by Hilbert transformation. The Landau coefficients which cover the initial transition until the steady periodic region are calculated for each mode independently at each of the oscillation amplitude. Since the data is recorded for 40 cycles, the system of Eq. (2.18) is over-determined and the constants can be calculated using least squares method.

$$\begin{bmatrix} S_1 & |S_1|^2 S_1 \\ \vdots & \vdots \\ S_i & |S_i|^2 S_i \\ \vdots & \vdots \\ S_{39} & |S_{39}|^2 S_{39} \end{bmatrix} \begin{bmatrix} \xi_0 + i\gamma_0 \\ \xi_2 + i\gamma_2 \end{bmatrix} = \begin{bmatrix} S_2 - S_1 \\ \vdots \\ S_{i+1} - S_i \\ \vdots \\ S_{40} - S_{39} \end{bmatrix} \quad (2.18(a))$$

$$\begin{bmatrix} K_1 & |K_1|^2 K_1 \\ \vdots & \vdots \\ K_i & |K_i|^2 K_i \\ \vdots & \vdots \\ K_{39} & |K_{39}|^2 K_{39} \end{bmatrix} \begin{bmatrix} \alpha_0 + i\delta_0 \\ \alpha_1 + i\delta_1 \end{bmatrix} = \begin{bmatrix} K_2 - K_1 \\ \vdots \\ K_{i+1} - K_i \\ \vdots \\ K_{40} - K_{39} \end{bmatrix} \quad (2.18(b))$$

The coupling coefficients are also determined by least squares method. These coefficients are calculated at the oscillation amplitudes where mode K is initially observed and the last time that mode S occurs. Then, the known landau coefficients of mode S for A/D=0.5 are substituted in the Eq. (2.13(a)) and the coupling coefficients are obtained from the over-determined system given by Eq. (2.19(a)). Applying the same method for the fixed cylinder case, the coupling coefficients of K mode are achieved. Thus the critical amplitude for mode K is the fixed cylinder case, A/D=0.0 where mode K is weak and for mode S, A/D=0.5 where its energy is reduced. The deduced coefficients are presented in Table 2-1.

$$\begin{bmatrix} |K_1|^2 S_1 & (K_1 \bar{S}_1)^2 S_1 & K_1^2 \bar{S}_1^3 & |K_1|^2 K_1^2 \bar{S}_1^3 & |S_1|^2 K_1^2 \bar{S}_1^3 \\ \vdots & \vdots & \vdots & \vdots & \vdots \\ |K_i|^2 S_i & (K_i \bar{S}_i)^2 S_i & K_i^2 \bar{S}_i^3 & |K_i|^2 K_i^2 \bar{S}_i^3 & |S_i|^2 K_i^2 \bar{S}_i^3 \\ \vdots & \vdots & \vdots & \vdots & \vdots \\ |K_{39}|^2 S_{39} & (K_{39} \bar{S}_{39})^2 S_{39} & K_{39}^2 \bar{S}_{39}^3 & |K_{39}|^2 K_{39}^2 \bar{S}_{39}^3 & |S_{39}|^2 K_{39}^2 \bar{S}_{39}^3 \end{bmatrix} \begin{bmatrix} \xi_1 + i\gamma_1 \\ \xi_3 + i\gamma_3 \\ \eta_0 + i\kappa_0 \\ \eta_1 + i\kappa_1 \\ \eta_2 + i\kappa_2 \end{bmatrix} = \begin{bmatrix} S_2 - S_1 - [(\xi_0 + i\gamma_0)S_1 + (\xi_2 + i\gamma_2)|S_1|^2 S_1]_{A/D=0.5} \\ \vdots \\ S_{i+1} - S_i - [(\xi_0 + i\gamma_0)S_i + (\xi_2 + i\gamma_2)|S_i|^2 S_i]_{A/D=0.5} \\ \vdots \\ S_{40} - S_{39} - [(\xi_0 + i\gamma_0)S_{39} + (\xi_2 + i\gamma_2)|S_{39}|^2 S_{39}]_{A/D=0.5} \end{bmatrix} \quad (2.19(a))$$

$$\begin{bmatrix} |S_1|^2 K_1 & (K_1 \bar{S}_1^2)^2 K_1 & \bar{K}_1 S_1^4 & |K_1|^2 \bar{K}_1 S_1^4 & |S_1|^2 \bar{K}_1 S_1^4 \\ \vdots & \vdots & \vdots & \vdots & \vdots \\ |S_i|^2 K_i & (K_i \bar{S}_i^2)^2 K_i & \bar{K}_i S_i^4 & |K_i|^2 \bar{K}_i S_i^4 & |S_i|^2 \bar{K}_i S_i^4 \\ \vdots & \vdots & \vdots & \vdots & \vdots \\ |S_{39}|^2 K_{39} & (K_{39} \bar{S}_{39}^2)^2 K_{39} & \bar{K}_{39} S_{39}^4 & |K_{39}|^2 \bar{K}_{39} S_{39}^4 & |S_{39}|^2 \bar{K}_{39} S_{39}^4 \end{bmatrix} \begin{bmatrix} \alpha_2 + i\delta_2 \\ \alpha_3 + i\delta_3 \\ \beta_0 + i\mu_0 \\ \beta_1 + i\mu_1 \\ \beta_2 + i\mu_2 \end{bmatrix} = \begin{bmatrix} K_2 - K_1 - [(\alpha_0 + i\delta_0)K_1 + (\alpha_1 + i\delta_1)|K_1|^2 K_1]_{A/D=0.0} \\ \vdots \\ S_{i+1} - S_i - [(\alpha_0 + i\delta_0)K_i + (\alpha_1 + i\delta_1)|K_i|^2 K_i]_{A/D=0.0} \\ \vdots \\ S_{40} - S_{39} - [(\alpha_0 + i\delta_0)K_{39} + (\alpha_1 + i\delta_1)|K_{39}|^2 K_{39}]_{A/D=0.0} \end{bmatrix} \quad (2.19(b))$$

Table 2-1: The coefficients of the amplitude equation deduced from the least squares method.

	$\xi_0 + i\gamma_0$	$\xi_1 + i\gamma_1$	$\xi_2 + i\gamma_2$	$\xi_3 + i\gamma_3$	$\eta_0 + i\kappa_0$	$\eta_1 + i\kappa_1$	$\eta_2 + i\kappa_2$
S	0.0926-0.08i	0.0-85.57i	-2.04+1.39i	985.32-3281.8i	-720.41+197.49i	95977+37561i	985.32-3281.8i
K	$\alpha_0 + i\delta_0$	$\alpha_1 + i\delta_1$	$\alpha_2 + i\delta_2$	$\alpha_3 + i\delta_3$	$\beta_0 + i\mu_0$	$\beta_1 + i\mu_1$	$\beta_2 + i\mu_2$
	0.25+0.25i	-80.63-37.59i	-4.15-5.98i	-198880+20991i	-57.45+2.96i	64593+115600i	819.87-427.48i

The real parts of both modes approximated from the amplitude equations are plotted in Figure 2-10. Both the frequency and amplitude of the modes match well with the simulation results. Now by variation of the bifurcation parameter due to the amplitude oscillation, the solution branches can be determined.

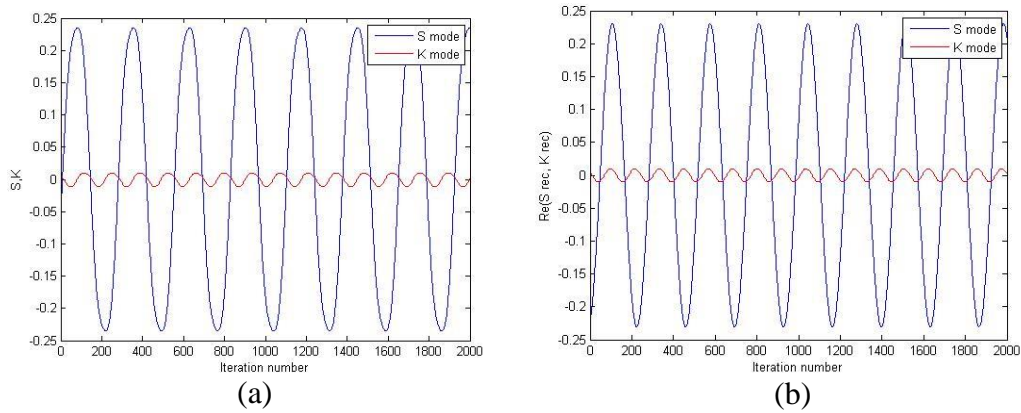


Figure 2-10: (a) The *chronos* of modes S and K from CFD, (b) Deduced S and K modes approximated from the least squares method of the dominant *chronos* data.

## 2.8 Bifurcation and stability analysis

Through the coefficients found from the *chronos* of the first two primary modes, the linear terms of the amplitude equations are influenced by harmonic inline oscillation. The nature of the interaction between different solution branches as linear bifurcation parameters are varied can be determined while the other coefficients remain fixed. Thus the bifurcation analysis is considered for the linear terms variation, obtained from the numerical computations. As the amplitude of oscillation increases,  $\xi_0$  decreases,  $\delta_0$  increases while  $\gamma_0, \alpha_0$  do not change. Therefore, the mixed modes undergo bifurcation by smooth variation of these two parameters  $\xi_0$  and  $\delta_0$ . The two steady travelling waves of Figure 2-10(b) lose stability via a Hopf bifurcation at  $\xi_0 = 0.0836$  and  $\delta_0 = 0.29$  shown in Figure 2-11. As the torus doubling bifurcation is approached at  $\xi_0 = 0.0826$  and  $\delta_0 = 0.46$ , two period-doubled tori are deduced as shown in Figure 2-12. Due to the principle solution branch classification, the bifurcated responses of the mode interaction are mixed modulated travelling waves (MTW) with  $\widetilde{SO}(2)$  symmetry group. As shown in Figure 2-12 the bifurcated mode S has higher energy with respect to the larger amplitude value in comparison with the bifurcated mode K which leads to the reflection symmetry  $Z_2(\kappa)$  becoming dominant in the flow field. The quasi-periodic solution of the complex amplitude in terms of mode S and K are shown in Figures 2-13 and 2-14.

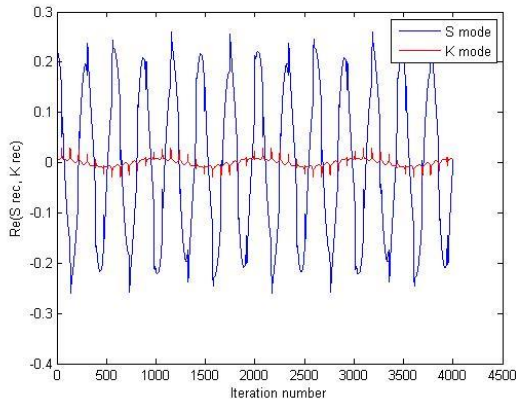


Figure 2-11: Quasi-periodic state of modes S and K at  $\xi_0 = 0.0836$ ,  $\delta_0 = 0.29$ .

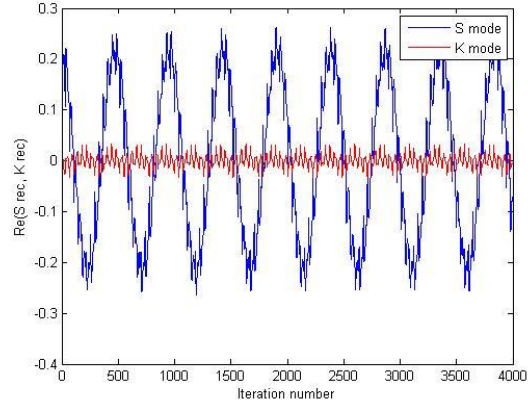


Figure 2-12: Quasi-periodic state of modes S and K at  $\xi_0 = 0.0826$ ,  $\delta_0 = 0.46$ .

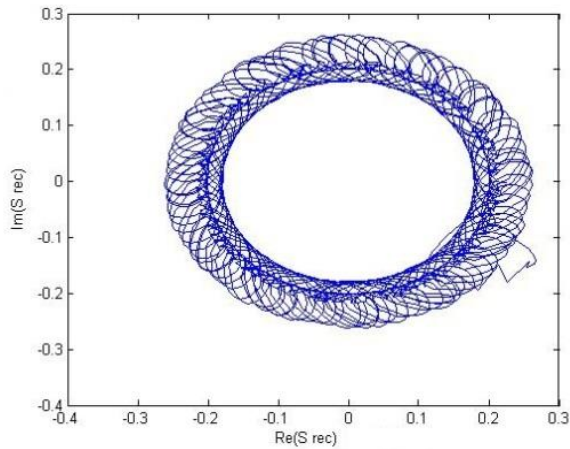


Figure 2-13: Complex amplitude of bifurcated mode S at  $\xi_0 = 0.0826$ ,  $\delta_0 = 0.46$ .

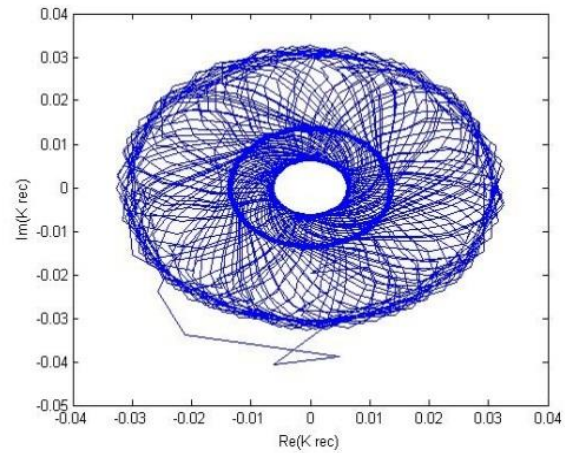


Figure 2-14: Complex amplitude of bifurcated mode K at  $\xi_0 = 0.0826$ ,  $\delta_0 = 0.46$ .

As previously mentioned, the physical significance of the inline amplitude oscillation can be modeled by variation of the two parameters  $\xi_0$  and  $\delta_0$ . Thus, the bifurcation analysis in the mixed region is limited to these two coefficients. The stable limit cycle of the amplitudes of S and K modes are given in the following plots.

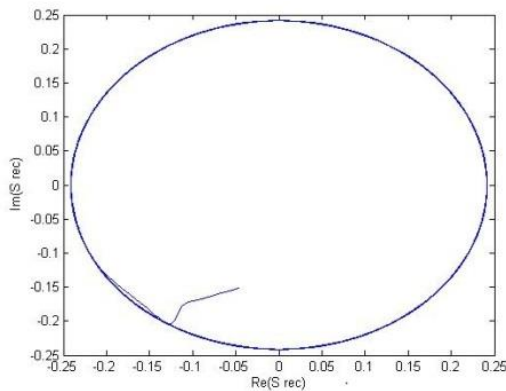


Figure 2-15: Limit cycle of amplitude term of mode S.

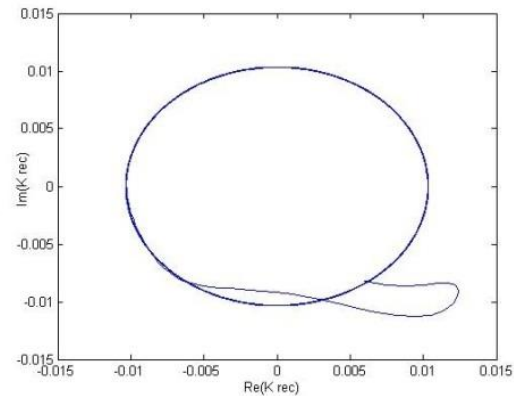


Figure 2-16: Limit cycle of amplitude term of mode K.

The stability of the orbit is analyzed by calculating the Poincare map. The Jacobian of the Poincare map is called monodromy matrix. For the stability analysis, the amplitude equations are rewritten in the Cartesian form using  $S = x + iy$  and  $K = z + ih$ .

$$\begin{aligned} \frac{dx}{dt} = & (\xi_0 + \xi_1(z^2 + h^2) + \xi_2(x^2 + y^2) + \xi_3 A - \gamma_3 B)x - (\gamma_0 + \gamma_1(z^2 + h^2) + \\ & \gamma_2(x^2 + y^2) + \xi_3 B + \gamma_3 A)y + (\eta_0 + \eta_1(z^2 + h^2) + \eta_2(x^2 + y^2))C - \\ & (\kappa_0 + \kappa_1(z^2 + h^2) + \kappa_2(x^2 + y^2))D \end{aligned} \quad (2.20(a))$$

$$\begin{aligned} \frac{dy}{dt} = & (\xi_0 + \xi_1(z^2 + h^2) + \xi_2(x^2 + y^2) + \xi_3 A - \gamma_3 B)y + (\gamma_0 + \gamma_1(z^2 + h^2) + \\ & \gamma_2(x^2 + y^2) + \xi_3 B + \gamma_3 A)x + (\eta_0 + \eta_1(z^2 + h^2) + \eta_2(x^2 + y^2))D + \\ & (\kappa_0 + \kappa_1(z^2 + h^2) + \kappa_2(x^2 + y^2))C \end{aligned} \quad (2.20(b))$$

$$\begin{aligned} \frac{dz}{dt} = & (\alpha_0 + \alpha_1(z^2 + h^2) + \alpha_2(x^2 + y^2) + \alpha_3 A - \delta_3 B)z - (\delta_0 + \delta_1(z^2 + h^2) + \\ & \delta_2(x^2 + y^2) + \alpha_3 B + \delta_3 A)h + (\beta_0 + \beta_1(z^2 + h^2) + \beta_2(x^2 + y^2))E - \\ & (\mu_0 + \mu_1(z^2 + h^2) + \mu_2(x^2 + y^2))F \end{aligned} \quad (2.20(c))$$

$$\begin{aligned} \frac{dh}{dt} = & (\alpha_0 + \alpha_1(z^2 + h^2) + \alpha_2(x^2 + y^2) + \alpha_3 A - \delta_3 B)h + (\delta_0 + \delta_1(z^2 + h^2) + \\ & \delta_2(x^2 + y^2) + \alpha_3 B + \delta_3 A)z + (\beta_0 + \beta_1(z^2 + h^2) + \beta_2(x^2 + y^2))F + \\ & (\mu_0 + \mu_1(z^2 + h^2) + \mu_2(x^2 + y^2))E, \end{aligned} \quad (2.20(d))$$

$$\begin{aligned} A &= (z^2 - h^2)(x^4 + y^4 - 6x^2 y^2) - 8xyz h(y^2 - x^2) \\ B &= 2zh(x^4 + y^4 - 6x^2 y^2) + 4xy(z^2 - h^2)(y^2 - x^2) \\ C &= (z^2 - h^2)(x^3 - 3xy^2) - 2zh(y^3 - 3x^2 y) \\ D &= 2zh(x^3 - 3xy^2) + (z^2 - h^2)(y^3 - 3x^2 y) \\ E &= z(x^4 + y^4 - 6x^2 y^2) + 4xyh(x^2 - y^2) \\ F &= -h(x^4 + y^4 - 6x^2 y^2) + 4xyz(x^2 - y^2) \end{aligned}$$

The Jacobian matrix around the periodic orbit is obtained as

$$J = \begin{bmatrix} \frac{\partial}{\partial x} \left( \frac{dx}{dt} \right) & \frac{\partial}{\partial y} \left( \frac{dx}{dt} \right) & \frac{\partial}{\partial z} \left( \frac{dx}{dt} \right) & \frac{\partial}{\partial h} \left( \frac{dx}{dt} \right) \\ \frac{\partial}{\partial x} \left( \frac{dy}{dt} \right) & \frac{\partial}{\partial y} \left( \frac{dy}{dt} \right) & \frac{\partial}{\partial z} \left( \frac{dy}{dt} \right) & \frac{\partial}{\partial h} \left( \frac{dy}{dt} \right) \\ \frac{\partial}{\partial x} \left( \frac{dz}{dt} \right) & \frac{\partial}{\partial y} \left( \frac{dz}{dt} \right) & \frac{\partial}{\partial z} \left( \frac{dz}{dt} \right) & \frac{\partial}{\partial h} \left( \frac{dz}{dt} \right) \\ \frac{\partial}{\partial x} \left( \frac{dh}{dt} \right) & \frac{\partial}{\partial y} \left( \frac{dh}{dt} \right) & \frac{\partial}{\partial z} \left( \frac{dh}{dt} \right) & \frac{\partial}{\partial h} \left( \frac{dh}{dt} \right) \end{bmatrix}_{X=X_{FP}} \quad (2.21)$$

To investigate the existence and stability of the periodic motions, a stability analysis is performed. The nonlinear nature of the equations does not allow solving analytically for the fixed points. Thus, numerical integration of the equations identifies the fixed points. We are interested in finding the values of  $\xi_0 - \delta_0$  space where torus doubling occurs. The stability of the periodic solution branch can be analyzed by calculating the Jacobian matrix with periodic coefficients. The characteristic polynomial of the Jacobian has the form

$$\lambda^4 + c_3\lambda^3 + c_2\lambda^2 + c_1\lambda + c_0 = 0 \quad (2.22)$$

where the coefficients  $c_i$  are functions of the variables. The periodic solution due to Floquet theory will be stable if all roots have norm less than 1 and it will become unstable if an eigenvalue crosses the unit circle. The monodromy matrix is captured by integrating the Jacobian matrix with period  $\tau = 1.0725$  starting from the fixed point values. The eigenvalues of the monodromy matrix are called Floquet multipliers. Figure 2-17 shows the Argand diagram of the two periodic solution branches undergoing bifurcation by variation of  $\xi_0$  and  $\delta_0$ . The diagram shows the movement of the Floquet multipliers while the bifurcations occur. It indicates that the stable mixed travelling wave (MTW) branches lose stability via a torus bifurcation at  $\xi_0 = 0.0836$  and  $\delta_0 = 0.29$ . At these values of the bifurcation parameters the Floquet multipliers move in the complex plane by the values given in Table 2-2. By later variation of the bifurcation parameters at  $\xi_0 = 0.0826$  and  $\delta_0 = 0.46$  the Floquet multipliers collide with negative real axis and cross the unit cycle at -1, triggering a torus doubling bifurcation.

Table 2-2: Floquet multiplier values at different bifurcation parameters.

Bifurcation parameters Floquet multipliers	$\xi_0 = 0.0926$ $\delta_0 = 0.25$	$\xi_0 = 0.0836$ $\delta_0 = 0.29$	$\xi_0 = 0.0836$ $\delta_0 = 0.36$	$\xi_0 = 0.0826$ $\delta_0 = 0.46$
mode S	-0.1643+ 0.2434i	-0.4310 + 0.9109i	-0.5414	-1.0258
mode K	-0.1650 +0.2410i	-0.4605+ 0.8769i	-0.4709	-1.0267

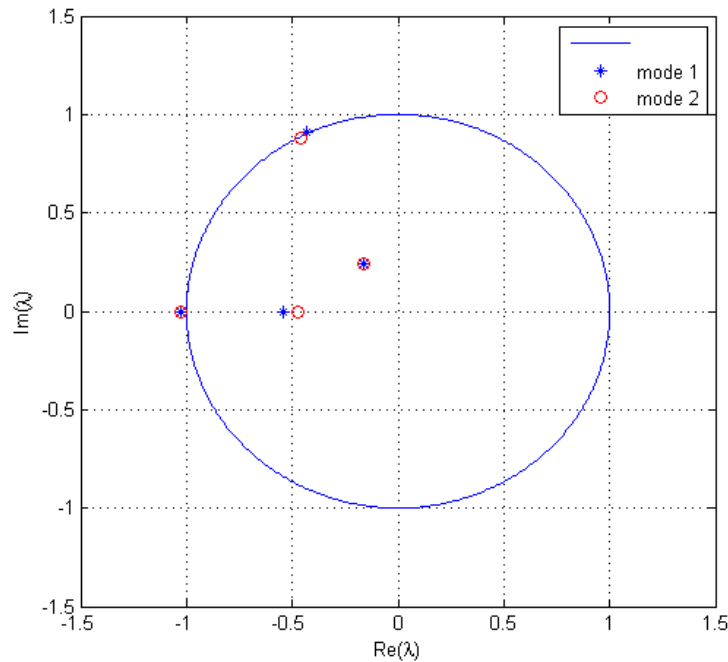


Figure 2-17: Movement of Floquet multipliers of mode K and S by variation of bifurcation parameters.

### 2.8.1 Poincare map

The Poincare maps of the amplitude equation solution branches for different cylinder amplitudes characterize the stability of the two periodic limit cycle responses. For the fixed cylinder case, the periodic response has almost a single Poincare point related to the steady state case (see Figures 2-18(a) and 2-18(b)). As the oscillation amplitude increases at  $\xi_0 = 0.0836$  and  $\delta_0 = 0.29$ , the system undergoes torus bifurcation. The Poincare map of the torus is shown in Figure 2-18(c) and 2-18(d). It is obvious from these figures that by varying the bifurcation parameters small-amplitude fluctuations are observed possibly caused by the interaction of the two frequencies. The later increase in the oscillation amplitude leads to the torus doubling bifurcation at  $\xi_0 = 0.0826$  and  $\delta_0 = 0.46$ . At these values, there is an infinite number of Poincare points organized along two invariant curves associated with the quasi-periodic response of period-doubled torus (Figure 2-18(e) and 2-18(f)).



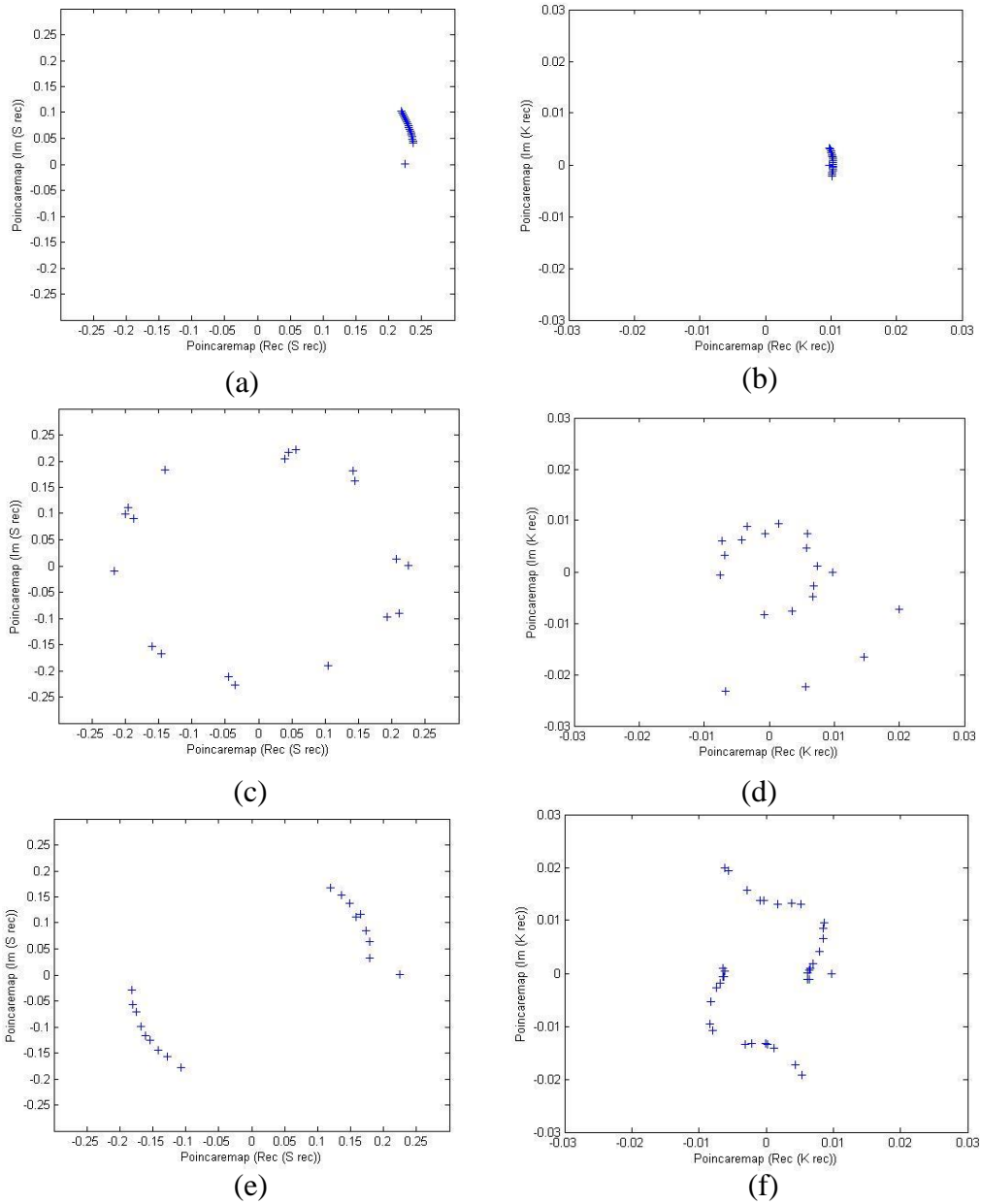


Figure 2-18: Poincare map of the modes S and K at (a,b)  $\xi_0 = 0.0926$ ,  $\delta_0 = 0.25$  (c,d)  $\xi_0 = 0.0836$ ,  $\delta_0 = 0.29$  and (e,f)  $\xi_0 = 0.0826$ ,  $\delta_0 = 0.46$ .

## 2.9 Conclusion

The equivariant bifurcation theory is applied to derive the amplitude equations modeling the cylinder wake mode interaction in Poincaré space. The proposed model predicts the sequence of bifurcations observed in the lift coefficient dynamics obtained from CFD results. This analysis shows that as the amplitude of oscillation increases, the limit cycle undergoes a symmetry-breaking

bifurcation leading to a quasi-periodic state. Further increase in the forcing amplitude leads to a period-doubled torus. The amplitude equations qualitatively explain the nonlinear interaction between symmetric and antisymmetric modes as the oscillation amplitude is increased. The cylinder streamwise oscillation energizes the second mode of the transverse velocity which interacts with the first mode and leading to the torus doubling bifurcation. However, the modulated travelling waves bifurcated from the model have mode S again as the dominant mode which verifies the symmetric  $v$ -velocity pattern with period-doubled bifurcated pattern observed in the numerical results. Thus, the solution branches deduced from the presented model are in good agreement with the wake dynamics obtained from numerical simulations.

## Chapter 3    **ARTICLE 2: LOCK-ON VORTEX SHEDDING PATTERNS AND BIFURCATION ANALYSIS OF THE FORCED STREAMWISE OSCILLATION OF THE CYLINDER WAKE**

Nabatian N. and Mureithi N. W. (2014) submitted to “International Journal of bifurcation and chaos” in April 8, 2014.

### **Abstract**

The 2D numerical simulation of the flow over a cylinder forced to oscillate in the streamwise direction for  $Re=200$  is performed in ANSYS CFX. The controlled-vibration comprised of prescribed inline vibration from  $0.05D$  up to  $0.5D$  with the excitation frequency ratios of 1, 1.5 and 2 including the harmonic and superharmonic excitation regions. The immersed boundary method is used to model the cylinder oscillation. Modal decomposition of the transverse velocity field using the POD method is applied to uncover the interaction of symmetric and antisymmetric modes of the near wake. A model using the first two POD modes is developed by the equivariant bifurcation theory. The present model predicts the mode interactions and bifurcation sequences for all cases which are in good agreement with numerical as well as previous experimental results. Lock-on is determined for a range of values of the oscillation amplitudes and frequency ratios. It is shown that the lock-on range widens with increasing  $A/D$ . The asymmetric 2S, P+S and symmetric pattern S as well as a regime in which vortex formation is not synchronized with cylinder motion are observed in the cylinder wake depending on the combination of oscillation amplitude and frequency ratio. The frequency ratio variation from 1 to 2 leads to the switching from asymmetric to symmetric modes. The symmetric flow pattern corresponds to a near zero lift coefficient on the cylinder.

*Key words:* Modal decomposition; equivariant bifurcation theory; lock-on.

### **3.1 Introduction**

The wake flow behind a cylinder generates transverse and inline fluctuating forces causing the cylinder to vibrate; so called vortex-induced vibration (VIV). The frequency of the vortex shedding

is affected by the cylinder motion and when it is synchronized with the structural frequency VIV phenomenon occurs which causes structural failure. In hydrodynamic flows, the inline force component has been known to excite members of offshore structures, marine piles and submarine periscopes. The controlled vibration is an approach to provide a deeper understanding of VIV behavior. Any motion of a cylinder in a steady approaching flow clearly affects the flow field in the wake of the cylinder depending on the combination of non-dimensional oscillation amplitude  $A/D$  and  $f_e/f_s$  where  $f_e$  is the excitation and  $f_s$  the natural shedding frequency. There have been some experimental investigations involving streamwise forced oscillation of the wake flow (Blackburn and Henderson, 1999; Konstantinidis and Bouris, 2009; Li et al., 2011; Mittal and Kumar, 1999; Papaioannou et al., 2006; Pham et al., 2010; Sohankar, 2007; Srikanth et al., 2011; Xu et al., 2006). Griffin and Ramberg, (1976) were among the first to study the wake flow behind an inline oscillating cylinder in a freestream. They performed simulations of the forced inline oscillation over the range of frequency ratios  $f_e/f_s \in [1.2, 2.5]$  for  $Re=190$ . They showed that during forced oscillation, vortex shedding is affected by the cylinder motion; hence the vortex shedding changes to oscillate with the structural frequency, a phenomenon known as lock-on. Both primary lock-on where  $f_e = f_s$  and subharmonic lock-on with  $f_s = f_e/2$  were observed. Two asymmetric modes of vortex shedding 2S and 2P were observed at the low amplitudes  $0.06 < A < 0.22$ . The asymmetric 2S mode corresponds to the Karman vortex street while in the 2P mode two pairs of vortices are shed per cycle. These flow structures correspond to A-I and A-III modes as categorized by Ongoren and Rockwell, (1988) who investigated the flow patterns for a cylinder forced to oscillate at an angle with respect to the streamwise direction at dimensionless oscillation amplitudes 0.13 and 0.3 and frequency ratios ranging from 0.5 to 4.0. Two basic modes, symmetric and antisymmetric vortex patterns are identified which are classified into five subgroups. The mode S corresponds to the symmetric vortex shedding and A-I, A-II, A-III and A-IV modes for antisymmetric vortex formation. Ongoren and Rockwell experimentally explained the switching between vortex patterns and showed that the modes of vortex shedding can be symmetric, antisymmetric or chaotic depending on the forcing frequency and oscillation amplitude. As mentioned above, the mode of vortex shedding is dependent upon the frequency-amplitude parameters as well as the Reynolds number. The different vortex shedding patterns are classified based on their symmetry properties. The symmetry properties of the vortex patterns can be used in

an analytical study of the vortex shedding by deriving a low order model (Clune and Knobloch, 1993; Goldstein et al., 1992). The Stuart-Landau model was first applied to model the Hopf bifurcation leading to the asymmetric Karman shedding results by Provansal, (1987a). He found that the periodic Karman wake is the saturated product of the temporal global wake instability and suggested that linear stability theory can be applied to find the saturation frequency near the threshold frequency. Later, Barkley et al., (2000) suggested the bifurcation scenario to describe the development and interaction between two three-dimensional modes. The truncated discrete Landau amplitude equations incorporate the coupling terms of mode A and B instabilities and satisfy the spatio-temporal symmetry properties of each mode. In order to model the frequency variation of the transition modes, the coupled Landau equations were then expanded into the complex plane by Sheard et al., (2003). The analytical model to study the forced oscillation considering the symmetry properties was first proposed by Mureithi, (2003; 2010; 2005). He used the symmetry-equivariant theory to study the forced Karman wake. The nonlinear interaction of the Karman and symmetric mode is modeled by symmetry equivariant bifurcation theory in the form of a pair of low order discrete amplitude equations. The coefficients of the amplitude equations are determined by proper orthogonal decomposition (POD) analysis (Chatterjee, 2000; Chen et al., 2012; Graham et al., 1999; Rowley, 2005) of the CFD results. The forced mode is assumed as known and its effect on the vortex shedding mode was investigated.

In the present study, the wake structure and lock-on phenomena are numerically investigated in the near wake region for  $Re=200$  with oscillation amplitude extended up to  $0.5D$  and three frequency ratios  $f_e/f_s = 1, 1.5$  and  $2$ . The two primary modes which exist at various oscillation amplitudes and represent the wake dynamics are determined via POD analysis of the transverse velocity component of the numerical results. The symmetry properties of the model are then applied to develop the analytical model. The coefficients of the amplitude equations are considered complex to include the frequency saturation and solved for higher orders to cover the spatio-temporal effects. These coefficients are calculated by the least squares method from the CFD results. The linear terms of the amplitude equations are assumed to be affected by the variation of the inline cylinder motion and thus considered as the bifurcation parameters. The objective of this work is to numerically investigate the wake flow with velocity streamlines, vorticity contours and lift coefficient transitions at each combination of oscillation amplitudes and forcing frequency ratios and determine the lock-on region. The proposed model is also used to predict the sequence of

bifurcations, and results are compared with those obtained from numerical computations.

### 3.2 Numerical computations

Two-dimensional numerical computations are conducted to simulate the inline forced oscillation with amplitude ratios in the range  $A/D = 0-0.5$  and excitation frequency ratios  $f_e/f_s = 1, 1.5$  and 2 for  $Re=200$ . Simulations are performed for frequencies within the harmonic and superharmonic regions and different oscillation amplitudes to determine the vortex shedding modes and lock-on ranges. The cylinder motion is simulated in the cylinder-fixed frame with a prescribed sinusoidal oscillation imposed in the inflow. The oscillating inlet flow is given by  $u = U + A\omega\sin(\omega t)$  with  $U$  the mean flow velocity,  $\omega$  the perturbation frequency and  $A$  the non-dimensional oscillation amplitude. For the lateral boundaries a symmetry condition is assumed, the no-slip condition is set on the cylinder surface and the outer boundary condition is pressure outlet. The accuracy of the results has already been validated for the stationary cylinder case. The detailed description of the numerical model is presented by Mureithi, (2005).

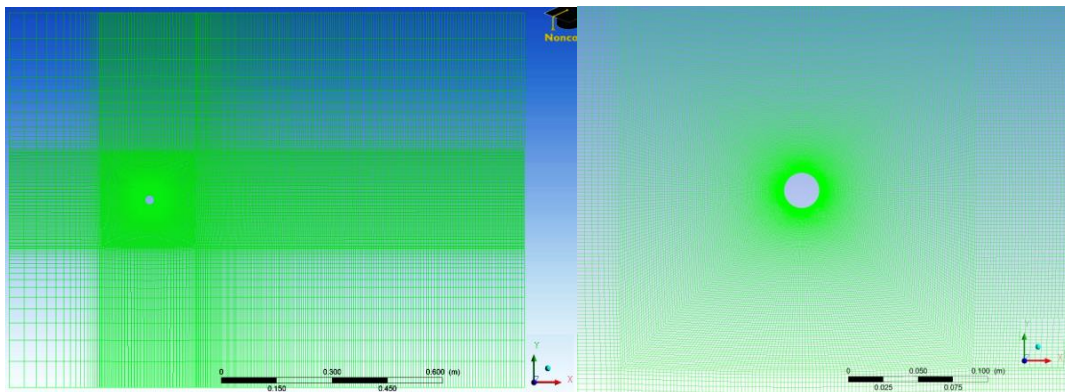


Figure 3-1: The structured mesh of the 2D domain.

The transverse velocity of the forced wake flow is monitored 10D aft of the cylinder at 100 nodes in the  $y$  direction and stored in a matrix,  $A$ . The  $v$ -velocity data is transformed to a complex signal by Hilbert transformation to include the frequency variation. The mean value is then subtracted to reach the velocity fluctuations as

$$v'(y,t) = v(y,t) - v_m(y,t) \quad (3.1)$$

The fluctuating velocity matrix  $A$  can then be decomposed using singular value decomposition (SVD) into spatial and temporal eigenfunctions as

$$v'(y,t) = \sum_{k=1}^{100} a_k(t) \psi_k(y), \quad (3.2)$$

where  $\psi_k(y)$  the spatial eigenvector representing the velocity profile in the  $y$ -direction is called *topos* and  $a_k(t)$  the temporal modal component describing the time history of velocity called *chronos*. Since the *topos* is normalized, the *chronos* contains the energy of each mode. The *topos* and *chronos* are affected by the cylinder motion. These modes are used to develop the amplitude equation modeling the mode interactions of the wake flow.

### 3.3 Numerical Results

In this section, CFD results of the lock-on range and vortex shedding modes for both harmonic and superharmonic excitations at three selected amplitude ratios are presented and compared with the proposed model results.

#### 3.3.1 Harmonic excitation

The case for  $Re=200$  and  $f_e/f_s = 1$  at different oscillation amplitude is considered first. The phase plane and power spectrum of the lift coefficient with the first mode *chronos* of the transverse velocity are plotted in Figure 3-2 to identify the lock-on region. For the stationary cylinder, the limit cycle is observed in the phase plane indicating the lock-on state. The spectrum of the first mode *chronos* confirms the pure sinusoidal response with the presence of a single peak at  $fD/U = 0.2$ . As the oscillation amplitude increases, the phase plane shows that the wake is in a quasi-periodic state with the fluctuation of the lift coefficient on different paths between two successive cycles. The power spectrum of the lift coefficient shows the higher frequency at vortex shedding reduced frequency  $St = 0.2$  while a smaller peak corresponding to the beating behavior at  $fD/U = 0.013$ . Since the secondary frequency is lower than the primary one, it affects the periodicity from cycle-to-cycle and thus the flow is periodic over the beating period. Increasing the oscillation amplitude up to  $A/D=0.5$ , synchronized vortex shedding is again observed. The power spectrum of the lift coefficient and first mode *chronos* given in Figure 3-2(h) and 3-2(i) exhibit the dominant frequency at  $fD/U = 0.1$  although there is a weak secondary peak at  $fD/U = 0.3$ . Since

the frequency of the secondary peak is higher than the lock-on frequency, it does not affect the periodicity of the flow and the lift coefficient trace is repetitive every two cycle of cylinder oscillation.

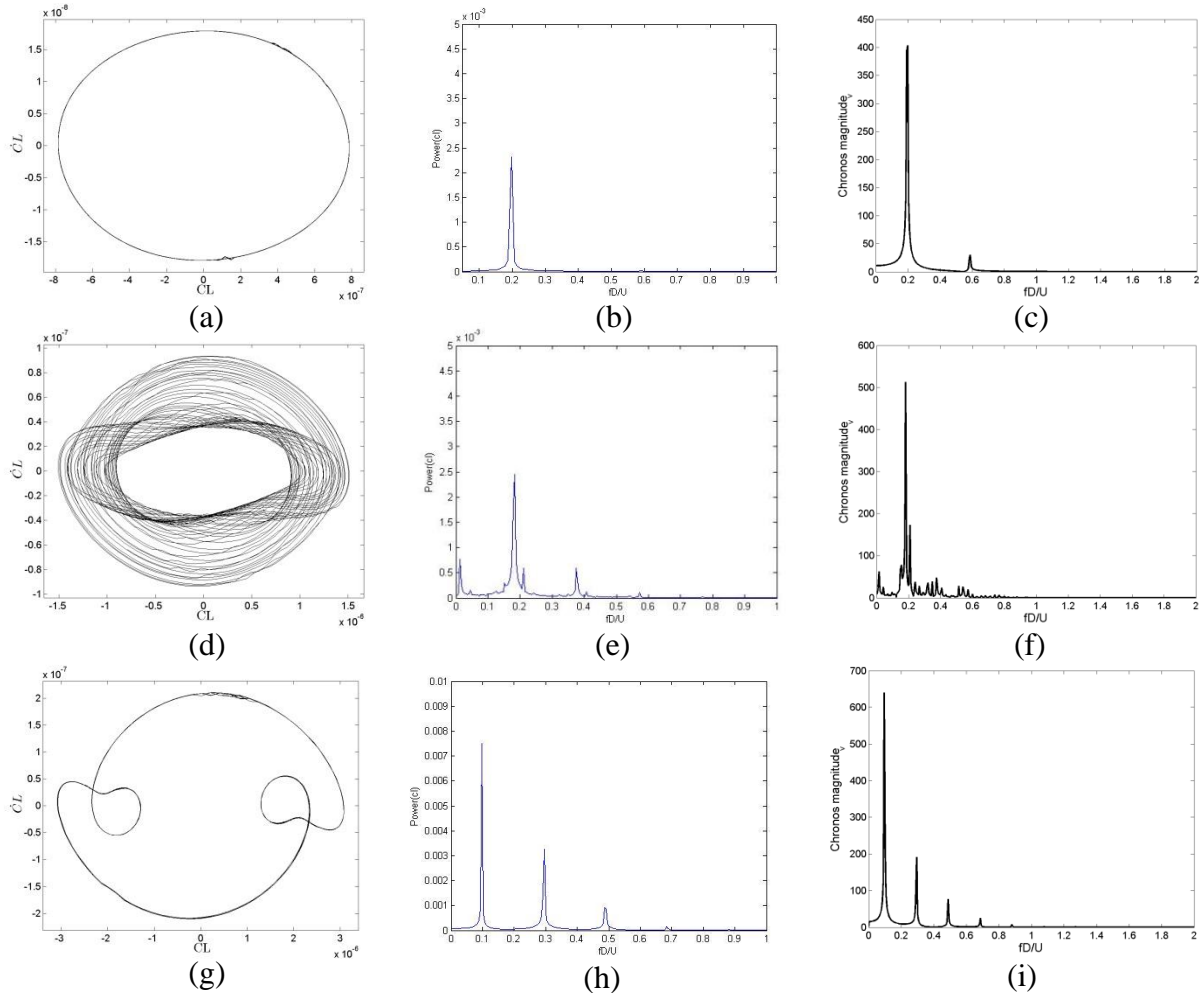


Figure 3-2: Phase plane of the lift coefficient, lift coefficient power spectrum and the  $v$ -velocity first mode *chronos* for three oscillation amplitudes (a-c)  $A/D = 0.0$ , (d-f)  $A/D = 0.175$  and (g-i)

$$A/D = 0.5 \text{ for } f_e/f_s = 1.$$

The periodicity of the fixed cylinder case can also be shown by velocity contours in the wake which are exactly the same at two instants separated by one period  $T_s = 1/f_s$ . For  $A/D = 0.175$  the wake is not locked on the cylinder motion due to the beating behavior. The velocity contours are plotted in Figure 3-3 over 15 cycles of the cylinder oscillation corresponding to the beating period,  $T_b = 15T_e$ . It is clear that the velocity contours at two instants separated by  $T_b$  are exactly the same.



Thus, outside of the lock-on region the vortex shedding periodicity is not periodic over shedding cycle but over the beating period.

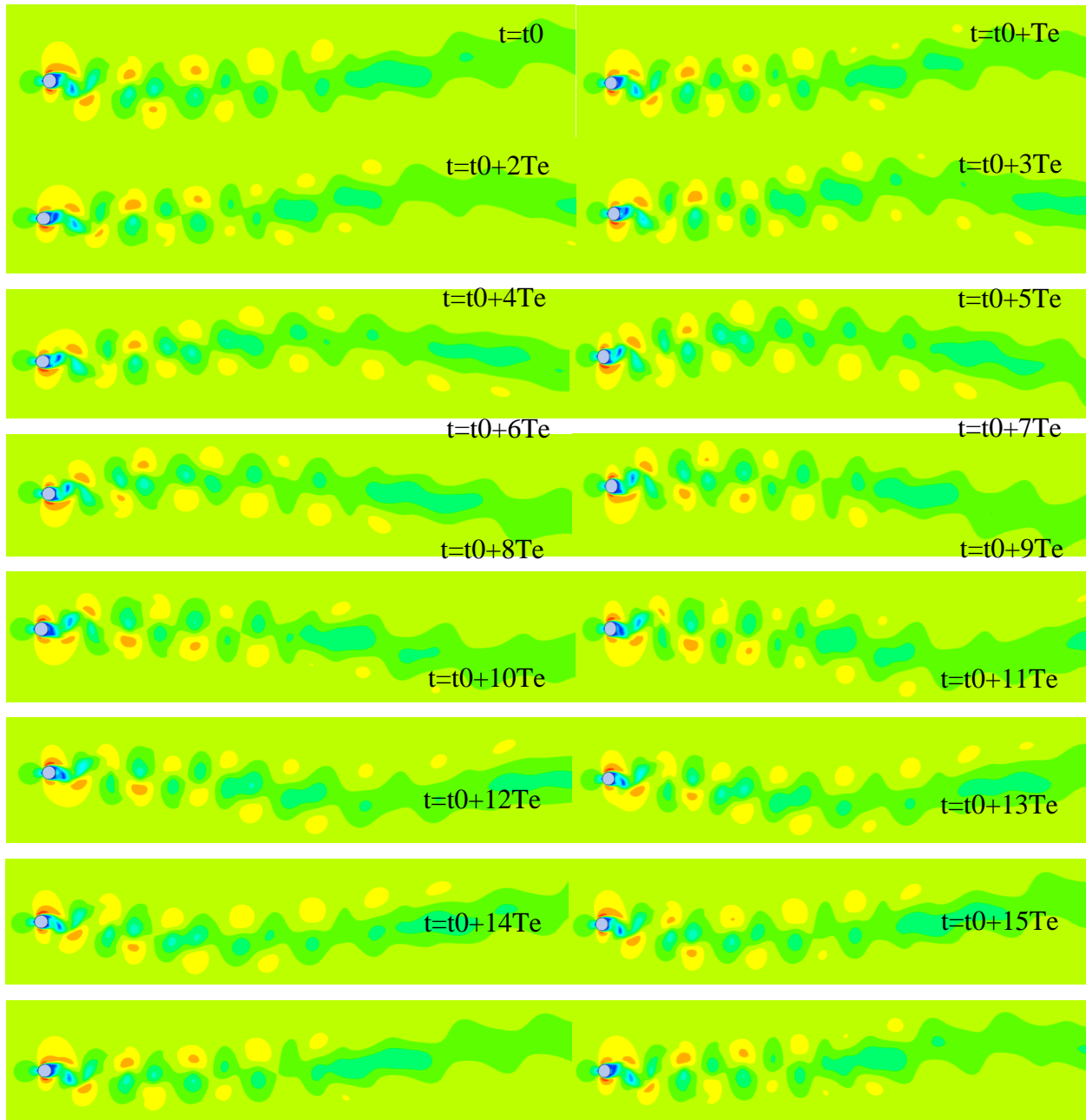


Figure 3-3: The velocity contours for oscillation amplitudes  $A/D = 0.175$  for  $f_e/f_s = 1$  over  $T_b = 15T_c$ .

For  $A/D=0.5$  the snapshots of the wake in terms of the velocity contours over two cylinder oscillation period are plotted. Figures 3-4(d)-3-4(f) show that the spacing between vortices is increased due to the inline oscillation and the velocity contours are the same over two periods of

cylinder motion. This indicates that the 2S mode is locked-on over two periods of the cylinder motion instead of the vortex shedding period.

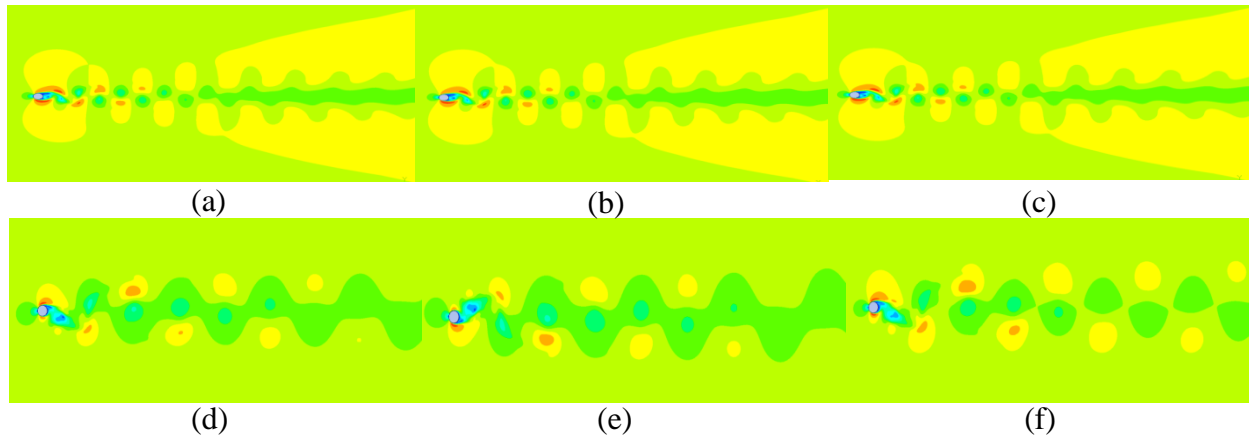


Figure 3-4: The velocity contours for the stationary cylinder (a-c) and forced oscillation amplitudes  $A/D = 0.5$  (d-f) for  $f_e/f_s = 1$  over two oscillation period.

### 3.3.2 Super non-harmonic excitation with $f_e/f_s = 1.5$

The phase plane and power spectrum of the lift coefficient with  $v$ -velocity first mode *chronos* are employed to identify the lock-on region at different oscillation amplitudes. In Figure 3-5(a) the phase plane shows a quasi-stable trajectory due to the presence of a lower frequency at  $fD/U = 0.1$  with respect to the primary frequency at  $fD/U = 0.2$  corresponding to the beating behavior. As it is known from previous studies the non-dimensional frequency  $f_e/f_s = 1.5$  is in the lock-on range for inline oscillation. Thus for  $A/D = 0.175$  the phase portrait exhibits a limit cycle indicating that vortex shedding has locked onto the cylinder motion at a smaller oscillation amplitude with respect to the harmonic oscillation case. The lift coefficient power spectrum given in Figure 3-5(e) does not exhibit any beating behavior, but the signal is modulated by a secondary frequency at  $fD/U = 0.45$  over an oscillation cycle. Since these frequencies are higher than the lock-on frequency  $fD/U = 0.15$ , they do not affect periodicity over the primary lock-on period but deform the shape of each cycle. For  $A/D = 0.5$  synchronized vortex shedding is observed. The phase plane of Figure 3-5(g) therefore shows only one limit cycle with a different shape from the fixed cylinder path. The spectrum of the lift coefficient of Figure 3-5(h) shows that the secondary frequency is energized due to the cylinder motion indicating the competition between symmetric and

asymmetric modes.

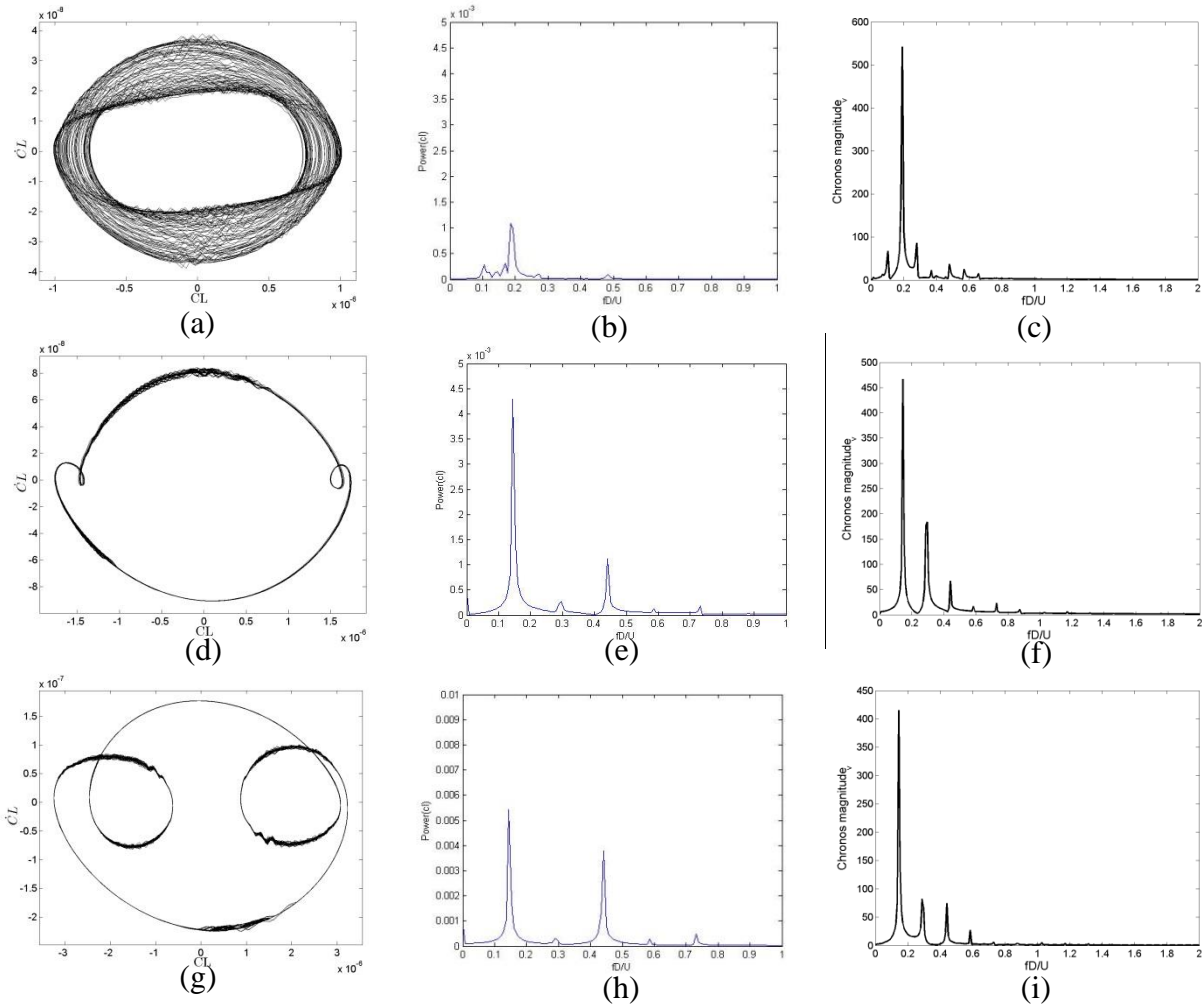


Figure 3-5: Phase plane of the lift coefficient, lift coefficient power spectrum and the  $v$ -velocity first mode *chronos* for (a-c)  $A/D = 0.05$ , (d-f)  $A/D = 0.175$  and (g-i)  $A/D = 0.5$  for  $f_e/f_s = 1.5$ .

The velocity contour visualization for three selected oscillation amplitudes  $A/D = 0.05, 0.175$  and  $0.5$  are presented next. Figures 3-6(a)-3-6(c) displays the velocity contours over two oscillation periods. The snapshots of the streamlines show the quasi-periodic pattern every two oscillation period. The beating behavior is not observed in Figures 3-6(a)-3-6(c) since the low peak at  $fD/U = 0.1$  is weak. Increasing the oscillation amplitude up to  $A/D = 0.175$  the lock-on state is reached. Six vortices are shed over two cycles of oscillation. Two of the vortices develop on the upper side of the cylinder while the third vortex is shed from bottom side per oscillation period. This asymmetric vortex formation is referred to as the P+S mode. This mode breaks the reflection

symmetry and makes it possible to track the side of perturbation initiation.

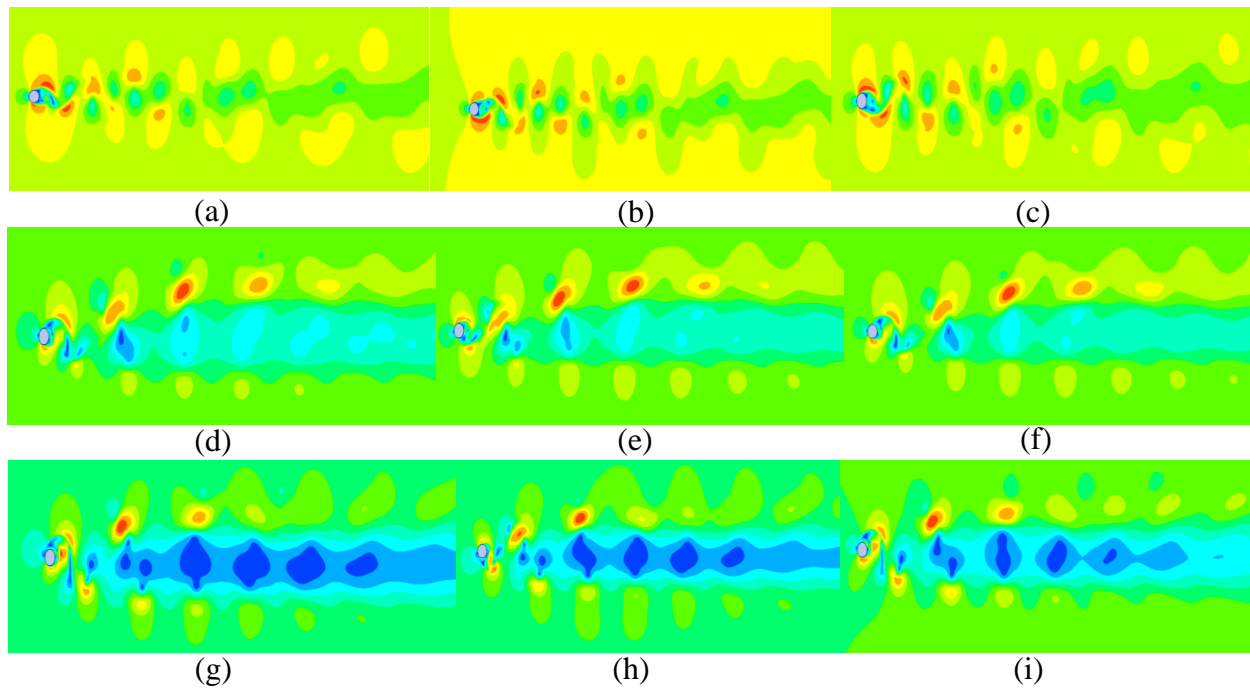


Figure 3-6: Velocity contours for (a-c)  $A/D = 0.05$ , (d-f)  $A/D = 0.175$  and (g-i)  $A/D = 0.5$  for  $f_e/f_s = 1.5$  over two oscillation period.

### 3.3.3 Superharmonic excitation with $f_e/f_s = 2$

The limit cycle of the lift coefficient for  $A/D=0.05$  is shown in Figure 3-7(a) indicating that the beating behavior is eliminated by increasing the frequency ratio in comparison with Figure 3-5(a). As  $f_e/f_s = 2$  is located in the lock-on region, the phase portrait again shows a limit cycle from small amplitude of oscillation. However, the limit cycle shape changes from the simple ellipse to the complex geometry. Figure 3-7(e) shows that the lift coefficient period is twice the cycle of cylinder oscillation which is also confirmed by velocity contours of Figure 3-8. The first peak corresponds to the natural shedding Strouhal number. By increasing the oscillation amplitude to  $A/D=0.5$ , a synchronized pair of vortices is shed as shown in Figures 3-8(g)-3-8(i). The symmetric pattern of the vortex shedding decreases the lift coefficient value to near zero with two frequencies each playing a role in the vortex shedding process. The first peak of the lift coefficient given in Figure 3-7(h) is at  $fD/U = 0.4$  which is equal to the forced oscillation frequency while the second frequency is at  $fD/U = 0.8$ . The first mode *chronos* of Figure 3-7(i) matches well with the

spectrum of the lift coefficient. Although a synchronized vortex shedding is observed it is not a complete lock-on according to the chaotic path on the phase plane with the values almost near zero. The chaotic behavior can be related to the presence of equal forcing and shedding frequencies and also nonlinear coupling between streamwise and transverse velocities.

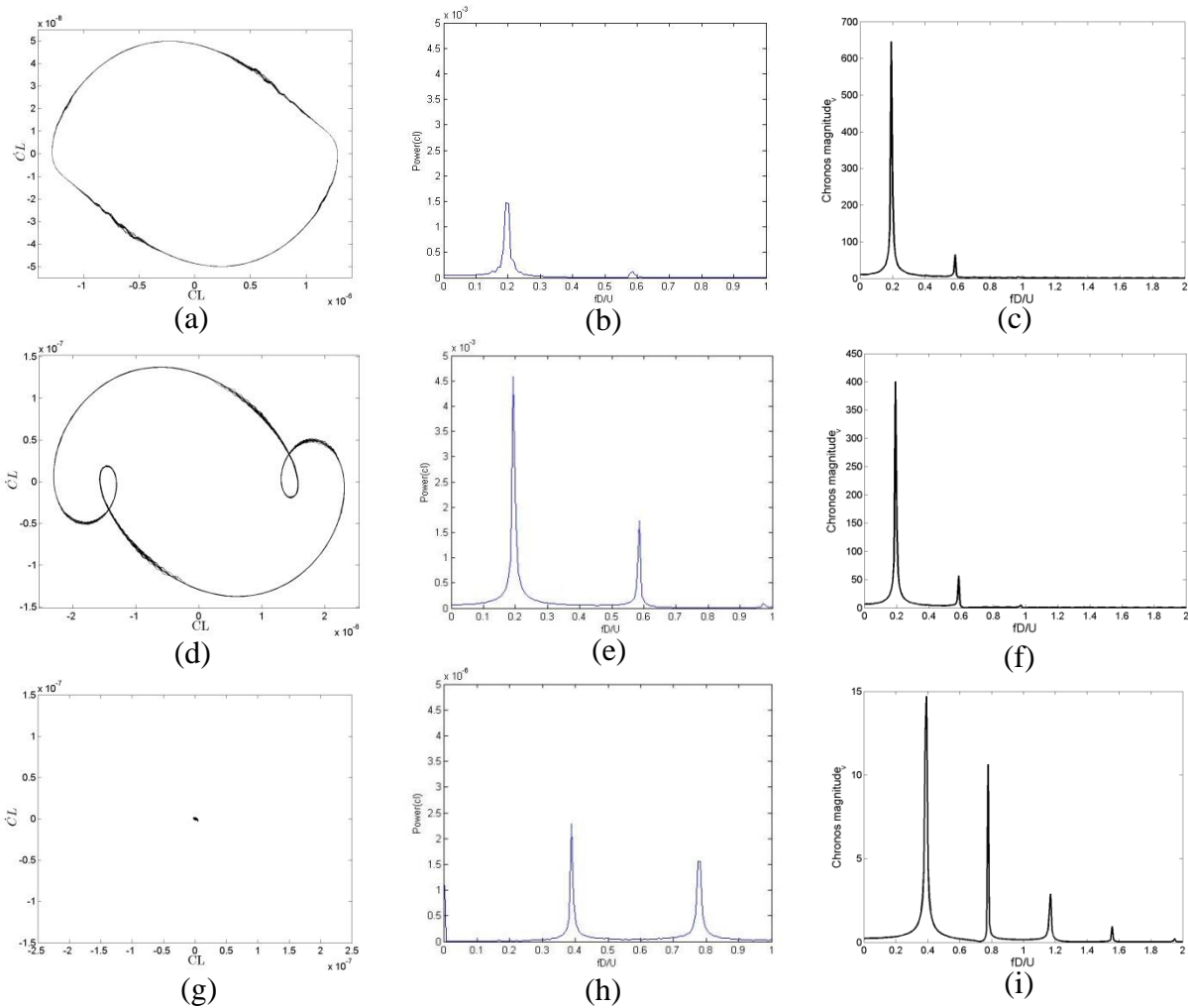


Figure 3-7: Phase plane, power spectrum of the lift coefficient and the  $v$ -velocity first mode *chronos* for (a-c)  $A/D = 0.05$ , (d-f)  $A/D = 0.175$  and (g-i)  $A/D = 0.5$ , for  $f_e/f_s = 2$ .

The velocity contours of Figure 3-8 as well as lift coefficient display the lock-on state of the flow every two periods of cylinder oscillation for  $A/D=0.05$  and  $0.175$ . By increasing the forcing frequency the longitudinal space between vortices decreases and then they are more concentrated than the lower forcing frequency. Consequently the near wake flow is asymmetric but the transition is toward the symmetric mode S. Figures 3-8(g)-3-8(i) show that the vortex shedding pattern

becomes symmetric every oscillation period. The snapshots of velocity streamlines are plotted every half cycle of cylinder oscillation.

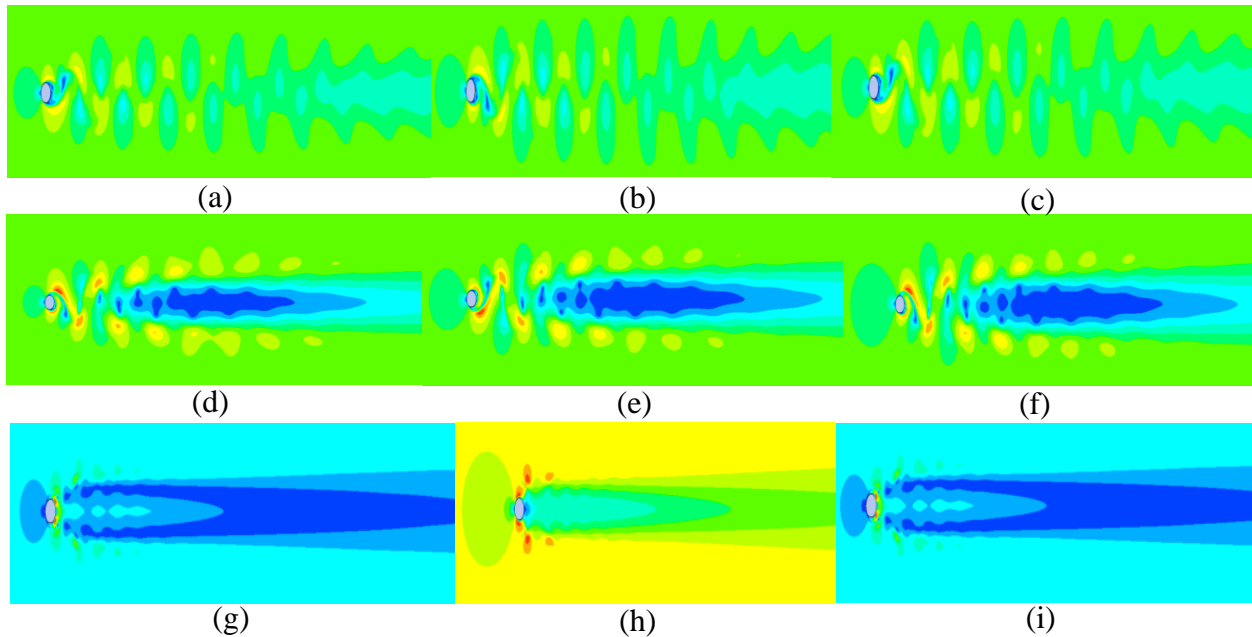


Figure 3-8: Velocity contours with forced oscillation amplitudes (a-c)  $A/D = 0.05$  (d-f)  $A/D = 0.175$  over two oscillation period and (g-i)  $A/D = 0.5$  every oscillation period for  $f_e/f_s = 2$ .

The vortex shedding patterns in terms of the vorticity are also presented for three different frequency ratios  $f_e/f_s = 1, 1.5$  and  $2$  with oscillation amplitude ranging from  $0$  to  $0.5$ . For the harmonic case as shown in Figures 3-9(a)-3-9(c), as the amplitude of oscillation increases the displacement between vortices are increased and thus the wake flow goes under torus-doubling bifurcation. The vorticity contours of non-harmonic excitation given in Figures 3-9(d)-3-9(f) show that for relatively low amplitudes  $A/D = 0.05$  the wake pattern does not seem to change and remains at the basic 2S mode. Further increase in the amplitude causes the alternate peaks to grow leading to the development of the asymmetric P+S mode. The reflection symmetry is broken as will be predicted later by the model. The symmetric S mode is observed in terms of the equivorticity contours for superharmonic forced excitation in Figure 3-9(i). Two symmetric vortices are shed simultaneously every oscillation cycle. The vortex shedding transition depending on the frequency variation is also shown at each of the oscillation amplitudes.

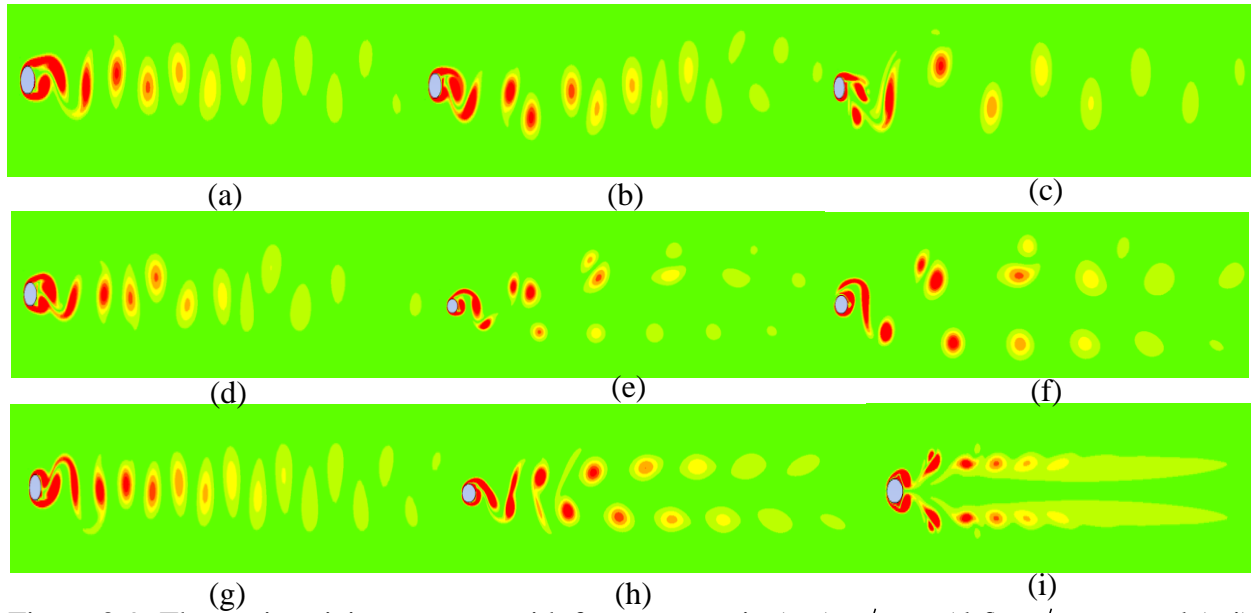


Figure 3-9: The equivorticity contours with frequency ratio (a-c)  $f_e/f_s = 1$  (d-f)  $f_e/f_s = 1.5$  and (g-i)  $f_e/f_s = 2$  for oscillation amplitudes ranging from 0-0.5.

The  $v$ -velocity contours are presented in Figure 3-10. Comparing Figure 3-9(c) and 3-9(i) shows that by increasing the frequency ratio the isovorticity contours represent switching from asymmetric to symmetric pattern while the  $v$ -velocity contours of Figures 3-10(c) and 3-10(i) represent the transition from symmetric to asymmetric mode.

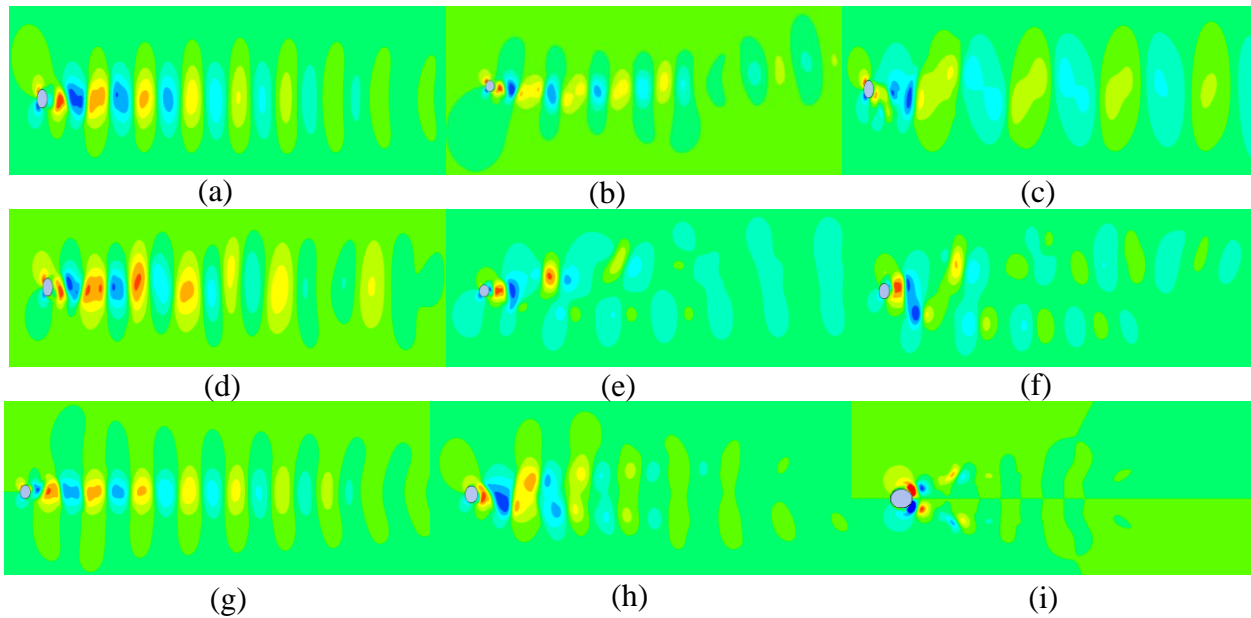


Figure 3-10: The  $v$ -velocity contours with frequency ratios (a-c)  $f_e/f_s = 1$  (d-f)  $f_e/f_s = 1.5$  and (g-i)  $f_e/f_s = 2$  for oscillation amplitudes ranging from 0-0.5.

### 3.4 Derivation of Amplitude Equations Based on Symmetry

Two primary modes of the transverse velocity excited by the cylinder motion are employed to represent the flow dynamics while the other modes are assumed to remain stable. These two primary modes deduced from POD with a wavelength ratio  $\lambda_s/\lambda_k = \omega_k/\omega_s = m/n = 2$  contribute to the one spatial dimensional oscillatory pattern represented as

$$v(x, y, t) = S(t)e^{i(\frac{x}{\lambda_s} + \omega_s t)} f(y) + K(t)e^{i(\frac{x}{\lambda_k} + \omega_k t)} g(y) + h.o.t, \quad (3.3)$$

where  $S(t)$  and  $K(t)$  are time dependent amplitudes of modes corresponding to spatial eigenvectors  $f(y)$  and  $g(y)$ . The approximate symmetry of each mode is defined next. The mode S has symmetries

$$v(x, y, t) = v(x, -y, t) = v(x + \lambda_s, y, t) = v(x, y, t + \tau_s), \quad (3.4)$$

while the K mode satisfies the symmetry group

$$v(x, y, t) = v(x, -y, t + \tau_k/2) = v(x + \lambda_k/2, -y, t) \quad (3.5)$$

where  $\tau_s = 2\pi/\omega_s$ ,  $\tau_k = 2\pi/\omega_k$ . The action of the symmetry group is generated on the amplitudes of primary modes from the requirement that the solution for  $v(x, y, t)$  should be invariant under the action of these symmetries.

$$\begin{aligned} \kappa : y \rightarrow -y &\Rightarrow \kappa(S, K) = (S, -K) \\ T : x \rightarrow x + l\lambda_s &\Rightarrow T(S, K) = (Se^{iml}, Ke^{iml}) \\ \theta : t \rightarrow t + \theta\lambda_s/2\pi &\Rightarrow \theta(S, K) = (Se^{im\theta}, Ke^{im\theta}) \end{aligned} \quad (3.6)$$

The element  $\kappa$  acts through reflection represented as  $Z_2(\kappa)$ .  $T$  acts through translation represented as  $SO(2)$  and  $\theta$  is a phase shift symmetry, shown by  $S^1$ . A steady bifurcation on one-dimensional lattice therefore has  $O(2) \times S^1$  symmetry. Applying the equivariance under translations in  $x$  and  $t$  and reflection  $\kappa$  leads to the invariants  $|S|^2, |K|^2, (K^n \bar{S}^m)^2$  and four equivariants  $(S, K^{2n} \bar{S}^{2m-1}), (K, S^{2m} \bar{K}^{2n-1})$ . The amplitude equations are derived by using these invariants and equivariants.



$$\frac{dS}{dt} = pS + qK^{2n}\bar{S}^{2m-1} \quad (3.7(a))$$

$$\frac{dK}{dt} = rK + s\bar{K}^{2n-1}S^{2m} \quad (3.7(b))$$

where  $p, q, r$  and  $s$  are polynomials based on the invariant functions. The general form of the amplitude equations is truncated up to 7<sup>th</sup> order to include frequency variation and the primary solution branches with maximum subgroups are determined. The amplitude equations expanded up to 7<sup>th</sup> order are

$$\begin{aligned} \frac{dS}{dt} = & [\xi_0 + i\gamma_0 + (\xi_1 + i\gamma_1)|K|^2 + (\xi_2 + i\gamma_2)|S|^2 + (\xi_3 + i\gamma_3)(K\bar{S}^2)^2]S + \\ & [\eta_0 + i\kappa_0 + (\eta_1 + i\kappa_1)|K|^2 + (\eta_2 + i\kappa_2)|S|^2]K^2\bar{S}^3 \end{aligned} \quad (3.8(a))$$

$$\begin{aligned} \frac{dK}{dt} = & [\alpha_0 + i\delta_0 + (\alpha_1 + i\delta_1)|K|^2 + (\alpha_2 + i\delta_2)|S|^2 + (\alpha_3 + i\delta_3)(K\bar{S}^2)^2]K + \\ & [\beta_0 + i\mu_0 + (\beta_1 + i\mu_1)|K|^2 + (\beta_2 + i\mu_2)|S|^2]\bar{K}S^4 \end{aligned} \quad (3.8(b))$$

These complex equations can be rewritten in polar forms by setting  $S = qe^{i\psi}$ ,  $K = re^{i\varphi}$  as

$$\begin{aligned} \frac{dq}{dt} = & [\xi_0 + \xi_1 r^2 + \xi_2 q^2 + (\xi_3 \cos 2\theta - \gamma_3 \sin 2\theta)r^2 q^4]q + \\ & [(\eta_0 + \eta_1 r^2 + \eta_2 q^2) \cos 2\theta - (\kappa_0 + \kappa_1 r^2 + \kappa_2 q^2) \sin 2\theta]r^2 q^3 \end{aligned} \quad (3.9(a))$$

$$\begin{aligned} \frac{dr}{dt} = & [\alpha_0 + \alpha_1 r^2 + \alpha_2 q^2 + (\alpha_3 \cos 2\theta - \delta_3 \sin 2\theta)r^2 q^4]r + \\ & [(\beta_0 + \beta_1 r^2 + \beta_2 q^2) \cos 2\theta + (\mu_0 + \mu_1 r^2 + \mu_2 q^2) \sin 2\theta]r q^4 \end{aligned} \quad (3.9(b))$$

$$\begin{aligned} \frac{d\theta}{dt} = & \delta_0 - 2\gamma_0 + (\delta_1 - 2\gamma_1)r^2 + (\delta_2 - 2\gamma_2)q^2 + [(\delta_3 - 2\gamma_3) \cos 2\theta + \\ & (\alpha_3 - 2\xi_3) \sin 2\theta]r^2 q^4 + [(\mu_0 + \mu_1 r^2 + \mu_2 q^2) \cos 2\theta - (\beta_0 + \beta_1 r^2 + \beta_2 q^2) \sin 2\theta]q^4 - \\ & 2[(\eta_0 + \eta_1 r^2 + \eta_2 q^2) \sin 2\theta + (\kappa_0 + \kappa_1 r^2 + \kappa_2 q^2) \cos 2\theta]q^2 r^2 \end{aligned} \quad (3.9(c))$$

where  $\theta = \varphi - 2\psi$  is a phase difference and thus the system is reduced to be three-dimensional. The fixed points of Eq. (3.9(c)) relate to the periodic solutions while a limit cycle of (3.9(c)) corresponds to the quasi-periodic state.

### 3.4.1 Basic solution branches

The equivariant bifurcation theory is applied to determine the primary solution branches with the maximal subgroups. They are classified into three types: (i) Trivial solution where  $q = r = 0$  (ii) Pure modes, (iii) Mixed modes. Pure mode solutions are given by  $(S, K) = (\sqrt{-\xi_0/\xi_2} e^{i\psi} f(y), 0)$  or  $(S, K) = (0, \sqrt{-\alpha_0/\alpha_1} e^{i\varphi} g(y))$  that are calculated by solving the set of Eq. (3.8) determining the amplitude and phase of the pure mode. The solution has the isotropy subgroup  $\widetilde{SO(2)} \times Z_2(\kappa)$  or  $\widetilde{SO(2)} \times Z_2(\kappa, \pi)$ . The definition of  $\widetilde{SO(2)} = \{(\theta, -\theta): 0 \leq \theta \leq 2\pi\}$  is that a translation through  $\theta$  has the same effect as a phase shift  $-\theta$ . The pure solution branches are travelling waves maintaining their spatio-temporal symmetry while oscillating periodically. Mixed mode solutions can be divided into two types, steady periodic solutions (TW) in the form of  $(qe^{i\psi}, re^{2i\psi})$  deduced by finding the fixed points of Eq. (3.9(c)) and mixed modulated waves (MTW) formed when  $d\theta/dt \neq 0$ . These solutions can be computed by solving the coupled set of Eq. (3.9) numerically. The phase speeds of the travelling mixed modes are then calculated by substituting the values of  $r$  and  $q$  in equations leading to

$$v(x, y, t) = q_{TW} e^{i(k_x x + \omega_s t + \psi_0)} f(y) + r_{TW} e^{i(k_x x + \omega_k t + \varphi_0)} g(y) \quad (3.10)$$

The mixed mode solution has maximum  $\widetilde{SO(2)}$  symmetry subgroup. However, if the amplitude of a mode is much higher than the other, the flow field gets the symmetry of the spatial eigenfunction of the dominant mode unless the amplitude of both modes are almost equal.

### 3.4.2 Coefficients calculation using the $v$ -velocity POD primary modes and bifurcation analysis

The unknown coefficients of the amplitude equations are calculated using the *chronos* of the two first dominant modes of  $v$ -velocity deduced from POD analysis. The Landau coefficients which cover the initial transition until the steady periodic region are calculated for each mode independently at each of the oscillation amplitudes. Since the data is recorded for 40 cycles, the system of Eq. (3.11) is over-determined and the Landau coefficients of mode S can be calculated using least squares method. The Landau coefficients of mode K are obtained by applying the same method.

$$\begin{bmatrix} S_1 & |S_1|^2 S_1 \\ \vdots & \vdots \\ S_i & |S_i|^2 S_i \\ \vdots & \vdots \\ S_{39} & |S_{39}|^2 S_{39} \end{bmatrix} \begin{bmatrix} \xi_0 + i\gamma_0 \\ \xi_2 + i\gamma_2 \end{bmatrix} = \begin{bmatrix} S_2 - S_1 \\ \vdots \\ S_{i+1} - S_i \\ \vdots \\ S_{40} - S_{39} \end{bmatrix} \quad (3.11)$$

The coupling coefficients are also determined by the least squares method. These coefficients are calculated at the oscillation amplitudes where for the first time mode K is observed and the last time that mode S occurs. Then, the known Landau coefficients of mode S for  $A/D=0.5$ , obtained from Eq. (3.11), are substituted in the Eq. (3.12) and the coupling coefficients are calculated from the over-determined system of Eq. (3.12). Applying the same method for the fixed cylinder case, the coupling coefficients of the K mode are achieved. Thus the critical amplitude for mode K is the fixed cylinder case, where mode K is weak and for mode S for  $A/D=0.5$  where its energy is reduced. The deduced coefficients are presented in Table 3-1.

$$\begin{bmatrix} |K_1|^2 S_1 & (K_1 \bar{S}_1)^2 S_1 & K_1^2 \bar{S}_1^3 & |K_1|^2 K_1^2 \bar{S}_1^3 & |S_1|^2 K_1^2 \bar{S}_1^3 \\ \vdots & \vdots & \vdots & \vdots & \vdots \\ |K_i|^2 S_i & (K_i \bar{S}_i)^2 S_i & K_i^2 \bar{S}_i^3 & |K_i|^2 K_i^2 \bar{S}_i^3 & |S_i|^2 K_i^2 \bar{S}_i^3 \\ \vdots & \vdots & \vdots & \vdots & \vdots \\ |K_{39}|^2 S_{39} & (K_{39} \bar{S}_{39})^2 S_{39} & K_{39}^2 \bar{S}_{39}^3 & |K_{39}|^2 K_{39}^2 \bar{S}_{39}^3 & |S_{39}|^2 K_{39}^2 \bar{S}_{39}^3 \end{bmatrix} \begin{bmatrix} \xi_1 + i\gamma_1 \\ \xi_3 + i\gamma_3 \\ \eta_0 + i\kappa_0 \\ \eta_1 + i\kappa_1 \\ \eta_2 + i\kappa_2 \end{bmatrix} = \begin{bmatrix} S_2 - S_1 - [(\xi_0 + i\gamma_0)S_1 + (\xi_2 + i\gamma_2)|S_1|^2 S_1]_{A/D=0.5} \\ \vdots \\ S_{i+1} - S_i - [(\xi_0 + i\gamma_0)S_i + (\xi_2 + i\gamma_2)|S_i|^2 S_i]_{A/D=0.5} \\ \vdots \\ S_{40} - S_{39} - [(\xi_0 + i\gamma_0)S_{39} + (\xi_2 + i\gamma_2)|S_{39}|^2 S_{39}]_{A/D=0.5} \end{bmatrix} \quad (3.12)$$

Table 3-1: The coefficients of the amplitude equation deduced from the least square method

	$\xi_0 + i\gamma_0$	$\xi_1 + i\gamma_1$	$\xi_2 + i\gamma_2$	$\xi_3 + i\gamma_3$	$\eta_0 + i\kappa_0$	$\eta_1 + i\kappa_1$	$\eta_2 + i\kappa_2$
S	0.0926-0.08i	0.0-85.57i	-2.04+1.39i	985.32-3281.8i	-720.41+197.49i	95977+37561i	985.32-3281.8i
	$\alpha_0 + i\delta_0$	$\alpha_1 + i\delta_1$	$\alpha_2 + i\delta_2$	$\alpha_3 + i\delta_3$	$\beta_0 + i\mu_0$	$\beta_1 + i\mu_1$	$\beta_2 + i\mu_2$
K	0.25+0.25i	-80.63-37.59i	-4.15-5.98i	-198880+20991i	-57.45+2.96i	64593+115600i	819.87-427.48i

The real parts of both modes approximated from the amplitude equations are plotted in Figure 3-11. Both the frequency and amplitude of the modes match well with the simulation results. The linear terms of the amplitude equations are affected most by the inline cylinder motion and thus considered as the bifurcation parameters while the other coefficients remain unchanged. Now by variation of the linear bifurcation parameters obtained from numerical computations, the solution branches can be determined.

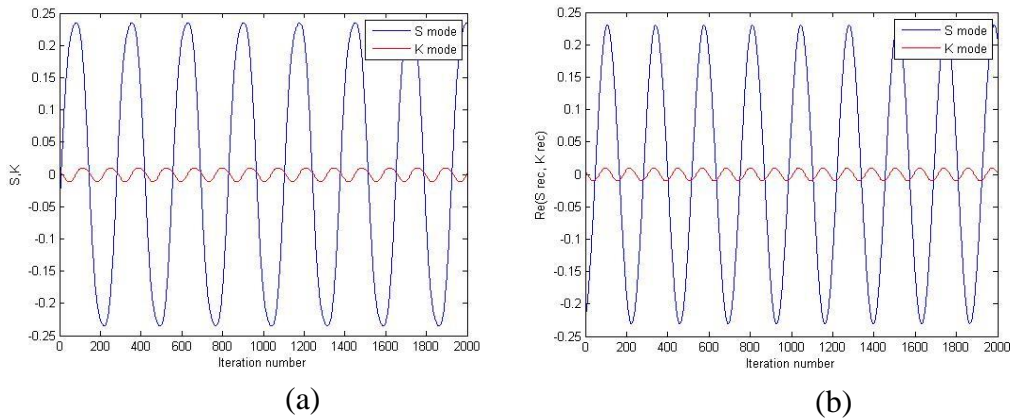


Figure 3-11: (a) The *chronos* of modes S and K from CFD, (b) Deduced S and K modes approximated from the least square method of the dominant *chronos* data.

For the harmonic case, as the amplitude of oscillation increases,  $\xi_0$  decreases,  $\delta_0$  increases while  $\gamma_0, \alpha_0$  remain fixed. Therefore, the mixed modes go under the bifurcation by smooth variation of these two parameters  $\xi_0$  and  $\delta_0$ .

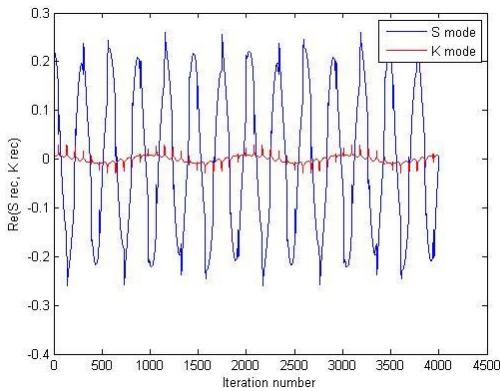


Figure 3-12: Quasi-periodic state of modes S and K at  $\xi_0 = 0.0836$  and  $\delta_0 = 0.29$

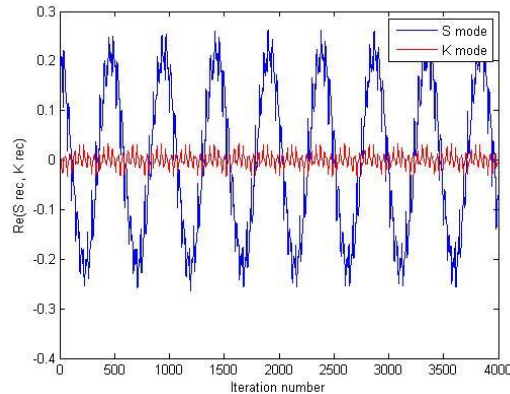


Figure 3-13: Quasi-periodic state of modes S and K at  $\xi_0 = 0.0826$  and  $\delta_0 = 0.46$ .

The steady travelling waves of Figure 3-11 lose stability at  $\xi_0 = 0.0836$  and  $\delta_0 = 0.29$  as shown in Figure 3-12. As the torus doubling bifurcation is approached at  $\xi_0 = 0.0826$  and  $\delta_0 = 0.46$ , two period-doubled tori are deduced as plotted in Figure 3-13. The modes bifurcating due to the harmonic inline oscillation are modulated travelling waves with  $\widetilde{SO}(2)$  symmetry. As shown in Figure 3-13 the bifurcated mode S has higher energy with respect to the larger amplitude value in comparison with the bifurcated mode K. Thus the flow field gets the reflection symmetry of the dominant spatial eigenfunction  $Z_2(\kappa)$ . The approximate symmetry for harmonic case is  $Z_2(\kappa) \times \widetilde{SO}(2)$ .

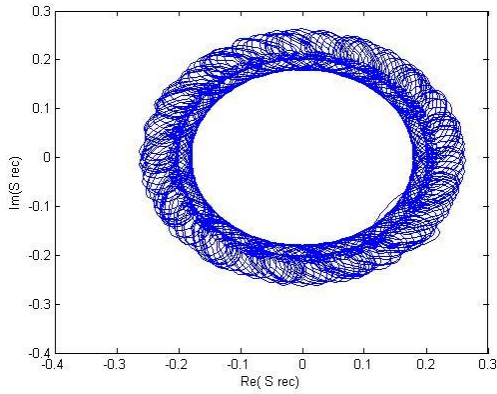


Figure 3-14: Complex amplitude of bifurcated mode S at  $\xi_0 = 0.0826$ ,  $\delta_0 = 0.46$ .

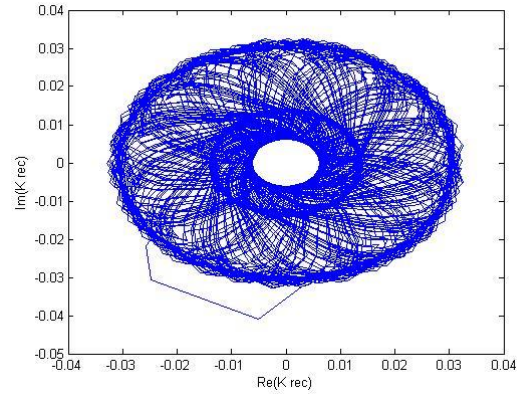


Figure 3-15: Complex amplitude of bifurcated mode K at  $\xi_0 = 0.0826$ ,  $\delta_0 = 0.46$ .

Next, the bifurcation analysis is considered for super non-harmonic excitation with the assumption that the forcing frequency variation, in addition to the oscillation amplitude changes, only affects the linear terms of the model. Then for forcing frequency ratio  $f_e/f_s = 1.5$ , the solution branch is deduced by calculating the variation of two linear terms  $\xi_0$  and  $\delta_0$  considered as bifurcation parameters. The mixed modulated modes are deduced from torus bifurcation at  $(\xi_0, \delta_0) = (0.0726, 0.26)$  due to the cylinder motion. However, the forcing frequency variation affects the other linear terms too e.g. at  $\xi_0 = 0.001, \gamma_0 = 0.0, \alpha_0 = 0.018$  and  $\delta_0 = 0.04$  two steady modes with primary dimensionless lock-on frequency 0.15 are found as given in Figure 3-17.

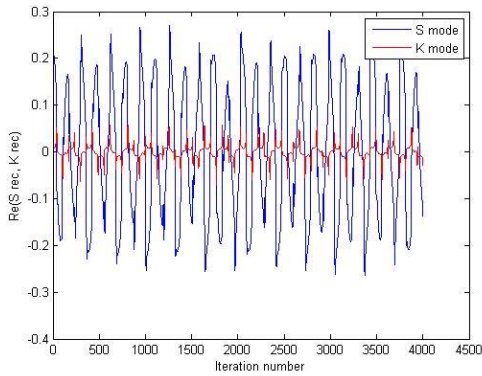


Figure 3-16: Quasi-periodic state of modes S and K at  $\xi_0 = 0.0726, \delta_0 = 0.26$ .

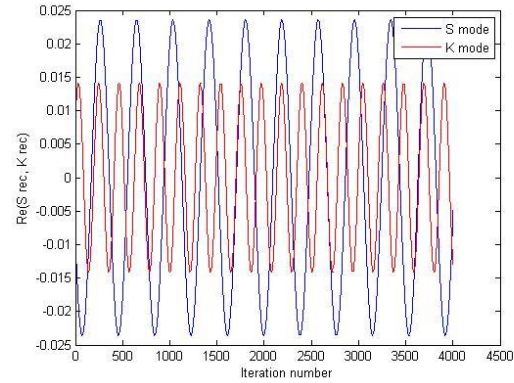


Figure 3-17: steady bifurcated modes S and K at  $\xi_0 = 0.001, \gamma_0 = 0.0, \alpha_0 = 0.018$  and  $\delta_0 = 0.04$ .

But the presence of higher harmonics shown in the phase portrait of Figure 3-5(g) which deforms the shape of the limit cycle is not observed in the modes of Figures 3-16 and 3-17. This shows that the nonlinear terms may also be affected by frequency variation. Two tori result from the Hopf bifurcation are shown in Figures 3-18 and 3-19. As the second mode amplitude increases, there is a competition between symmetric and asymmetric modes. Thus the deduced solution branch has symmetry  $\widetilde{SO}(2)$  which shows that the forced excitation breaks the reflection symmetry.

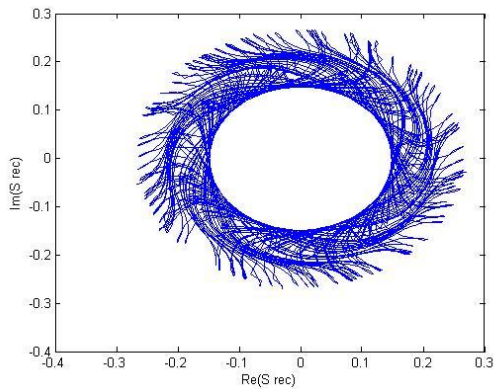


Figure 3-18: Complex amplitude of bifurcated mode S at  $\xi_0 = 0.0726, \delta_0 = 0.26$ .

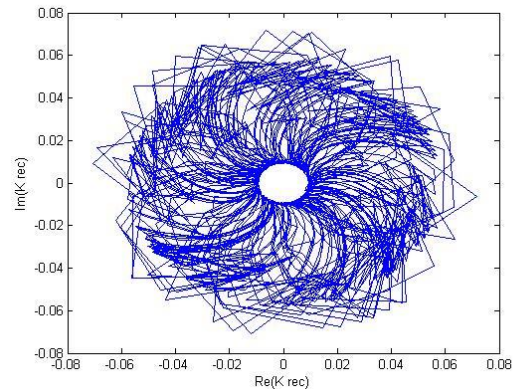


Figure 3-19: Complex amplitude of bifurcated mode K at  $\xi_0 = 0.0726, \delta_0 = 0.26$ .

Finally, the bifurcation analysis for the superharmonic excitation with frequency ratio  $f_e/f_s = 2$  is considered. Figure 3-20 shows two travelling waves created from two bifurcation parameters at  $(\xi_0, \delta_0) = (-0.0606, 0.17)$ .

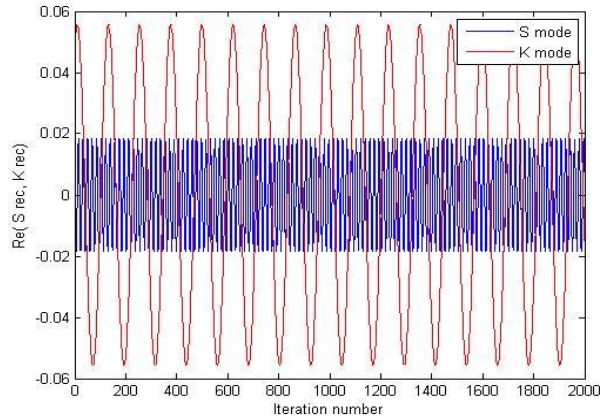


Figure 3-20: Steady bifurcated S and K modes at  $\xi_0 = -0.0606$ ,  $\delta_0 = 0.17$ .

It is clear from Figure 3-20 that the K mode with its spatio-temporal reflection symmetry is dominant similar to the asymmetric  $v$ -velocity contours of Figure 3-10(i) observed in the numerical results. Thus for superharmonic excitation the approximate symmetry group is  $Z_2(\kappa, \pi) \times \widetilde{SO}(2)$ . As shown in Figure 3-7(g) the lift coefficient becomes chaotic with respect to the presence of equal forcing and shedding frequencies and nonlinear couplings of inline and transverse velocities. The dominant frequency of the mode K is predicted well however the second mode frequency cannot be modeled with variation of only two bifurcation parameters.

### 3.5 Conclusion

The lock-on flow regime is investigated by phase plane and power spectra of lift coefficient, transverse velocity and equivorticity contours. Two-dimensional numerical computations are conducted for  $Re=200$ ,  $A/D=0.0-0.5$  and  $f_e/f_s = 1, 1.5$  and  $2$ . The vortices are shed in various vortex shedding modes and there is no deviation from the  $x$ -axis, thus the  $v$ -velocity first mode *chronos* is a good representative of the lift coefficient frequency which is confirmed in numerical results. As the vorticity contains both the streamwise and transverse velocity effects, the *chronos* of first vorticity mode may give a better approximation of the shedding frequency.

A model is developed to analyze the vortex shedding mode interactions using equivariant bifurcation theory. The torus-doubling bifurcation for harmonic excitation, the mode competition for super non-harmonic case with  $f_e/f_s = 1.5$  which leads to the reflection symmetry breaking and for superharmonic case with  $f_e/f_s = 2$  switching of the dominant eigenfunction reflection

symmetry are all well predicted with the proposed model. However, the frequency of the second mode does not match for superharmonic cases, which shows that more than two linear bifurcation terms should be involved for more precise modeling. Involving more than two bifurcation parameters could uncover the complexity of the nonlinear vortex shedding mode interaction.

For superharmonic excitation cases, the lock-on occurs within the oscillation amplitude ranges of [0.175-0.5], a much larger range than the one found for the harmonic case. It is shown that the lock-on range widens with the increase of amplitude, reflecting the dominance of the oscillatory motion by increasing amplitude. For the harmonic case, by increasing the oscillation amplitude, the second peak takes a lower frequency than the dominant peak and the beating phenomenon is observed. Thus the flow is not periodic over the lock-on period but over several periods equal in total, to the beating period. However, for the super non-harmonic case, the second peak has higher frequency than the first peak which modulates the signal during the oscillatory frequency. The flow in superharmonic case remains periodic over one cycle but with some fluctuations due to the presence of the secondary peak.

Symmetric and asymmetric lock-on modes are observed for three different oscillation amplitudes and frequency ratios. The lock-on asymmetric 2S mode when  $f_e/f_s = 1$  for  $A/D=[0.35-0.5]$ , P+S mode with  $f_e/f_s = 1.5$  for  $A/D=[0.175,0.5]$  and symmetric S mode with  $f_e/f_s = 2$  for  $A/D=[0.175,0.5]$  are verified. Increasing the frequency ratio from harmonic to superharmonic for  $A/D=0.5$  causes the vortex shedding mode to switch from asymmetric to symmetric mode while the transverse velocity pattern changes from symmetric to asymmetric. The lift coefficient decreases as the symmetric mode develops in the wake. The obtained numerical results are in good agreement with previous experimental observations.



## Chapter 4 **ARTICLE 3: POD ANALYSIS OF THREE-DIMENSIONAL FORCED HARMONIC INLINE WAKE FLOW OF A CIRCULAR CYLINDER**

Nabatian N., Xu X. and Mureithi N. W. (2014) submitted to “Transactions of the Canadian Society for Mechanical Engineering, TCSME” in April 23, 2014.

### **Abstract**

A three-dimensional numerical simulation of a circular cylinder wake is presented in this paper. The cylinder is harmonically forced in the streamwise direction. The results are compared with a previous two-dimensional CFD model. The objective of the present work is to investigate the effect of the oscillation amplitude on the secondary transition of the wake. The wake characteristics are analyzed using the aerodynamic coefficients. The lift and drag coefficient frequencies computed from 3D simulations agree well with the previous 2D model and other experimental results. Both two and three-dimensional simulations of the unsteady wake flow using an immersed-boundary method in a fixed Cartesian grid predict the flow dynamics well. The frequency of the lift force is then linked to the form of the vortex shedding mode. The relation between these vortex shedding modes using POD analysis of the transverse velocity and the unsteady lift coefficient of 3D simulation is in good agreement with the 2D model. Results show that the three-dimensional spanwise effect, which can change the wake structure, is suppressed at  $Re=200$  by streamwise oscillation of the cylinder. Thus the 2D analysis can effectively model the temporal instability of the wake flow.

**Keywords:** secondary transition; immersed-boundary method; temporal instability.

### **ANALYSE POD TRIDIMENSIONNELLE DE L'ÉCOULEMENT DU SILLAGE EN LIGNE FORCÉ D'UN CYLINDRE CIRCULAIRE**

### **RÉSUMÉ**

Dans cet article, une simulation numérique tridimensionnelle de l'écoulement dans le sillage d'un cylindre circulaire est présentée. Le nombre de Reynolds ( $Re$ ) considéré est égal à 200. On force une oscillation harmonique en ligne du cylindre. Les résultats prédits par cette simulation sont comparés avec notre modèle

CFD bidimensionnelle antérieur. L'objectif de ce travail est d'étudier l'effet de l'amplitude des oscillations sur la transition secondaire du sillage. Les caractéristiques du sillage sont analysées en utilisant les coefficients aérodynamiques. Les fréquences des coefficients de portance et de traînée calculés à partir de simulations 3D sont en général en accord avec les résultats du modèle 2D ainsi qu'avec quelques mesures expérimentales trouvées dans la littérature. Les simulations instationnaires tridimensionnelles et bidimensionnelles de l'écoulement dans le sillage utilisent des conditions aux frontières immergées dans une grille cartésienne fixe. Les prédictions de la dynamique d'écoulement sont assez précises. La fréquence de la force de portance est reliée à la forme du mode de décollement tourbillonnaire. La relation entre les modes de décollement tourbillonnaire et le coefficient de portance instationnaire de la simulation 3D a été analysé grâce à l'analyse POD de la vitesse transverse. Les résultats 2D et 3D sont en bon accord. Nos calculs montrent que les effets *spanwise* tridimensionnels, affectant la structure de sillage, sont supprimés à  $Re = 200$  par l'oscillation en ligne du cylindre. Par conséquent, l'analyse 2D est suffisante pour modéliser l'instabilité temporelle du sillage d'un cylindre circulaire.

**Mots-clés :** transition secondaire ; conditions aux frontières immergées; Instabilité temporelle.

## 4.1 Introduction

Flow around a circular cylinder is studied to understand the bluff body wake complex dynamics as it has a large application in many industries. Different flow regimes are classified depending on Reynolds number. At low Reynolds number, the flow field is symmetric. As the Reynolds number increases, the first instability causes the flow to separate behind the cylinder causing vortex shedding. This is the first 2D transition that creates a periodic flow from the steady wake. For  $40 < Re < 200$ , laminar vortex shedding occurs in the wake of the cylinder. Secondary transition of the wake flow occurs at approximately  $Re=200$ , where the three-dimensional effects are observed in the flow. The vortex shedding induces fluctuating drag and lift that cause the structure to vibrate when synchronized to the structural resonant frequency. This is known as vortex induced vibration (VIV) and can lead to structural failures (Blackburn and Henderson, 1999; Blackburn et al., 2004a; Thompson et al., 2001; Williamson, 1996). Numerous experimental and numerical studies have been performed to improve the understanding and prediction of cylinder VIV behavior. The forced oscillation of the cylinder is one of the approaches to study and control vortex shedding. When the cylinder oscillates at a given frequency, it interacts with the vortex shedding process. For forced oscillations in a specific range of amplitude and frequency, the cylinder motion is able to control the instability mechanism arising from the vortex shedding. One of the characteristics of fluid-

structure interactions is lock-on between vortex shedding and structure vibration in which the vortex shedding frequency diverges from natural shedding frequency and becomes equal to the forced oscillation frequency. This approach is used to study the phenomenon of VIV where the wake flow causes the cylinder to oscillate at its natural frequency at a higher Reynolds number (Atluri et al., 2009; Borggaard et al., 2007; Bruneau and Mortazavi, 2006; Carberry et al., 2004; Constantinides and Oakley, 2006; Do et al., 2011; Konstantinidis et al., 2007; Morse and Williamson, 2006; Morse and Williamson, 2009; Srikanth et al., 2011; Xu et al., 2006; Zheng and Zhang, 2008).

Several studies have been conducted to investigate the oscillation effect on the transition of the 3D wake (Barkley et al., 2002; Buffoni et al., 2006; Kaiktsis et al.). Williamson, (1996) showed that at the transition Reynolds number,  $Re \approx 200$ , three-dimensional flow effects appear which are shown by a hysteretic discontinuity in the Strouhal number values. Due to this phenomenon, there is a reduction in the Strouhal number followed by an increase up to  $Re=300$ . It has been demonstrated that the three-dimensionality of the cylinder wake can be delayed by forcing the cylinder to oscillate at moderate amplitudes. Koopman, (1967) and Griffin and Ramberg, (1974) showed that the wake flow is two-dimensional at oscillation amplitudes above  $0.1D$  for Reynolds number up to 300-400. Berger, (1967) showed via an experimental study that by applying a controlled transverse oscillation with frequencies that synchronize the wake fluctuations, a laminar vortex-shedding regime can be extended until  $Re=300-350$ . Thus, the flow can be assumed to be two-dimensional. Later, Gioria and Meneghini, (2010) presented direct numerical simulations of forced wake flow behind a circular cylinder. The threshold amplitude in which the three-dimensionality is suppressed is in the range of  $0.03D < A < 0.65D$  for  $Re=200$ . The transverse oscillations inhibit the growth of three-dimensional fluctuations; hence the wake flow remains two-dimensional in this amplitude range.

The present study numerically investigates the three-dimensional wake flow past a circular cylinder forced to oscillate inline to the free-stream. The numerical simulations are performed for a range of oscillation amplitudes extended up to  $0.5D$  with frequency equal to natural shedding frequency at  $Re=200$ . By changing the oscillation amplitude, the wake flow undergoes several transition regions and states. The objective of the present work is to investigate the effect of inline oscillation of the cylinder on the wake dynamics using 3D simulations. The results are compared with

previously obtained 2D numerical results to verify the two-dimensional wake flow assumption at  $Re=200$  by considering the inline oscillation.

## 4.2 Numerical computations

### 4.2.1 Methodology

The computational domain is extended 40D downstream, 15D upstream and 20D cross-stream on each side. A no-slip condition is imposed on the cylinder surface and symmetry conditions are employed for the lateral boundaries, whereas the pressure outlet is used for the outlet condition. A structured mesh of Figure 4-1(a) with 109692 elements corresponding to 220648 nodes is used for 2D simulation. A 3D mesh is constructed with 3433440 nodes and 3344828 elements with considerable mesh concentration around the cylinder and the wake shown in Figure 4-1(b).

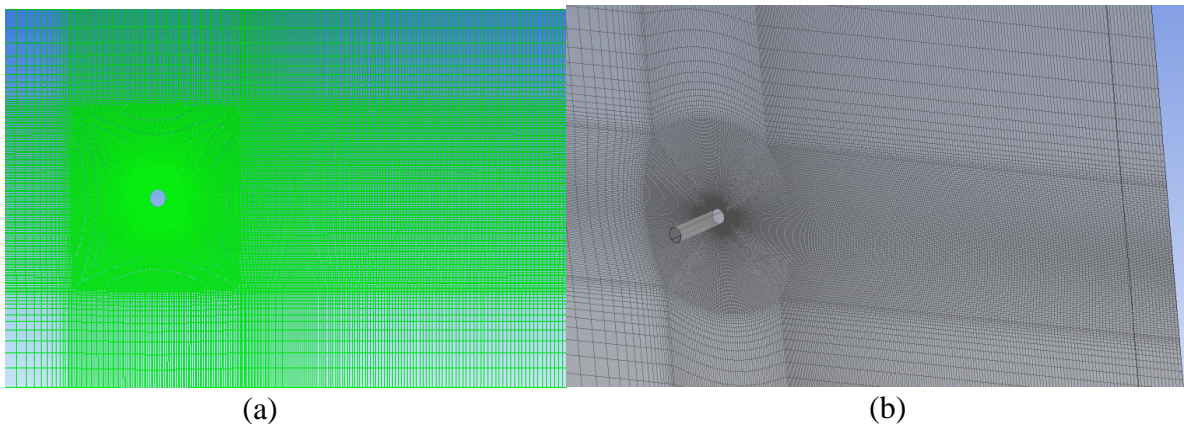


Figure 4-1: (a) Schematic of the mesh for 2D domain, (b) Schematic of the mesh for 3D domain

The immersed boundary method is applied. To simulate the forced inline oscillation of the wake flow in the stationary coordinate system an extra acceleration term and mass source/ sink terms are added to the momentum and continuity equations. The forced oscillation is implemented as a boundary condition that is equivalent to subjecting the rigid cylinder to an oscillating flow. At the inlet boundary a sinusoidal velocity is prescribed as  $u(t) = U + A\omega\sin(\omega t)$ , where  $A$  is the non-dimensional amplitude of oscillation,  $\omega = 2\pi f_e$  is the oscillation frequency with  $f_e/f_s = 1$  and  $u(t)$  is the streamwise component of fluid velocity.

The Navier-Stokes equations are solved using the implicit hybrid finite-element/finite-volume approach to achieve the pressure-velocity coupling. Advection fluxes are evaluated with a

calculated blending factor using second-order accurate high resolution scheme while a second-order accurate backward Euler scheme is used for time discretization. The shear-stress transport (SST)  $k - \omega$  model is employed to account for the transport of the principle turbulent shear stress. In the SST  $k - \omega$  model the standard  $k - \omega$  model and transformed  $k - \varepsilon$  model are both multiplied by a blending function. This function is designed to approach one in the near wall region which activates the standard  $k - \omega$  model and zero away from the surface which activates the transformed  $k - \varepsilon$  model. A constant time step,  $dt = 0.0078$  is used for simulation of the unsteady wake flow which is twice the 2D simulation time step. The resolution and convergence tests have been conducted for the stationary cylinder case in the previous study. The detailed results of the comparison, the Strouhal number and non-dimensional aerodynamic coefficients, for grid-dependence study were presented in previous publications (Mureithi et al., 2010; Mureithi and Rodriguez, 2005).

#### 4.2.2 POD Analysis of the transverse velocity

The transverse velocity of the forced wake flow is extracted on a square plane with 10D dimension and 51 sampling points on each side at 21 selected planes in the  $z$ -direction. The recorded data for 40-cycles is then stored in a matrix A. POD is used to develop the low order dynamical model of the wake flow which optimally contains the dominant energy of the  $v$ -velocity perturbations by minimizing the error (Druault and Chaillou, 2007; Graham et al., 1999; Kerschen et al., 2005; Rowley, 2005). The 3D POD analysis is performed using the snapshots of  $v(x, y, z, t_k)$  at  $N_k$  discrete time instants of the last 40 steady periods. The mean-flow field is subtracted to find the velocity perturbation value as in Eq. (4.1) and the results are stored in a matrix A.

$$v'(x, y, z, t) = v(x, y, z, t) - v_m(x, y, z, t), \quad (4.1)$$

Since the dimension of the spatial discretization of the flow field is higher than the snapshots, the POD modes of the perturbation velocity field are computed using the time correlation tensor. The time correlation tensor is defined as

$$[R]_{ijk} = \frac{1}{n_1 n_2 n_3} \sum_{l=1}^{n_1} \sum_{m=1}^{n_2} \sum_{q=1}^{n_3} V(X_{lmq}, t_i) V(X_{lmq}, t_j) V(X_{lmq}, t_k) \quad (4.2)$$

where  $n_1 \times n_2$  is the number of total grid points in the  $x$ - $y$  plane at  $n_3$   $z$ -coordinates,  $V$  is the transverse velocity vector and  $X$  is the space variable. The POD coefficients  $a^{(n)}$  are deduced from

this correlation matrix by solving the eigenvalue problem  $RA = \lambda A$  where  $\lambda^n$  corresponds to the energy contained within the  $n$ th POD mode. Thus solving the  $N_k \times N_k$  eigenvalue problem is more efficient than  $n \times n$  eigenvalue equation as the number of snapshots  $N_k$  is smaller than the number of states  $n$ . The eigenfunctions are deduced from the Galerkin-projection of the instantaneous velocity field onto the corresponding POD coefficients. The instantaneous transverse velocity field is then reconstructed as

$$v(X, t) = \sum_{n=1}^{N_{mode}} a^{(n)}(t) \psi^{(n)}(X) \quad (4.3)$$

where  $N_{mode}$  is the total number of POD modes. The  $\psi^{(n)}$  is the set of orthogonal spatial modes and  $a^{(n)}$  is the set of modal coefficients. For 2D flow, the POD modes can be calculated using the recorded data of the  $v$ -velocity perturbations at 100 nodes on the line 10D downstream of the flow for 40 steady cycles. The transverse velocity values are transformed into complex form by Hilbert transformation. The mean value is subtracted and the singular value decomposition (SVD) is applied to find the decomposed perturbation velocity as

$$v'(y, t) = \sum_{k=1}^{100} a_k(t) \psi_k(y), \quad (4.4)$$

where each mode includes a spatial eigenvector  $\psi_k(y)$ , called *topos* and a temporal one  $a_k(t)$ , called *chronos*. The *chronos*  $a_k(t)$  describes the time history of each point velocity while  $\psi_k(y)$  represents the velocity profile of 100 points at a specific time. The matrix A (5500,100) for each case of the forced oscillation is processed by SVD to identify the *topos* and *chronos* of the primary modes. The different *topos* and *chronos* created at various amplitudes of oscillation show different behaviors of the flow field, affected by the cylinder oscillations. Since POD gives the normalized *topos*, *chronos* contains the amplitude evolution of the mode.

### 4.3 Results

The structure of the wake flow is studied using the transverse velocity streamlines. Physical quantities such as lift and drag coefficients are computed and compared with the 2D numerical results. The power spectra of the lift and drag coefficients for the stationary cylinder are computed using data in the last 40 steady periods as shown in Figure 4-2(b). The lift frequency represents the natural shedding frequency at  $St = 0.1975$  and the primary frequency in the drag direction

corresponds to twice the vortex shedding frequency at  $fD/U = 0.395$  since two vortices are created in each oscillation cycle. There is significant coupling between lift and drag coefficients as the drag frequency is twice the lift frequency. The measured dominant frequencies for lift and drag coefficients are in comparison with  $fD/U = 0.1945$ ,  $fD/U = 0.385$  obtained from the 2D simulation. The 3D results have a good agreement with the 2D model. Despite a better agreement in the drag coefficient, the lift coefficient amplitude of the 2D simulation is higher than the 3D lift as the three-dimensional effects which reduce the force are not considered in two-dimensional simulation.

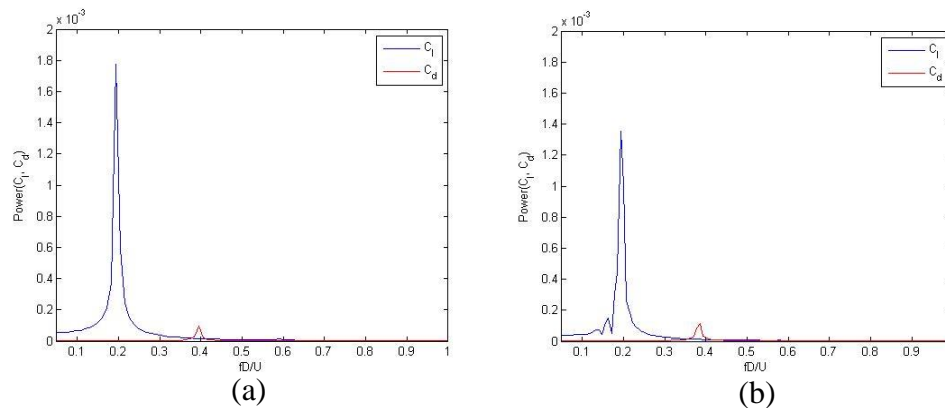


Figure 4-2: The spectra of the lift and drag coefficients for (a) 2D simulation, (b) 3D simulation.

The forced harmonic oscillation alters the lift coefficient dynamics from a steady state. The fluctuating lift coefficient is directly related to the vortex shedding pattern in the wake. The time histories and power spectra of the lift coefficient at the various oscillation amplitudes for the harmonic case are plotted in Figure 4-3. For the stationary cylinder case, the lift coefficient is characterized by a pure sinusoidal response. The spectrum of the lift coefficient presented in Figure 4-3(a) confirms this sinusoidal response with a single peak at  $fD/U = 0.1975$ . Additionally, a limit cycle is observed in the lift coefficient phase portrait of Figure 4-3(c). Increasing the oscillation amplitude, the quasi-periodic state appears at  $A.D=0.175$  where  $fD/U = 0.2$  is the main frequency with the presence of the lower frequency at  $fD/U = 0.016$  in  $C_l$  signal. The time series of the lift coefficient is no longer sinusoidal as shown in Figure 4-3(d-f) and a beating behavior is observed. This shows that the flow is now periodic over the beating period which is related to the forced oscillation period by  $T_b = 15T_e$ . Different paths between two cycles in the phase plane of Figure 4-3(f) are associated with the quasi-periodic state. The presence of more than one peak in the

frequency spectrum exhibits the nonlinear nature of the forced harmonic excitation. The other harmonics of the dominant frequency can interact with a pure harmonic mode to non-synchronized state.

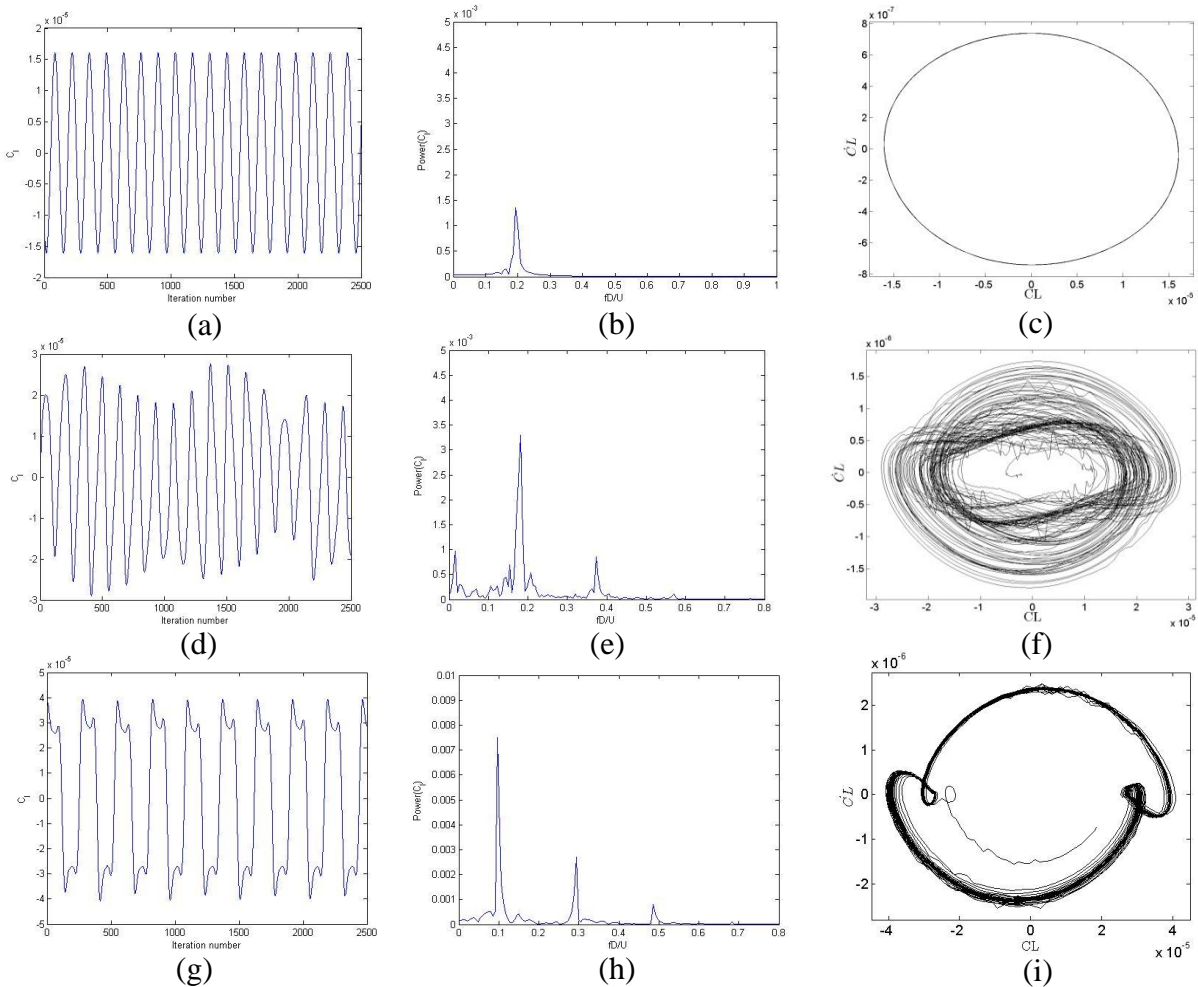


Figure 4-3: Time series, power spectrum and phase plane of the fluctuating lift coefficient at  $Re=200$  for three cases (a-c)  $A/D = 0.0$  (d-f)  $A/D = 0.175$  and  $A/D = 0.5$  with  $f_e/f_s = 1$ .

As the oscillation amplitude is increased, the lift trace varies from quasi-steady form to one with two smaller secondary peaks per oscillation. The power spectrum has a dominant peak at  $fD/U = 0.1$  and a secondary frequency at  $fD/U = 0.2$  verifying the torus-doubling nature of the flow. Although a synchronized vortex shedding mode is observed, a complete lock-on is not observed due to the presence of the other peaks. The secondary frequency is higher than the main one and thus does not affect the periodicity but deforms the shape of each cycle. Therefore, the phase-plane diagram exhibits a limit cycle indicating that the wake locks onto the forced oscillatory motion with different shapes from the stationary cylinder limit cycle.



POD is used to identify the most energetic modes with their corresponding spatial structures. The temporal evolution of the POD primary modes with their temporal distributions for 2D and spatial structures with their temporal modes for 3D simulations of a stationary cylinder case are presented in Figure 4-4(a-d) and Figure 4-5(a-i) in terms of the  $v$ -velocity streamlines. The 2D POD modes are derived as a set of orthonormal fields in a Hilbert system including the frequency information.

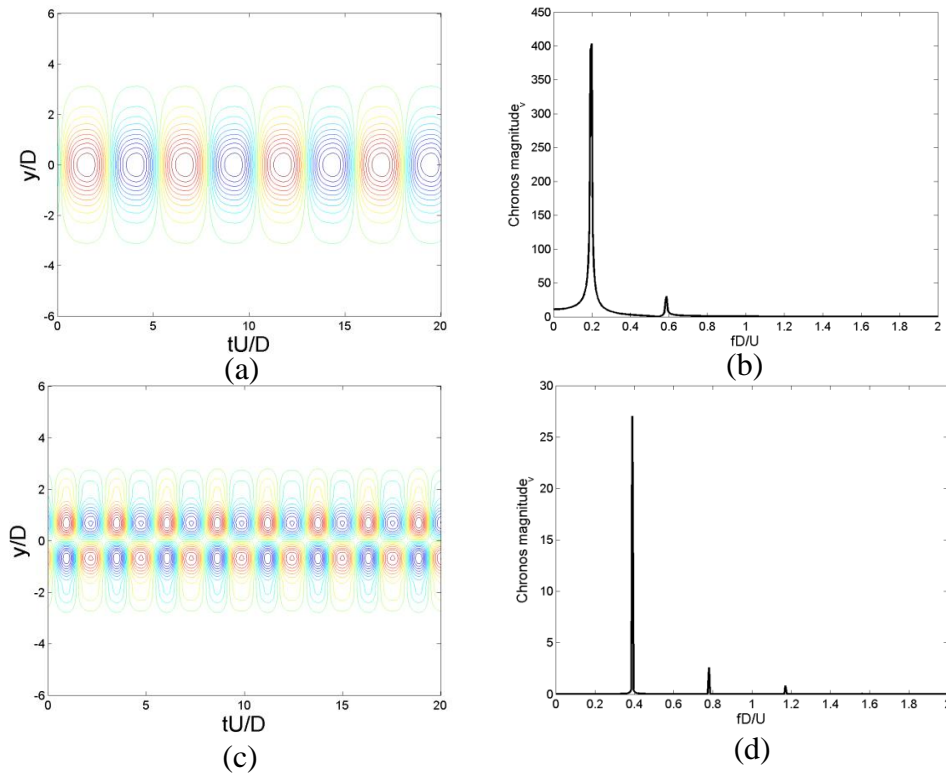


Figure 4-4: Spatio-temporal structure of the 2D POD modes in terms of the  $v$ -velocity streamlines with their corresponding *chronos* values for stationary cylinder case, (a,b) first mode, (c,d) second mode.

The *chronos* of the first mode for the fixed cylinder case shows a single peak at  $fD/U = 0.2$  and smaller peak at third harmonic  $fD/U = 0.6$ . The second mode dominant frequency is at  $fD/U = 0.4$  with smaller peak at  $fD/U = 0.8$ . The first primary mode is symmetric whereas the second mode is asymmetric. The 3D POD modes can be grouped as pairs where the two modes of each pair have similar energy. The first two eigenmodes of 3D POD correspond to the first mode of 2D POD mode with *chronos* at  $fD/U = 0.2$ . Their grouping shows that the wake behaves like a travelling wave. The second pair of dominant modes has a similar symmetry to the first primary modes but

with the frequency at  $fD/U = 0.6$  which is associated with the secondary peak of the 2D POD main mode.

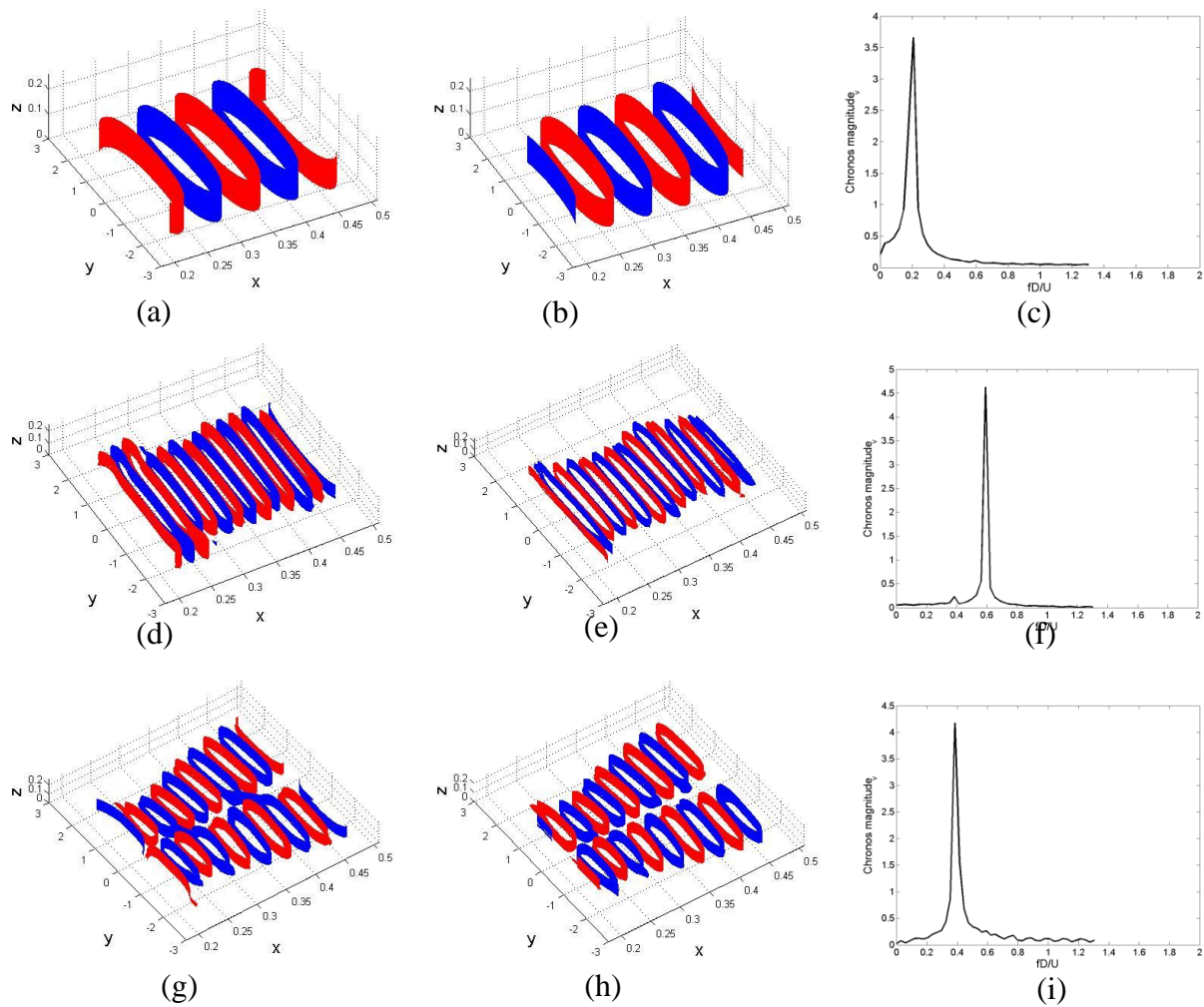


Figure 4-5: Spatial structure of the first three pairs of the 3D POD modes with their corresponding *chronos* values for stationary cylinder case, (a-c) first pair (d-f) second pair and (g-i) third pair.

Eigenmode 5 and 6 are asymmetric with the dominant frequency at  $fD/U = 0.4$  similar to the *chronos* of the second mode in 2D POD analysis. The eigenmodes of order 7 and 8 have the same asymmetric structure as the fifth and sixth modes but as their energy is less than 0.1% they are considered negligible.

Comparing the 3D and 2D singular value spectra given in Figure 4-6(a) and 4-6(b) shows that the modes with similar symmetry have the same energy level. As the 2D  $v$ -velocity signal is

complexified to contain the frequency information, each pair of similar patterns of the 3D POD modes with a phase shift correspond to one mode of the 2D POD mode. The similar structure of the modes shifted spatially is due to the convective nature of the flow. The symmetric and asymmetric primary modes with their singular values decaying pairwise exhibit the symmetry of the wake flow. Most of the fluctuation energy is captured by the first two modes of the 2D POD modes or the first six modes of the 3D POD modes with the remaining eigenvalues accounting for much less than 1% of the energy which provides a satisfactory description of the flow dynamics.

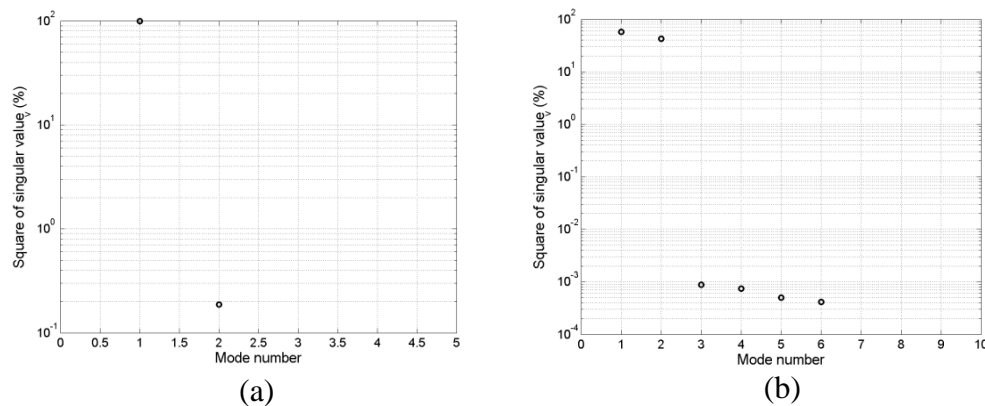


Figure 4-6: Singular values of the transverse velocity deduced for fixed cylinder case, (a) from 2D POD analysis, (b) from 3D POD analysis.

By increasing the oscillation amplitude up to  $A/D=0.175$ , other peaks appear in the *chronos* of both modes. The interaction of these two frequencies leads to non-synchronized flow as shown in Figure 4-7(a-d) of 2D POD results and Figure 4-8(a-i) for 3D POD analysis where the spacing between vortices is different. The *chronos* of the POD modes show that the second mode amplitude increases while the amplitude of the first mode decreases; however the first mode amplitude is still higher than the second one and thus the basic mode remains symmetric as shown in Figure 4-7(a) and 4-8(a-b) for 2D and 3D primary modes respectively. The cylinder motion energizes the second pair of modes. The flow energy is also partially convected downstream due to the spatial effects given in Figure 4-8(d-i) and partially transferred to higher modes via nonlinear interaction between the symmetric and asymmetric pair of modes. The dominant modes also dissipate energy. The fifth and sixth spatial modes shown in Figure 4-8(g-h) might be related to the asymmetric modes only in the very near wake as they are shift modes in the transition region.

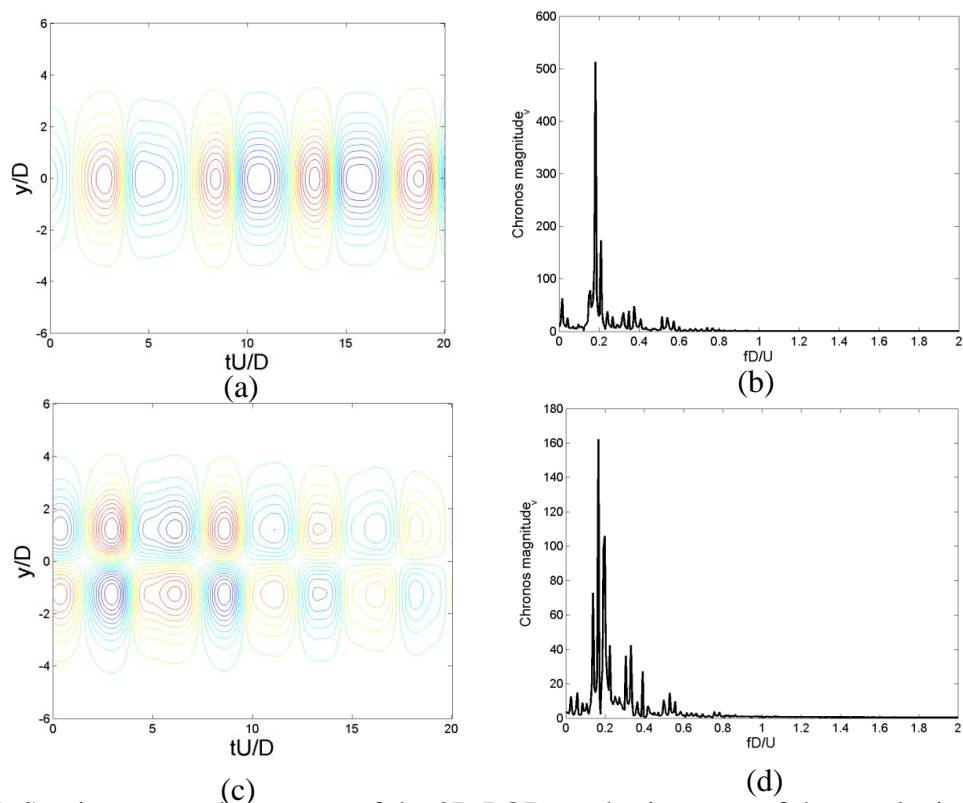
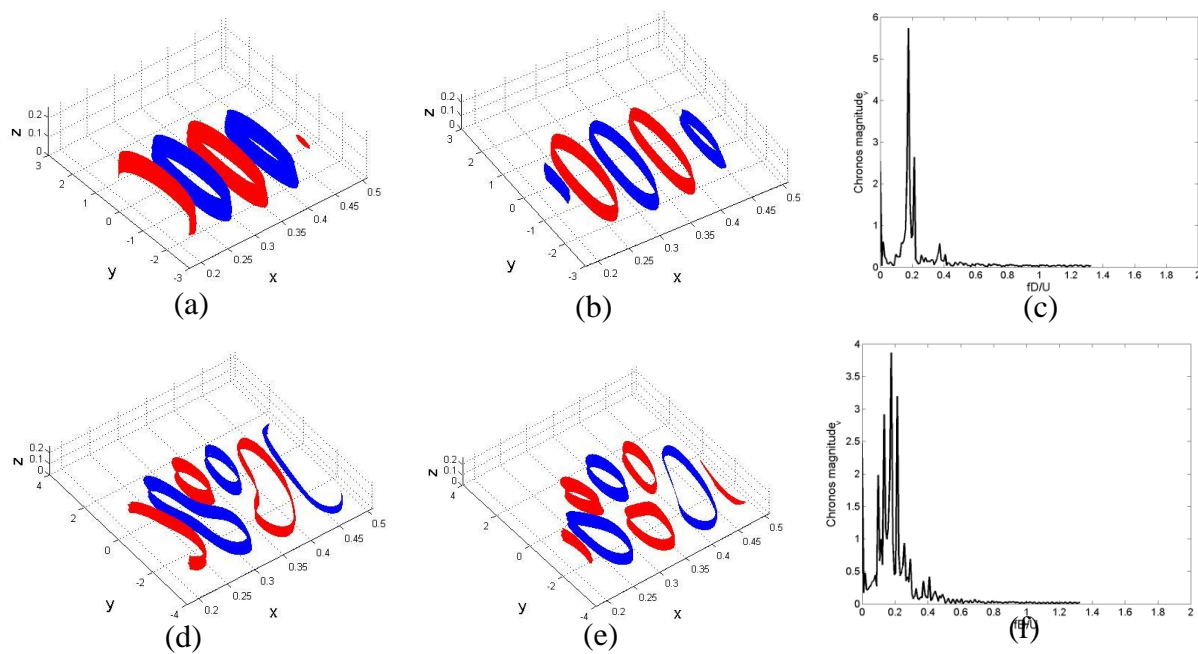


Figure 4-7: Spatio-temporal structure of the 2D POD modes in terms of the  $v$ -velocity streamlines with their corresponding *chronos* values for  $A/D=0.175$ . (a,b) first mode, (c,d) second mode.



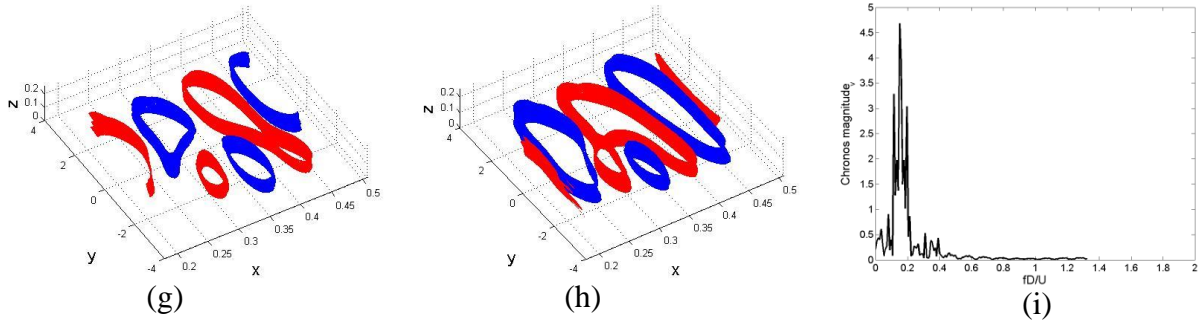


Figure 4-8: Spatial structure of the first three pairs of the 3D POD modes with their corresponding *chronos* values for  $A/D=0.175$ , (a-c) first pair (d-f) second pair and (g-i) third pair.

As the oscillation amplitude increases up to  $A/D=0.5$ , the 3D POD analysis shows that the eigenvalue spectrum of Figure 4-9(b) is again concentrated around the first few modes having the similar structure to those derived for the fixed cylinder case which match with the 2D POD analysis. The 2D eigenvalues given in Figure 4-9(a) confirm that the other modes have less than 1% energy although they are energized due to the cylinder oscillation. The 3D singular value plot also confirms that the first four modes contain more than 99% of the energy.

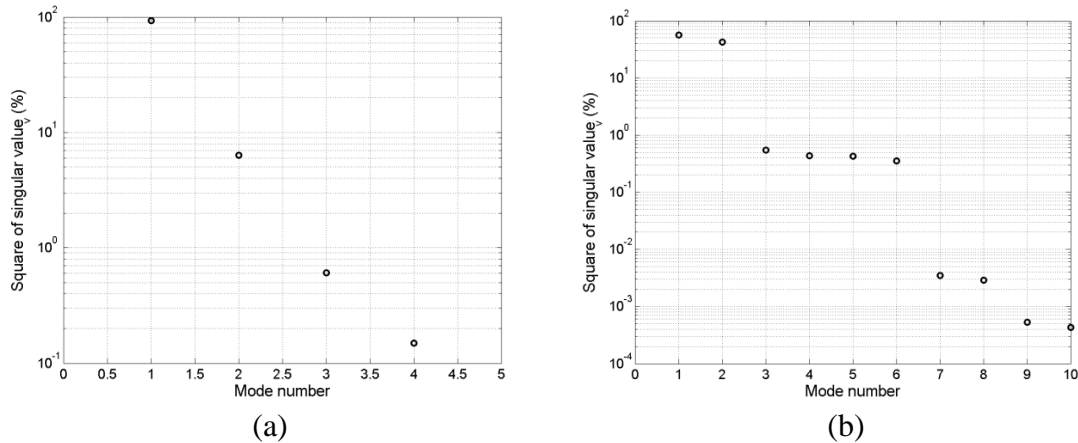


Figure 4-9: (a) Singular values of the transverse velocity deduced for  $A/D=0.5$  (a) from 2D POD analysis, (b) from 3D POD analysis.

The torus-doubling bifurcation is observed in the two 2D POD eigenmodes where the reduced primary vortex shedding frequency is  $fD/U = 0.1$  with a second mode peak at  $fD/U = 0.3$  due to incomplete synchronization. In the 3D POD analysis, the torus bifurcation occurs in the fourth-order eigenmodes followed by a near period doubling at  $fD/U = 0.116$ . It is clear that by increasing the amplitude of oscillation, the space between vortices increases; therefore four vortices are shed

instead of eight for stationary cylinder case shown in Figure 4-10(a) and similarly for 3D POD analysis, four vortices are observed in the fixed cylinder case and two vortices are shed for  $A/D=0.5$  as shown in Figure 4-11(a-b) confirming the first mode lock-on over two cycles of cylinder oscillation in *chronos* of Figure 4-11(c) and *chronos* of the 2D POD mode in Figure 4-10(b). The dominant frequency of the  $v$ -velocity corresponds well with the lift coefficient frequency at various oscillation amplitudes. However, the higher harmonics especially for 3D POD do not match well due to the spatial effects. The spatial structures of the fifth and sixth modes are also rather asymmetric with some random velocity distributions reflecting chaotic pattern downstream.

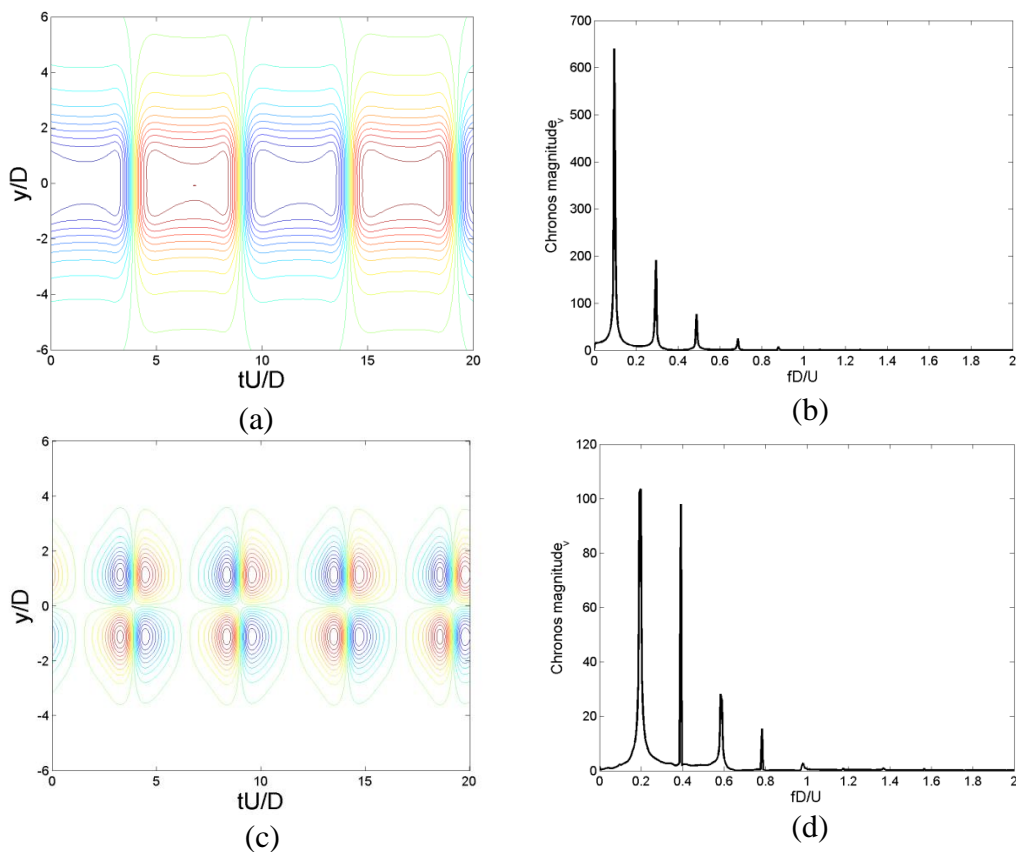


Figure 4-10: Spatio-temporal structure of the 2D POD modes in terms of the  $v$ -velocity streamlines with their corresponding *chronos* values for  $A/D=0.5$ , (a,b) first mode, (c,d) second mode.



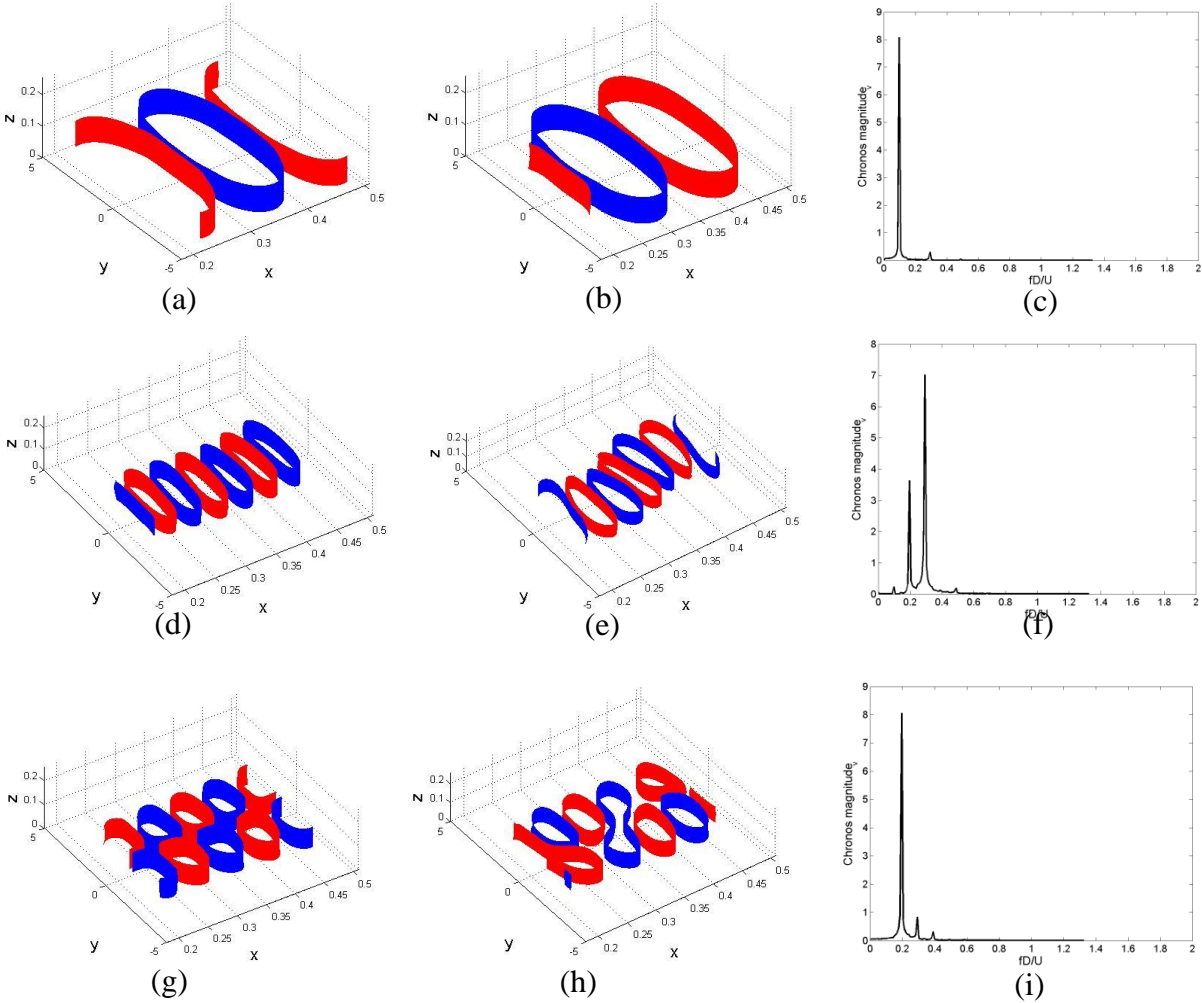


Figure 4-11: Spatial structure of the first three pairs of the 3D POD modes with their corresponding *chronos* values for  $A/D=0.5$ , (a-c) first pair, (d-f) second pair and (g-i) third pair.

The snapshots of the transverse velocity streamlines are plotted for three oscillation amplitudes with harmonic forcing frequency as illustrated in Figures 4-12 and 4-13 for 3D simulations. For the stationary cylinder wake, the  $v$ -velocity field is exactly the same over a shedding period. For  $A/D=0.175$  the vortices shed from the cylinder surface elongate and the distance between them is not equal indicating the flow is not periodic over the shedding cycle but over several cycles corresponding to the beating period. The beating phenomenon can be observed by plotting the  $v$ -velocity streamlines at three instants  $t=t_0, t=t_0+T_e, t=t_0+2T_e$  and  $t=t_0+T_b$  where  $T_b=15T_e$ . The quasi-periodic vortex shedding pattern as shown in Figure 4-12 at two instants separated by  $T_b$  is the same. Changing the oscillation amplitude can cause transition from a quasi-periodic to a phase-locked state as in Figure 4-13.

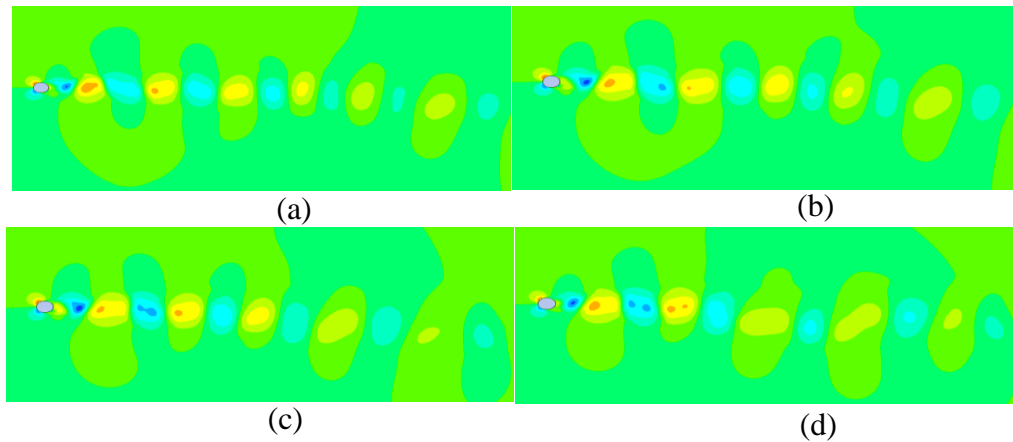


Figure 4-12: The  $v$ -velocity contours for  $A/D=0.175$  with  $f_e/f_s=1$  for (a-d)

$$t = t_0, t = t_0 + T_e, t = t_0 + 2T_e \text{ and } T_b = 15T_e.$$

For  $A/D=0.5$  the  $v$ -velocity field shows a similar vortex shedding pattern to the case of the stationary cylinder with an increase in the longitudinal spacing between the vortices leading to the period of the vortex shedding twice as the period of the base flow. The  $v$ -velocity field visualization in Figure 4-13(b) indicates that the vortex shedding is periodic over two cylinder oscillation periods, which confirms the two-dimensional simulation results. In comparison, the 3D  $v$ -velocity field of the wake is similar to the two-dimensional one with a small amount of spatial effect due to the three dimensional instabilities. This may be due to the fact that the wake flow is effectively two-dimensional and laminar.

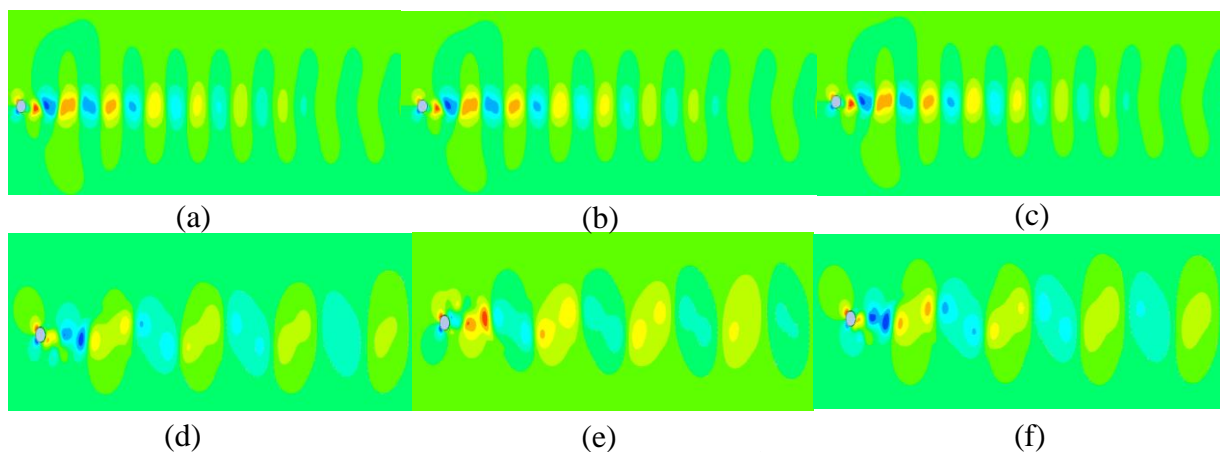


Figure 4-13: (a-c) The transverse velocity contours with  $f_e/f_s=1$  over two oscillation periods for (a-c) stationary cylinder, (d-f)  $A/D=0.5$ .

The transverse velocity field can be reconstructed using the POD dominant modes to show the relation between vortex shedding modes and the  $v$ -velocity field.



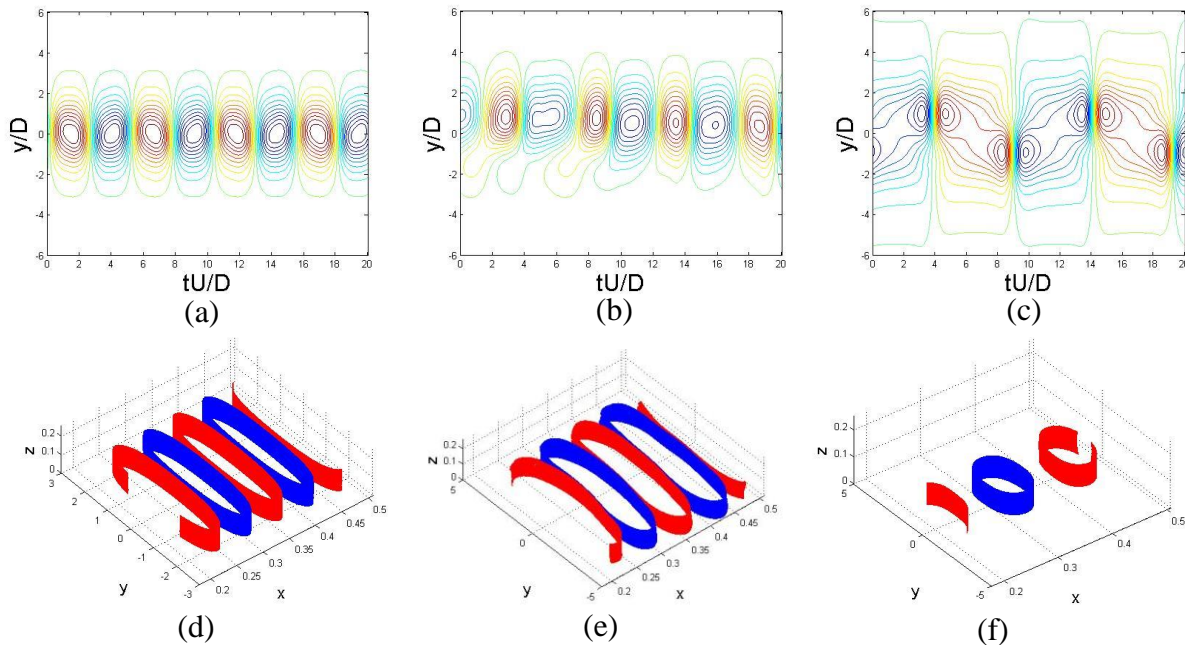


Figure 4-14: Reconstruction of  $v$ -velocity field for oscillation amplitudes  $A/D=0.0$ ,  $A/D=0.175$  and  $A/D=0.5$  (a-c) using two first modes of the 2D POD (d-f) using four eigenmodes of the 3D POD.

The reconstruction is made using the first two POD modes for the 2D case or four POD eigenmodes for the 3D case. As shown in Figure 4-14, the 2S mode for the stationary cylinder case is clearly evident. For  $A/D=0.5$  the reconstructed eigenmodes are associated with the basic 2S wake mode with half shedding frequency which are similar observation of the transverse velocity contours given in Figure 4-13 from numerical computation.

#### 4.4 Conclusion

The two and three-dimensional simulations of wake flow past over a circular cylinder forced to harmonic inline oscillation are performed using the immersed boundary condition method. The phase plane, power spectra and time series of the lift coefficient with  $v$ -velocity POD modes are used to analyze the wake dynamics and bifurcations. The wake pattern and torus doubling bifurcation observed in 2D simulation is in good agreement with the 3D results since the 3D features are weak. The main shedding frequency is almost equal to the primary 2D instability without any new time scale introduced from the secondary 3D transition. However, the amplitude of the lift coefficient is lower due to the three-dimensional distortions of the 3D instability. Thus the 3D results show very small variability from the 2D model for forced oscillation cases, despite

the significant differences found in the fixed cylinder case. For the stationary cylinder case, the wake initiates the transition from 2D to 3D flow by the spanwise secondary instability. But the cylinder oscillation inhibits the growth of three-dimensional perturbations as the transverse velocity streamlines are periodic without changing sign and almost independent of  $z$ -direction. This shows that the cylinder motion has a stabilization effect on the wake dynamics and delays the secondary transition to three dimensional. Thus the vortex shedding modes and the stability of the flow with respect to the three-dimensional fluctuations are dependent on the cylinder vibration. It is shown that the wake flow at small oscillation amplitude becomes stable to three-dimensional perturbation. Although 2D simulation is a simplifying assumption compared to three-dimensional approach, the results confirm that the vortex shedding remains two-dimensional.

## GENERAL DISCUSSIONS

The research performed in the present Thesis is motivated by better understanding of the physical mechanism of the vortex induced vibration (VIV). The transition from steady state to spatio-temporal complexity and turbulence in the wake flow can be uncovered by studying the fundamental wake flow over a simple geometry such as a cylinder which leads to the development of fluid-structure interaction. The forced inline excitation is employed to study the wake flow dynamics. The work approach combined the equivariant bifurcation and normal form theories with numerical simulation to uncover the key factors behind the formation of the different wake patterns. The first paper (Chapter 2) includes the two-dimensional numerical computations of the wake flow subjected to inline cylinder oscillation with harmonic forcing frequency for selected oscillation amplitudes. A low order model was also developed to reduce the number of degree-of-freedom in the problem. The eigenfunctions of the  $v$ -velocity were then computed by POD approach using the flow field snapshots from the CFD simulation. The resulting dominant modes were used to model the wake flow characteristics over a wide range of oscillation amplitudes and forcing frequency ratios. Two primary modes are considered invariant under the action of a symmetry group. The vortex shedding primary modes have unique symmetry properties. These symmetries were applied to develop an analytical model using the equivariant bifurcation theory. The wake dynamics was modeled by a set of ODE which provides analytical insight into the physical mechanisms.

From the CFD results, by increasing the amplitude of oscillation, the dominant modes reach a quasi-periodic state in the transition region and by later increase in the forcing amplitude two travelling waves undergo a torus-doubling bifurcation. The cylinder motion energized the asymmetric mode to interact with the first mode leading to the torus doubling bifurcation. However, the bifurcated S mode, which is period doubled, has higher amplitude than the asymmetric mode. This confirms the period-doubled symmetric transverse velocity pattern observed in simulations. The third harmonic of the lift coefficient exists in the response of the wake flow at  $A/D=0.5$  due to the inline motion of the cylinder.

The nonlinear interaction between symmetric and asymmetric modes was qualitatively predicted by the analytical model. The linear bifurcation parameters were changed due to the cylinder motion leading to the symmetry-breaking bifurcation. The mode competition between these two modes has been investigated while they bifurcate simultaneously. In the linear stability analysis the transitions of the primary modes were investigated by movement of the Floquet multipliers in the

Argand diagram. The complex-conjugate pair of Floquet multipliers collides with the negative real axis and crosses the unit circle at -1 confirming the torus doubling bifurcation. In addition, a stability analysis of the coupled amplitude equations was performed in Poincare space where two steady travelling waves undergo the torus doubling bifurcation. The bifurcated modes have the same spatial symmetries as in fixed cylinder case but with different wavenumbers. The symmetries and wavelength of each mode could therefore be determined characterizing the bifurcated pattern. Thus, the symmetry-based model correctly predicts the bifurcation sequences that were observed in CFD results.

Employing the same methodology in the second paper presented in Chapter 3, the forced super non-harmonic and superharmonic streamwise excitation simulations were performed. Various vortex shedding patterns were observed for different forcing frequency ratios and oscillation amplitudes within the identification of the lock-on region using phase plane and power spectra of the lift coefficient. For the harmonic excitation case, the basic flow undergoes a Hopf bifurcation at  $A/D=0.175$  and since the second frequency is lower than the main one, the beating phenomenon was observed. At  $A/D=0.5$  the transition from the quasi-periodic state to the lock-on state occurs where the dominant mode keeps the spatial symmetry of the base flow with half shedding frequency. For forcing frequency ratio  $f_e / f_s = 1.5$ , the lock-on region becomes wider than the harmonic excitation case and covers  $A/D=0.175$ . The competition between symmetric and antisymmetric primary modes leads to the breaking of the reflection symmetry and the P+S mode bifurcates from the mode interaction. For the superharmonic excitation case with  $f_e / f_s = 2$ , the symmetric S mode replaces the asymmetric basic mode 2S while the  $v$ -velocity mode switches from symmetric to asymmetric. Lock-on also occurs within the oscillation amplitude range of [0.05-0.5]. The bifurcation analysis of the analytical model correctly predicts the symmetry of the primary modes, the dominant mode wavelength and bifurcation sequences. However, the frequency of the second mode does not match for the superharmonic case. In this case, more than two bifurcation parameters are involved which shows the complexity of the mode interaction. Furthermore, the change in the vortex shedding pattern is found to cause a significant effect on the force acting on the cylinder as the lift coefficient magnitude is reduced in the symmetric pattern. Finally, the secondary instability of the wake flow was considered in the third paper presented in Chapter 4. The three-dimensional simulations of the wake flow at  $Re=200$  using the SST model were performed to investigate the cylinder motion effect on the vortex shedding. The three-

dimensional simulations show that the wake flow dynamics remains almost two-dimensional at  $Re=200$ . It was shown that the vibration of the cylinder improves the spanwise correlation of the vortices and suppresses the three-dimensional instabilities, although there are some spatial effects which lead to the random distribution of vorticity downstream. This suggests that the cylinder motion has a stabilizing effect in the flow and the two-dimensional simulations provide good results, thus the wake flow can be assumed two-dimensional.

## CONCLUSIONS AND RECOMMENDATIONS FOR FUTURE WORK

As mentioned above, the research is motivated by fluid-structure interaction results from VIV. The objective of this work is to investigate the pure inline VIV effect to improve the prediction methods of wake flow dynamics. Forced oscillation of a rigid cylinder for selected oscillation amplitudes and forcing frequency ratio were carried out to study the wake response to the prescribed motion. The following paragraphs outline main contributions of this Thesis and recommendations for future work are presented. The main contributions of the Thesis are:

1. Development of the modal amplitude equations, with the role of normal form symmetries through equivariant bifurcation theory, capable of predicting the forced inline cylinder wake dynamics.
2. Bifurcation and stability analysis of the coupled amplitude equations to predict the bifurcation sequences that observed in CFD results.

The first two primary modes which exist for various oscillation amplitudes with harmonic forcing frequency ratio are employed to model the wake dynamics. The symmetries and periodicity of these modes are determined by POD analysis of the  $v$ -velocity data. Each of these modes has its own symmetry properties. The symmetries of the spatial eigenfunctions corresponding to the dominant  $v$ -velocity modes are applied to the governing equations of the system to develop modal amplitude equations through the bifurcation theory. The coefficients of the amplitude equations are calculated through the least squares method using the *chronos* of two primary modes, which are transformed into complex signals by Hilbert transformation. Thus, the frequency saturation information is included as the coefficients are complex. Two linear terms of the amplitude equations are affected most by the variation of the streamwise oscillation and thus considered as the bifurcation parameters. By changing the bifurcation parameters, the low order amplitude equations can have different solution branches with less symmetry than the symmetry of the original equations. The sequence of bifurcations observed in CFD and previous experimental results are well predicted through bifurcation analysis of the symmetry-based model.

3. Identification of the lock-on region and various vortex shedding patterns by simulating the forced inline oscillation of a circular cylinder in the range of frequencies  $f_e / f_s \in [1-2]$  consisting the harmonic and superharmonic excitation region with amplitude ratio belongs to the range  $A / D \in [0-0.5]$ .

4. Bifurcation analysis of the amplitude equations to predict the sequence of bifurcations occurs according to the combination of oscillation amplitudes and forcing frequency ratios.

The wake structure and lock-on phenomenon are numerically investigated in the near wake region for  $Re=200$  with oscillation amplitude extended up to  $0.5D$  and three frequency ratios  $f_e/f_s = 1, 1.5$  and  $2$ . The wake flow with velocity, vorticity contours and lift coefficient transitions at each combination of oscillation amplitudes and forcing frequency ratios are investigated and the lock-on region is determined. The bifurcation scenario is applied to the developed analytical model to study the mode competition between symmetric and asymmetric ones and determine the types of bifurcation and wavenumber selection of the solution branches. The analytical results match well with those obtained numerically.

5. Investigation of the stability of the two-dimensional wakes to three-dimensional perturbations at  $Re=200$  through POD analysis of three-dimensional forced harmonic inline wake flow of a circular cylinder.

The three-dimensional wake flow past a circular cylinder forced to oscillate inline to the free-stream is also investigated to verify the 2D results. The numerical simulations are performed for three selected oscillation amplitudes  $A/D=0.0, 0.175$  and  $0.5$  with frequency equal to natural shedding frequency at  $Re=200$ . The validity of two-dimensional flow field for  $Re=200$  subjected to inline harmonic oscillation is confirmed.

## **Recommendations for future work**

As noted in the conclusions, the dominant frequency of the transverse velocity is a good representative of the vortex shedding frequency except for the superharmonic case for  $A/D=0.5$ . Since there is a nonlinear coupling between the streamwise and transverse velocities, the vorticity component may be a better representative for identification of the shedding frequency since it contains both the  $u$  and  $v$  velocity effects. Although the forced harmonic and superharmonic excitation of the wake flow are investigated, there are number of issues that remain unresolved. The first one is the subharmonic excitation region in which from previous studies it seems that the vortex shedding may deviate from the horizontal axes and thus the flow becomes doubly periodic. For harmonic and superharmonic cases, the vortex shedding is parallel to the  $x$ -axis and thus the one-dimensional oscillatory pattern is used to develop the analytical model although the flow is temporal-doubly periodic. However, if the wake flow is two-dimensionally periodic a dual lattice

should be used to model the wake flow dynamics. Another recommendation for future work is the characterization of the secondary instabilities in the wake flow investigated at higher Reynolds number. At higher Reynolds number three-dimensional effects appear and spanwise effects can change the structure of the wake flow. Using a temporal model is then not sufficient due to the spatial dislocations and the Ginzburg-Landau model should be employed. Experiments can also be performed over a wide range of frequency ratios and oscillation amplitudes in the longitudinal direction making possible to a mapping of the wake modes and a complete Griffin-plot.

## **Publications**

This PhD project has led to three journal articles and one conference paper. The papers submitted to journals are:

NABATIAN N., MUREITHI N. W. (2014), Bifurcation and stability analysis with the role of normal form symmetries on the harmonic streamwise forced oscillation of the cylinder wake, (paper submitted to International Journal of bifurcation and chaos).

NABATIAN N., MUREITHI N. W. (2014), Lock-on vortex shedding patterns and bifurcation analysis of the forced streamwise oscillation of the cylinder wake, (paper submitted to International Journal of bifurcation and chaos).

NABATIAN N., MUREITHI N. W. (2014), POD analysis of three-dimensional forced harmonic inline wake flow of a circular cylinder, (paper submitted to TCSME).



## REFERENCES

- Amdjadi, F., 2002. Hopf bifurcations in problems with  $O(2)$  symmetry: Canonical coordinates transformation. In: Proceedings of Institute of Mathematics of NAS of Ukraine, 65-71
- Atluri, S., Rao, V.K., Dalton, C., 2009. A numerical investigation of the near-wake structure in the variable frequency forced oscillation of a circular cylinder. *Journal of Fluids and Structures* 25, 229- 244.
- Barkley, D., Gomes, M.G.M., Henderson, R.D., 2002. Three-dimensional instability in flow over a backward-facing step. *Journal of Fluid Mechanics* 473, 167-190.
- Barkley, D., Henderson, R.D., 1996. Three-dimensional Floquet stability analysis of the wake of a circular cylinder. *Journal of Fluid Mechanics* 322.
- Barkley, D., Tuckerman, L., Golubitsky, M., 2000. Bifurcation theory for three-dimensional flow in the wake of a circular cylinder. *Physical Review E*. 61, 5247.
- Berger, E., 1967. Suppression of vortex shedding and turbulence behind oscillating cylinders. *Physics of Fluids* 10.
- Berkooz, G., Holmes, P., Lumley, J.L., 1993. The proper orthogonal decomposition in the analysis of turbulent flows. *Annual Review of Fluid Mechanics* 25, 539–575.
- Blackburn, H.M., Henderson, R.D., 1999. A study of two-dimensional flow past an oscillating cylinder. *Journal of Fluid Mechanics* 385, 255-286.
- Blackburn, H.M., Lopez, J.M., Marques, F., 2004a. Three-Dimensional Quasi-Periodic Instabilities of Two-Dimensional Time-periodic Flows. *15th Australasian Fluid Mechanics Conference*. The University of Sydney, Sydney, Australia.
- Blackburn, H.M., Marques, F., Lopez, J.M., 2004b. On three-dimensional instabilities of two-dimensional flows with a spatio-temporal symmetry. *Journal of Fluid Mechanics*.
- Blackburn, H.M., Marques, F., Lopez, J.M., 2004c. Symmetry breaking of two-dimensional time-periodic wakes. *Journal of Fluid Mechanics* 522, 395-411.
- Bloor, M.S., 1964. The transition to turbulence in the wake of circular cylinder. *Journal of Fluid Mechanics* 19, 290–340.

- Borggaard, J., Hay, A., Pelletier, D., 2007. Interval-based reduced-order models for unsteady fluid flow. *International Journal of Numerical Analysis and Modeling* 4, 353-367.
- Brede, M., Eckelmann, H., Rockwell, D., 1996. On the secondary vortices in the cylinder wake. *Physics of Fluids* 8, 2117-2124.
- Bruneau, C.H., Mortazavi, L., 2006. Control of vortex shedding around a pipe section using a porous sheath. *International Journal of Offshore and Polar Engineering* 16, 90-96.
- Buffoni, M., Camarri, S., Iollo, A., Salvetti, M.V., 2006. Low-dimensional modelling of a confined three-dimensional wake flow. *Journal of Fluid Mechanics* 569, 141-150.
- Cao, Q., Xu, L., Djidjeli, K., Price, W.G., Twizell, E.H., 2001. Analysis of period-doubling and chaos of a non-symmetric oscillator with piecewise-linearity. *Chaos Solitons & Fractals* 12, 1917-1927.
- Carberry, J., Govardhan, R., Sheridan, J., Rockwell, D., Williamson, C.H.K., 2004. Wake states and response branches of forced and freely oscillating cylinders. *European Journal of Mechanics B-Fluids* 23, 89-97.
- Carmo, B.S., 2009. *On Wake Interface in the Flow around Two Circular Cylinders: Direct Stability Analysis and Flow-Induced Vibrations*. London, Imperial College London.
- Chatterjee, A., 2000. An introduction to the proper orthogonal decomposition. *Current Science* 78, 808-817.
- Chen, K.K., Tu, J.H., Rowley, C.W., 2012. Variation of Dynamic Mode Decomposition: Boundary Condition, Koopman and Fourier Analyses. *Journal of Nonlinear Science*.
- Clune, T., Knobloch, E., 1993. Pattern Selection in Rotating Convection with Experimental Boundary-Conditions. *Physical Review E* 47, 2536-2550.
- Constantinides, Y., Oakley, O.H., 2006. Numerical prediction of bare and straked cylinder VIV. *Proceedings of the 25th International Conference on Offshore Mechanics and Arctic Engineering*, Vol 4, 745-753.
- Dawes, J.H.P., 2000. Pattern selection in oscillatory rotating convection. *Physica D* 147, 336-351.

- Dawes, J.H.P., 2001. A Hopf/steady-state mode interaction in rotating convection: bursts and heteroclinic cycles in a square periodic domain. *Physica D* 149, 197-209.
- Dawes, J.H.P., Proctor, M.R.E., 2008. Secondary Turning-type instabilities due to strong spatial resonance. In: *Proceedings of the Royal Society*, 923-942
- Deane, A.E., Mavriplis, C., 1994. Low-dimensional description of the dynamics in separated flow past thick airfoils. *AIAA Journal* 32, 1222-1227.
- Ding, W.C., Xie, J.H., Sun, Q.G., 2003. Interaction of Hopf and period doubling bifurcations of a vibro-impact system. *Journal of Sound and Vibration* 275, 27-45.
- Do, T., Chen, L., Forrest, J.A., Tu, J.Y., 2011. Numerical Experiments of Forced Cylinder Oscillations at an Angle to Oncoming Flow. *Engineering Applications of Computational Fluid Mechanics* 5, 579-594.
- Druault, P., Chaillou, C., 2007. Use of Proper Orthogonal Decomposition for reconstructing the 3D in-cylinder mean-flow field from PIV data. *Comptes Rendus Mecanique* 335, 42-47.
- Ermentrout, G.B., Folias, S.E., Kilpatrick, Z.P., 2012. Spatiotemporal pattern formation in neural fields with linear adaptation. *Neural Field Theory*, Springer.
- Gioria, R.S., Meneghini, J.R., 2010. Amplitude threshold in the wake transition of an oscillating circular cylinder. *Seventh Iutam Symposium on Laminar-Turbulent Transition* 18, 497-500.
- Goldstein, H.F., Knobloch, E., Silber, M., 1992. Planform Selection in Rotating Convection - Hexagonal Symmetry. *Physical Review A* 46, 4755-4761.
- Graham, W.R., Peraire, J., Tang, K.Y., 1999. Optimal control of vortex shedding using low-order models. Part I - Open-loop model development. *International Journal for Numerical Methods in Engineering* 44, 945-972.
- Griffin, O.M., Ramberg, S.E., 1974. The vortex-street wakes of vibrating cylinders. *Journal of Fluid Mechanics* 66, 533-576.
- Griffin, O.M., Ramberg, S.E., 1976. Vortex shedding from a cylinder vibrating inline with incident uniform flow. *Journal of Fluid Mechanics* 75, 257-271.

- Gunaratne, G.H., Ouyang, Q., Swinney, H.L., 1994. Pattern-Formation in the Presence of Symmetries. *Physical Review E* 50, 2802-2820.
- Holmes, P., Lumley, J.L., Berkooz, G., 1996. *Turbulence, coherent structures, dynamical systems and symmetry*, Cambridge University Press, Cambridge.
- Hoyle, R., 2006. *Pattern formation An Introduction to Methods* Cambridge Univ. Press Cambridge.
- Kaiktsis, L., Papadopoulos, C.I., Triantafyllou, G.S., POD Analysis of Ordered and Disordered Vortex Wakes in Flow past an Oscillating Cylinder. *ENOC 2011 7th EUROPEAN NONLINEAR DYNAMICS CONFERENCE*. Rome, Italy.
- Kerschen, G., Golinval, J.C., Vakakis, A.F., Bergman, L.A., 2005. The method of proper orthogonal decomposition for dynamical characterization and order reduction of mechanical systems: An overview. *Nonlinear Dynamics* 41, 147-169.
- Konstantinidis, E., Balabani, S., Yianneskis, M., 2007. Bimodal vortex shedding in a perturbed cylinder wake. *Physics of Fluids* 19.
- Konstantinidis, E., Bouris, D., 2009. Effect of nonharmonic forcing on bluff-body vortex dynamics. *Physical Review E* 79.
- Koopman, G., 1967. The vortex wakes of vibrating cylinders at low Reynolds numbers. *Journal of Fluid Mechanics* 28, 501-512.
- Lam, K.M., Liu, P., Hu, J.C., 2010. Combined action of transverse oscillations and uniform cross-flow on vortex formation and pattern of a circular cylinder. *Journal of Fluids and Structures* 26, 703-721.
- Le Gal, P., Nadim, A., Thompson, M., 2001. Hysteresis in the forced Stuart-Landau equation: Application to vortex shedding from an oscillating cylinder. *Journal of Fluids and Structures* 15, 445-457.
- Lentini, J.S., Thompson, M.C., Hourigan, K., 2006. Three-dimensional transition in the wake of a transversely oscillating cylinder. *Journal of Fluid Mechanics* 577, 79-104.
- Leweke, T., Williamson, C.H.K., 1998. Three-dimensional instabilities in wake transition. *European Journal of Mechanics B-Fluids* 17, 571-586.

- Li, T.A., Zhang, J.Y., Zhang, W.H., 2011. Nonlinear characteristics of vortex-induced vibration at low Reynolds number. *Communications in Nonlinear Science and Numerical Simulation* 16, 2753-2771.
- Mittal, S., Kumar, V., 1999. Finite element study of vortex-induced cross-flow and in-line oscillation of a circular cylinder at low Reynolds numbers. *International Journal for Numerical Methods in Fluids* 31, 1087-1120.
- Morse, T.L., Williamson, C.H.K., 2006. Employing controlled vibrations to predict fluid forced on a cylinder undergoing vortex-induced vibration. *Journal of Fluids and Structures* 22, 877-884.
- Morse, T.L., Williamson, C.H.K., 2009. Prediction of vortex-induced vibration response by employing controlled motion. *Journal of Fluid Mechanics* 634, 5-39.
- Mureithi, N.W., 2003. Implications of symmetry in inline and Karman shedding mode interaction. *NAGARE Journal of the Japanese Society of Fluid Mechanics* 22, 211-227.
- Mureithi, N.W., Huynh, K., Rodriguez, M., Pham, A., 2010. A simple low order model of the forced Karman wake. *International Journal of Mechanical Sciences* 52, 1522-1534.
- Mureithi, N.W., Rodriguez, M., 2005. Stability and bifurcation analysis of a forced cylinder wake. *Proceedings of the ASME Fluids Engineering Division* 261, 59-66.
- Noack, B., Eckelman, H., 1994. A low-dimensional Galerkin method for the three-dimensional flow around a circular cylinder. *Physics of Fluids* 6, 124-143.
- Noack, B.R., Afanasiev, K., Morzynski, M., Tadmor, G., Thiele, F., 2003. A hierarchy of low-dimensional models for the transient and post-transient cylinder wake. *Journal of Fluid Mechanics* 497, 335-363.
- Ongoren, A., Rockwell, D., 1988. Flow structure from an oscillating cylinder. Part 2: mode competition in the near wake. *Journal of Fluid Mechanics* 191, 225-245.
- Papaioannou, G.V., Yue, D.K.P., Triantafyllou, M.S., Karniadakis, G.E., 2006. Evidence of holes in the Arnold tongues of flow past two oscillating cylinders. *Physical Review Letters* 96.
- Park, D.S., Ladd, D.M., Hendricks, E.W., 1994. Feedback control of von-Karman vortex shedding behind a circular cylinder at low Reynolds numbers. *Physics of Fluids* 6.

- Pham, A.H., Lee, C.Y., Seo, J.H., Chun, H.H., Kim, H.J., Yoon, H.S., Kim, J.H., Park, D.W., Park, I.R., 2010. Laminar Flow Past an Oscillating Circular Cylinder in Cross Flow. *Journal of Marine Science and Technology-Taiwan* 18, 361-368.
- Porter, J., Knobloch, E., 2000. Complex dynamics in the 1 : 3 spatial resonance. *Physica D* 143, 138-168.
- Porter, J., Knobloch, E., 2001. New type of complex dynamics in the 1 : 2 spatial resonance. *Physica D* 159, 125-154.
- Provansal, M., Mathis, C., Boyer, L., 1987a. Benard-von Karman instability: transient and forced regimes. *Journal of Fluid Mechanics* 182, 1-22.
- Provansal, M., Mathis, C., L., B., 1987b. Benard-von Karman instability: transient and forced regimes. *Journal of Fluid Mechanics* 182, 1-22.
- Roshko, A., 1961. Experiments on the flow past a circular cylinder at very high Reynolds number. *Journal of Fluid Mechanics* 10, 345-356.
- Rowley, C.W., 2005. Model reduction for fluids, using balanced proper orthogonal decomposition. *International Journal of Bifurcation and Chaos* 15, 997-1013.
- Rucklidge, A.M., 1997. Symmetry-breaking instabilities of convection in squares. *Proceedings of the Royal Society a-Mathematical Physical and Engineering Sciences* 453, 107-118.
- Ryan, K., Thompson, M.C., Hourigan, K., 2005. Three-dimensional transition in the wake of bluff elongated cylinders. *Journal of Fluid Mechanics* 538, 1-29.
- Schewe, G., 1983. On the force fluctuations acting on a circular cylinder in crossflow from subcritical up to transcritical Reynolds numbers. *Journal of Fluid Mechanics* 133, 265-285.
- Sheard, G.J., Thompson, M.C., Hourigan, K., 2003. A coupled Landau model describing the Strouhal-Reynolds number profile of a three-dimensional circular cylinder wake. *Physics of Fluids* 15, L68-L71.
- Silber, M., Skeldon, A.C., 1999. Parametrically excited surface waves: Two-frequency forcing, normal form symmetries, and pattern selection. *Physical Review E* 59, 5446-5456.

- Sirovichi, L., Kirby, M., 1987. Low-dimensional procedure for the characterization of human Faces. *Journal of the optical society of america* 4, 519.
- Sohankar, A., 2007. Hopf bifurcation, vortex shedding and near wake study of a heated cylinder in cross flow. *Iranian Journal of Science and Technology* 31, 31-47.
- Srikanth, T., Dixit, H.N., Tatavarti, R., Govindarajan, R., 2011. Vortex shedding patterns, their competition, and chaos in flow past inline oscillating rectangular cylinders. *Physics of Fluids* 23.
- Sumer, B., Fredsøe, J., 2006. *Hydrodynamics around cylindrical structures*. New Jersey, World Scientific Publishing Co.
- Thompson, M.C., Leweke, T., Williamson, C.H.K., 2001. The physical mechanism of transition in bluff body wakes. *Journal of Fluids and Structures* 15, 607-616.
- Williamson, C.H.K., 1996. Vortex dynamics in the cylinder wake. *Annual Review of Fluid Mechanics* 28, 477-539.
- Williamson, C.H.K., Govardhan, R., 2008. A brief review of recent results in vortex-induced vibrations. *Journal of Wind Engineering and Industrial Aerodynamics* 96, 713-735.
- Williamson, C.H.K., Roshko, A., 1988. Vortex formation in the wake of an oscillating cylinder. *Journal of Fluids and Structures* 2, 355-381.
- Wooden, S.M., Sinha, S.C., 2007. Analysis of periodic-quasiperiodic nonlinear systems via Lyapunov-Floquet transformation and normal forms. *Nonlinear Dynamics* 47, 263-273.
- Xu, S.J., Zhou, Y., Wang, M.H., 2006. A symmetric binary-vortex street behind a longitudinally oscillating cylinder. *Journal of Fluid Mechanics* 556, 27-43.
- Zheng, Z.C., Zhang, N., 2008. Frequency effects on lift and drag for flow past an oscillating cylinder. *Journal of Fluids and Structures* 24, 382-399.

## APPENDIX A – MATHEMATICAL FORMULATION OF POD

In order to model and control the vortex shedding, numerical computations of forced oscillation are needed. Due to the inherent nonlinearity in the Navier-Stokes equations and complexity of infinite-dimensional flow dynamics, the full simulation is a challenging task. So, some type of approximation is introduced to simplify the flow computation via reduced order model. Many reduced-order model techniques in fluid mechanics are derived from the proper orthogonal decomposition (POD)-Galerkin projection approach. The POD provides a tool to formulate an optimal basis or minimum degree of modes (or freedom) required to represent the system dynamics. This method is known as Karhunen-Loeve expansion in component analysis. It has been applied to many engineering and scientific applications including low-dimensional dynamics modeling (Berkooz et al., 1993; Deane and Mavriplis, 1994; Noack et al., 2003); image processing (Holmes et al., 1996), and pattern recognition (Sirovichi and Kirby, 1987). POD has been widely used to identify the coherent structures in turbulent flows and examine their stability (Holmes et al., 1996) .

The flow field data  $(u,v)$  is generated from a numerical simulation and is assembled in a matrix  $W_{S \times 2N}$  as shown below. The fluctuating velocity matrix is calculated by subtracting the mean velocities from the individual snapshot. Each row represents a time instant or a snapshot and  $S$  is the total number of snapshots for  $N$  grid points in the domain. The eigenvalues represent the measure of kinetic energy of each mode.

$$W = \begin{bmatrix} u_1^{(1)} & \cdots & u_N^{(1)} & v_1^{(1)} & \cdots & v_N^{(1)} \\ u_1^{(2)} & \cdots & u_N^{(2)} & v_1^{(2)} & \cdots & v_N^{(2)} \\ \vdots & & \vdots & \vdots & & \vdots \\ u_1^{(S)} & \cdots & u_N^{(S)} & v_1^{(S)} & \cdots & v_N^{(S)} \end{bmatrix} \quad (\text{A-1})$$

Mathematically, the eigenfunction  $\Phi$  is computed in a way that the following relation becomes maximum

$$\frac{\langle |u, \Phi|^2 \rangle}{\|\Phi^2\|}, \quad (\text{A-2})$$

where  $\langle \cdot \rangle$  denotes the average operator in time. This equation is equivalent to a Fredholm integral eigenvalue represented as



$$\int_{\Omega} R_{ij}(x, x') \Phi^j(x') dx = \lambda \Phi^i(x), \quad (\text{A-3})$$

where  $i, j$  are the number of velocity components and  $R(x, x')$  is the space-time correlation tensor and the eigenfunctions are the POD modes. The average operator is evaluated in time. In this approach, the autocovariance matrix is computed as

$$R = W^T W \quad (\text{A-4})$$

The POD modes are then calculated by solving the eigenvalue problem

$$R Q^i = \lambda^i Q^i \quad (\text{A-5})$$

where  $\lambda^i$  and  $Q^i$  are the eigenvalue and eigenvector. The POD modes are computed as follows

$$\Phi_i = \frac{1}{\sqrt{\lambda_i}} W Q_i \quad (\text{A-6})$$

The velocity eigenmodes have relation as  $\Phi_i \cdot \Phi_j = \delta_{ij}$  where  $\delta_{ij}$  is the kronecker delta function which shows the orthogonally characteristic of these modes. The optimality is determined by capturing the greatest possible fraction of the eigenvalues for a projection set of modes. In another approach, the singular value decomposition (SVD) of the data is computed. The POD eigenfunctions of the data ensemble,  $W = U \Sigma V^T$  are computed via three methods

1.  $W W^T \in \mathbb{R}^{S \times S} : W^T W V_i = \sigma_i^2 V_i \text{ and } U_i = \frac{1}{\sigma_i} W V_i \text{ (if } S \square N \text{)}$
2.  $W W^T \in \mathbb{R}^{N \times N} : W W^T U_i = \sigma_i^2 U_i \text{ (if } S \square N \text{)}$
3.  $W \in \mathbb{R}^{S \times N} : W^T U_i = \sigma_i V_i$

where  $\Sigma$  contains the singular values of  $W$ . The descending order of the singular values in  $\Sigma$  are positive and real. The  $\sigma_i$  is related to the eigenvalue  $\lambda_i$  by  $\lambda_i = \sigma_i^2$ . The eigenvalue represent the energy contained in each eigenfunction.

### **Galerkin projection**

Then, the reduced order model can be formed using Galerkin projection onto this subspace. The dynamics of the system can be described by

$$\dot{x}(t) = f(x(t)) \quad (\text{A-7})$$

Galerkin projection simply projects the original vector field onto the  $r$ -dimensional subspace through  $\dot{x}_r(t) = P_r f(x_r(t))$ . Writing

$$x_r(t) = \sum_{j=1}^r a_j(t) \varphi_j, \quad (\text{A-8})$$

Substituting into the equation (A-7) and multiplying by  $\varphi_j^T$  leads to a set of  $r$  ODEs that describe the evolution of  $x_r(t)$ .

$$\dot{a}_k(t) = \varphi_k^T f(x_r), \quad k = 1, \dots, r \quad (\text{A-9})$$

### Stuart-Landau equation

In this work, instead of using Galerkin projection, the reduced order model of the transverse velocity field was developed within the framework of the Landau equation using symmetry-equivariant bifurcation theory. The Landau model was first applied in hydrodynamics to perform the stability analysis of a steady flow. A velocity perturbation  $u_1(x, y, z, t)$  of the steady flow  $u_0(x, y, z)$  of the Navier-Stokes equations is expanded as a sum:

$$u_1(x, y, z, t) = \sum_{i=1} \left\{ A_i(t) g_i(x, y, z) + A_i^*(t) g_i^*(x, y, z) \right\}, \quad (\text{A-10})$$

where  $g_i(x, y, z)$  satisfies the boundary condition and the temporal amplitude  $A_i(t)$  satisfies the evolution equation

$$\frac{dA_i}{dt} = s_i A_i + G_i(A_j); j = 1, 2, \dots \quad (\text{A-11})$$

where  $G_i$  includes the nonlinear terms of the mode interaction results from the nonlinear partial differential equation. The Landau equation is then truncated form of the above equation. The independent mode  $A \propto e^{\sigma t}$  with relative growth rate  $\sigma = \sigma_r + i\sigma_i$  is considered for temporal amplitude term. When  $\text{Re} < \text{Re}_{cr}$  all disturbances are stable and  $\sigma_r < 0$  while for  $\text{Re} = \text{Re}_{cr}$  there is only one normal mode with  $\sigma_1 = \sigma_{r1} + i\sigma_{i1}$  ( $\sigma_{r1} = 0$  for marginal stability at  $\text{Re} = \text{Re}_{cr}$ ). As  $\text{Re}$  increases above  $\text{Re}_{cr}$ ,  $\sigma_{r1} > 0$  but  $\sigma_r < 0$  for all the other modes. Thus, the expression for the amplitude is no longer valid as the modulus does not grow infinitely. The Landau hypothesis leads

to definition of the term which bounds its limit. The following term is the first term of the expansion of the solution in powers of  $A$  and  $A^*$ .

$$\frac{d|A(t)|^2}{dt} = 2\sigma_r |A(t)|^2. \quad (\text{A-12})$$

The second term is of the third order in  $A$ . There are two constraints for the validity of the amplitude equation. First the average value of  $\frac{d|A(t)|^2}{dt}$  should be considered on time  $\tau$  long compared to the period  $T = 2\pi/\sigma_i$  meanwhile small enough to keep  $u_1$  as small perturbation. The boundary condition should also be satisfied. Due to the solvability condition, the mean value of the third-order term is almost null, so the second term is of fourth order:

$$\begin{aligned} \frac{d|A(t)|^2}{dt} &= 2\sigma_r |A(t)|^2 - l_r |A(t)|^4, \\ \frac{d|A(t)|}{dt} &= \sigma_r |A(t)| - \frac{1}{2} l_r |A(t)|^3, \end{aligned} \quad (\text{A-13})$$

which is proposed by Landau in 1944. The steady solution for the amplitude is then  $|A| = (2\sigma_r/l_r)^{\frac{1}{2}}$ , where  $\sigma_r$  plays the role of bifurcation parameter with the following relation

$$\sigma_r = k(\text{Re} - \text{Re}_{cr}) + O(\text{Re} - \text{Re}_{cr})^2, \quad (\text{A-14})$$

where  $k$  is the characteristic frequency. Substituting Eq. (A-14) in the steady amplitude relation leads to

$$|A| \propto (\text{Re} - \text{Re}_{cr})^{\frac{1}{2}}. \quad (\text{A-15})$$

The stability analysis of a given flow by Landau equation was derived by Stuart in 1958 (Provansal et al., 1987a). The Stuart-Landau equation governing the weakly nonlinear dynamics of the amplitude of perturbations near the bifurcation is then given:

$$\begin{aligned} \frac{d|A(t)|}{dt} &= \sigma_r |A(t)| - \frac{1}{2} l_r |A(t)|^3, \\ \frac{d\varphi}{dt} &= \sigma_i - \frac{1}{2} l_i |A(t)|^2 \end{aligned} \quad (\text{A-16})$$

As mentioned above in the present work, the nonlinear mode interaction of  $v$ -velocity field have been investigated within the framework of the Landau equation using equivariant bifurcation theory by defining the invariant and equivariant functions described in Appendix C.

## APPENDIX B – INTRODUCTION TO BIFURCATION AND LINEAR STABILITY ANALYSIS

Bifurcation occurs only when the system is structurally unstable. The stability of system is studied by analyzing the fixed point stability. The equilibrium point of the system is called fixed point. Fixed points in the phase space are calculated by solving the equation  $\dot{x} = F(x) = 0$ . The stability of the fixed point is studied by applying a small perturbation to the system located at the considered fixed point

$$\tilde{x} \rightarrow \tilde{x} + \xi \Rightarrow \dot{\tilde{x}} + \dot{\xi} = F(\tilde{x} + \xi) \quad (\text{B-1})$$

Using the approximate polynomial  $F(\tilde{x} + \xi) = F(\tilde{x}) + J(\tilde{x})\xi + O(\xi^2)$ , where  $J(\tilde{x})$  is the Jacobian matrix of  $F$ , the system evolution  $\dot{\xi}$  arises from the perturbation can be obtained from the variational equation

$$\dot{\xi} = J(\tilde{x})\xi + O(\xi^2) \quad (\text{B-2})$$

The eigenvalues  $\lambda_i$  of the Jacobian matrix is found by solving  $J(\tilde{x})\xi_i = \lambda_i\xi_i$ . Writing the variational equation in the form of  $\dot{\xi}_i = \lambda_i\xi_i$  leads to the integration

$$\dot{\xi}_i(t) = \xi_{i0}e^{\lambda_i t} \quad (\text{B-3})$$

Depending on the sign of the real part of the eigenvalues of Jacobian matrix  $\lambda_i$ , the perturbation  $\xi_i$  will be amplified or damped describing the stability of such equilibria.

The first order differential equation can be a function of control parameter as

$$\dot{x} = f(x, \mu) \quad (\text{B-4})$$

where  $\mu$  is the bifurcation parameter. A bifurcation marks qualitative changes of a system when the parameter  $\mu$  is varied. As the system undergoes the bifurcation it can reach to the new equilibrium, periodic or chaotic state. Different types of singular points are presented in Figure B-1.

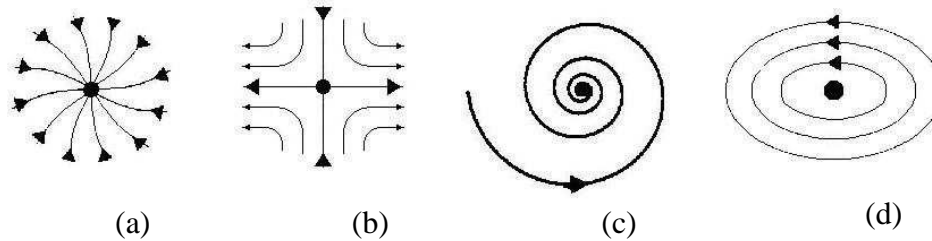


Figure B-1: Different types of the fixed point (a): node; (b): saddle; (c): sink; (d):centre.

As mentioned, the nature of the fixed point is changed by variation of the control parameter  $\mu$ . Bifurcation can be subcritical if the number of fixed points decreases, supercritical if it increases and transcritical if the number of singular points stays unchanged. The bifurcation diagram in Figure B-2 shows the stability of the fixed points as a function of the control parameter  $\mu$ .

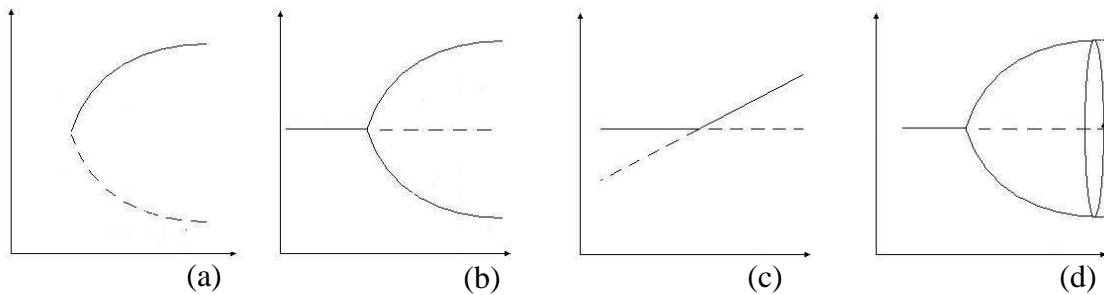


Figure B-2: Bifurcations of singular points. (a): Saddle-node bifurcation; (b): Supercritical pitchfork bifurcation; (c): Transcritical bifurcation; (d): Supercritical Hopf bifurcation.

A structurally stable system comes back to its equilibrium position if its parameters are slightly perturbed. A system is structurally unstable if its fixed points are non-hyperbolic. A fixed point  $\tilde{x}$  is non-hyperbolic if the Jacobian  $J(\tilde{x}, \mu) = (\partial f / \partial x)_{x=\tilde{x}}$  at that point has any eigenvalue with zero real part. Structural instability is necessary for bifurcation to occur, but it does not imply bifurcation automatically. The bifurcation size is determined by the number of eigenvalues of the Jacobian matrix with zero real parts. If there is no eigenvalue with zero real part, then no bifurcation occurs. Having two or more eigenvalues with zero real parts, then bifurcation of two or higher orders can take place. The general forms of the typical bifurcations are followed. The general form of the pitchfork bifurcation is represented in equation (B-5) with singular points are found by letting  $\dot{x} = 0$  leads to

$$\begin{aligned}\tilde{x} &= \pm\sqrt{\mu}. \\ \dot{x} &= \mu x - x^3\end{aligned}\tag{B-5}$$

The eigenvalues of Jacobian matrix of pitchfork bifurcation are

$$J(x, \mu) = \frac{\partial \dot{x}}{\partial x} = \mu - 3x^2\tag{B-6}$$

By substituting the fixed points, the eigenvalues are  $\lambda = \mu$  for  $\tilde{x} = 0$  and  $\lambda = -2\mu$  for  $\tilde{x} = \pm\sqrt{\mu}$ . When  $\mu = 0$ , the system is structurally unstable and bifurcation occurs. For  $\mu < 0$ , the only singular point is  $\tilde{x} = 0$ , which is stable as  $Re(\lambda) = \mu < 0$ . When  $\mu > 0$ , the singular point  $\tilde{x} = 0$  becomes unstable because of  $Re(\lambda) = \mu > 0$  and two other singular points  $\tilde{x} = \pm\sqrt{\mu}$  are added which both stable as  $Re(\lambda) = -2\mu < 0$ . The supercritical and subcritical solution branches deduced from the pitchfork bifurcation are presented in Figure B-3.

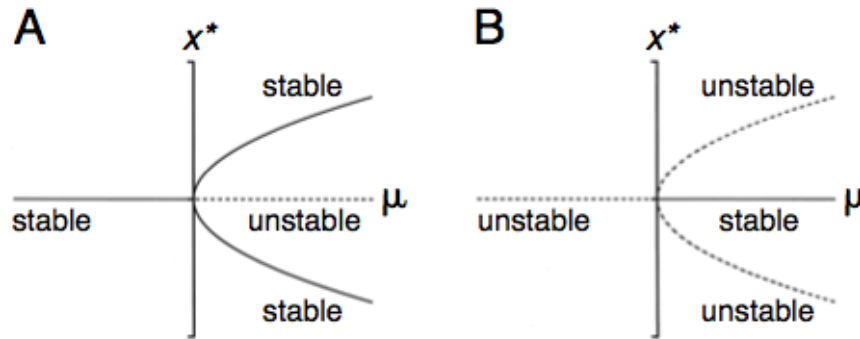


Figure B-3: (a) Supercritical pitchfork bifurcation diagram, (b) subcritical pitchfork bifurcation diagram, Solid line is stable states and dashed lines relate to unstable conditions

The saddle-node bifurcation is described in the form of  $\dot{x} = \mu - x^2$  with singular points  $\tilde{x} = \pm\sqrt{\mu}$ . The Jacobian matrix of the saddle-node bifurcation is  $J(x, \mu) = -2\tilde{x}$  with eigenvalue  $\lambda = -2\tilde{x}$ . The bifurcation parameter is  $\mu = 0$  and fixed point stability is determined by  $Re(\lambda) = -2\sqrt{\mu} < 0$ . The fixed point  $\tilde{x} = \sqrt{\mu}$  is therefore stable while  $\tilde{x} = -\sqrt{\mu}$  is unstable as shown in Figure B-4.

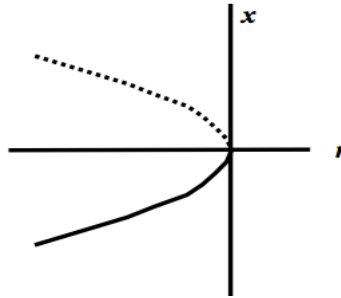


Figure B-4: Saddle node Bifurcation diagram, solid line (stable), dashed line (unstable).

The transcritical bifurcation general form with fixed points is

$$\begin{aligned}\dot{x} &= \mu x - x^2, \\ \tilde{x} &= 0, \tilde{x} = \mu.\end{aligned}\tag{B-7}$$

The transcritical Jacobian matrix obtained from equation (B-7) is  $J(x, \mu) = \mu - 2\tilde{x}$  with eigenvalue  $\lambda = \mu - 2\tilde{x}$ . The bifurcation parameter is  $\mu = 0$ . The singular point  $\tilde{x} = 0$  is stable for  $\mu < 0$  and unstable for  $\mu > 0$ . The second fixed point  $\tilde{x} = \mu$  is unstable for  $\mu < 0$  and stable for  $\mu > 0$ . The two equilibrium solutions therefore meet and change stability in the transcritical bifurcation as shown in Figure B-5.

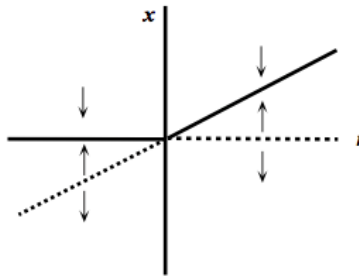


Figure B-5: Transcritical bifurcation diagram, solid line (stable), dashed line (unstable).

The Hopf bifurcation is characterized by a limit cycle, which means that the equilibrium point bifurcates into periodic motion. Therefore the bifurcation space is two dimensional. The general form of Hopf bifurcation with fixed points is

$$\begin{aligned}\dot{x} &= -y + x(\mu - (x^2 + y^2)), \\ \dot{y} &= x + y(\mu - (x^2 + y^2)), \\ (\tilde{x}, \tilde{y}) &= (0, 0).\end{aligned}\tag{B-8}$$

The Jacobian matrix of the Hopf bifurcation is  $J(x, \mu) = \mu \pm i$ . The bifurcation point is  $\mu = 0$ . The singular point is stable for  $\mu < 0$  and unstable for  $\mu > 0$ . At  $\mu = 0$ , a stable limit cycle exists for  $\mu > 0$ . The Hopf bifurcation, like the pitchfork bifurcation has supercritical and subcritical forms shown in Figure B-6. The subcritical form has inverted sign of equation (B-8) and so inverted stability.

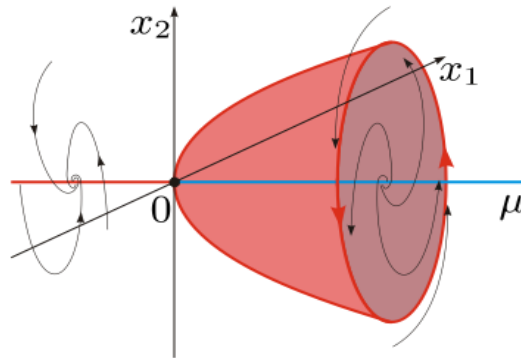


Figure B-6: Supercritical Hopf bifurcation diagram.

The limit cycle arises from the supercritical Hopf bifurcation can be subject to destabilization. The stability of limit cycle is studied through a periodic point which transformed by the period of limit cycle using the Poincare section.

$$x_{n+1} = G(x_n) \quad (\text{B-9})$$

The periodic solution corresponds to one periodic point  $\tilde{x}$  of the map  $G$  defined by  $\tilde{x} = x_{n+p} = x_n$  where  $p$  is the period of the limit cycle. Stability of the periodic orbit can be studied using Floquet theory. When the limit cycle loses its stability and undergoes a Hopf bifurcation, the limit cycle turns to a torus as shown in below figure.

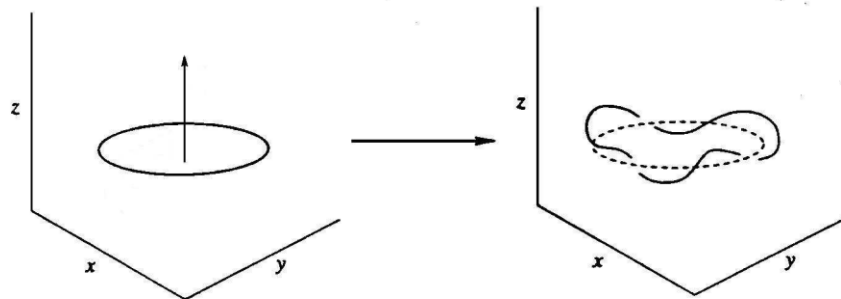


Figure B-7: Limit cycle undergoes torus doubling bifurcation.



The evolution of the system then is characterized by two frequencies, one related to the rotation around the principle axis and second to the rotation around the tore. The system depending on the frequency ratio to be rational or not can be periodic or quasi-periodic.

Another type of bifurcation is period-doubling or flip bifurcation that occurs only in periodic orbits as shown in Figure B-8.

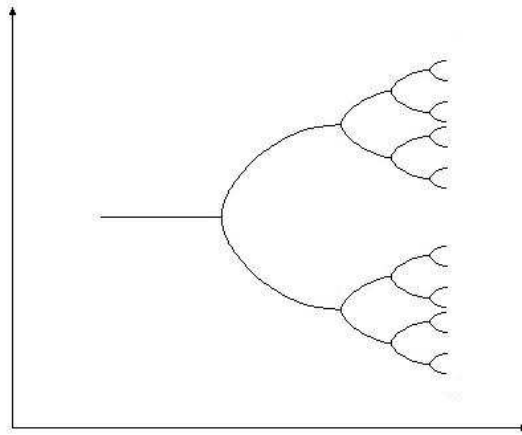


Figure B-8: Bifurcation diagram of a period-doubling cascade.

When the limit cycle loses its stability and the eigenvalues of the system takes the value -1, the flip bifurcation occurs. The limit cycle undergoes a period-doubling and period-2 cycle appears at low  $\mu$  value. With further increase of the bifurcation parameter  $\mu$ , the period-2 undergoes another period-doubling and becomes period-4 cycle and so on. This sequence of period-doubling occurrence is called period-doubling cascade (Hoyle, 2006).

### Numerical Floquet Theory

First, the basics of the Floquet theory are reviewed. If  $X$  is a fundamental solution matrix for a periodic system  $\dot{u} = [A(t)]u$  with  $X(0) = I$ , where  $I$  is the identity matrix, then by calculating the periodic coefficient matrix  $A(t)$  at  $t = t + \tau$  a new solution  $X(t + \tau)$  is produced. These two solution matrices can be related via matrix

$$X(t + \tau) = X(t)C \quad (\text{B-10})$$

Substituting  $t=0$  into equation (B-10) yields the monodromy matrix  $C = X(\tau)$ , that is integrated on the interval  $[0 - \tau]$ . Let  $Y(t)$  be another solution such that  $Y(t) = X(t)R$  where columns of  $R$

are the matrix of independent eigenvectors of the matrix  $C$ . Rewriting equation (B-10) in terms of  $Y(t)$  leads

$$Y(t + \tau) = Y(t)R^{-1}CR = Y(t)\Lambda \quad (\text{B-11})$$

where  $\Lambda$  is a diagonal matrix with the eigenvalues of  $C$ . Thus the  $i^{\text{th}}$  column of equation (B-11) can be written as

$$Y_i(t + \tau) = \lambda_i Y_i(t) \quad (\text{B-12})$$

The solution of equation (B-12) can be in the form of  $Y_i(t) = \lambda_i^{kt} p_i(t)$  where  $k$  is an unknown constant and  $p_i$  an unknown function. Substituting this into equation (B-12) gives

$$\lambda_i^{k(t+\tau)} p_i(t + \tau) = \lambda_i (\lambda_i^{kt} p_i(t)) \quad (\text{B-13})$$

It is satisfied when  $k = \frac{1}{\tau}$  and  $p_i(t)$  is a periodic function with period  $\tau$ . Then the solution becomes  $Y_i(t) = \lambda_i^{\frac{t}{\tau}} p_i(t)$  where  $p_i(t + \tau) = p_i(t)$ . To have a stable solution from this model,  $Y_i$  should remain bounded as  $t \rightarrow \infty$ . Therefore the eigenvalues of the matrix  $C$  determine the stability condition. If  $|\lambda_i| < 1$  then  $Y_i(t) \rightarrow 0$  as  $t \rightarrow \infty$ . Likewise if  $|\lambda_i| > 1$  then  $Y_i(t) \rightarrow \infty$  as  $t \rightarrow \infty$ . Thus, it is confirmed that norm of the eigenvalues of the matrix  $C$  should be less than or equal to unity in order to have stable solution.

### Poincare' Map for periodically excited forced vibration

The idea of Poincare comes from the response to this question that how the orbit behaves if we start very close to it.

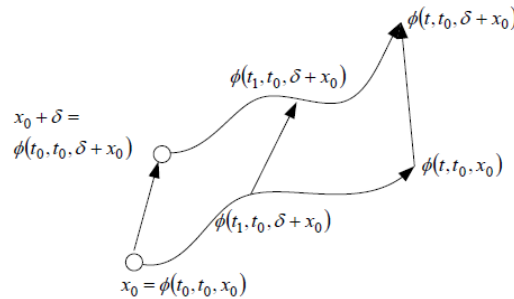


Figure B-9: Schematic of the perturbed fixed point around the periodic orbit.

The periodic function with initial perturbation is defined as

$$\begin{aligned}\delta &= \varphi(t_0, t_0, \delta + x_0) - \varphi(t_0, t_0, x_0) = \Delta\varphi(t_0, t_0, x_0) \\ \Delta\varphi(t, t_0, x_0) &= \varphi(t, t_0, \delta + x_0) - \varphi(t, t_0, x_0)\end{aligned}\quad (\text{B-14})$$

Therefore, the original perturbation is defined as

$$\begin{aligned}\varphi(t, t_0, \delta + x_0) &=^{TS} \varphi(t, t_0, x_0) + \frac{\partial\varphi(t, t_0, x_0)}{\partial x_0} \delta \leftrightarrow \\ \underbrace{\varphi(t, t_0, \delta + x_0) - \varphi(t, t_0, x_0)}_{\Delta\varphi(t, t_0, x_0)} &= \frac{\partial\varphi(t, t_0, x_0)}{\partial x_0} \delta \leftrightarrow \\ \Delta\varphi(t, t_0, x_0) &= \frac{\partial\varphi(t, t_0, x_0)}{\partial x_0} \Delta\varphi(t_0, t_0, x_0)\end{aligned}\quad (\text{B-15})$$

which is called variational equation. For  $t = t_0$  we have

$$\Delta\varphi(t_0, t_0, x_0) = \frac{\partial\varphi(t_0, t_0, x_0)}{\partial x_0} \Delta\varphi(t_0, t_0, x_0) \leftrightarrow \frac{\partial\varphi(t_0, t_0, x_0)}{\partial x_0} = I_{n \times n} \quad (\text{B-16})$$

So the sensitivity to the ICs is investigated by  $\frac{\partial\varphi(t, t_0, x_0)}{\partial x_0}$ . Considering a linear system in the form

of  $\dot{x}(t) = A(t)x(t)$  having a solution due to the perturbation as

$$\Delta\varphi(t, t_0, x_0) = \frac{\partial\varphi(t, t_0, x_0)}{\partial x_0} \Delta\varphi(t_0, t_0, x_0), \quad (\text{B-17})$$

hence  $\frac{\partial\varphi(t, t_0, x_0)}{\partial x_0} = \Phi_{STM}(t, t_0)$ . Thus, the partial derivative of the solution with respect to the initial condition is the state transition matrix (STM). The STM can be found numerically by solving

$$\frac{d}{dt} \Phi_{STM}(t, t_0) = A(t) \Phi_{STM}(t, t_0), \quad \Phi_{STM}(t, t_0) = I_{n \times n} \quad (\text{B-18})$$

Now, for a nonlinear system the same analysis is applied

$$\begin{aligned}
\varphi(t, t_0, x_0) &= x_0 + \int_0^t f(\varphi(\tau, t_0, x_0), \tau) d\tau \\
\frac{\partial \varphi(t, t_0, x_0)}{\partial x_0} &= I + \int_0^t \frac{\partial f(\varphi(\tau, t_0, x_0), \tau)}{\partial x_0} d\tau \\
\frac{\partial \varphi(t, t_0, x_0)}{\partial x_0} &= I + \int_0^t \frac{\partial f(\varphi(\tau, t_0, x_0), \tau)}{\partial \varphi(\tau, t_0, x_0)} \frac{\partial \varphi(\tau, t_0, x_0)}{\partial x_0} d\tau
\end{aligned} \tag{B-19}$$

As the RHS should equal to the LHS at  $t = t_0$ , then  $\varphi_{x_0}(t, t_0, x_0) = I_{n \times n}$ . In the linear system

$$\frac{\partial f(x(t), t)}{\partial x(t)} = A(t) \text{ which means that } \varphi_{x_0}(t, t_0, x_0) \text{ is the STM. Now, going back to the general}$$

solution of the nonlinear system, the Poincare map is

$$\varphi(T+t, t_0, x_0) = x_0 + \int_0^{T+t_0} f(\varphi(\tau, t_0, x_0), \tau) d\tau \leftrightarrow x_{n+1} = P(x_n) = x_n + \int_0^{T+t_0} f(\varphi(\tau, t_0, x_0), \tau) d\tau \tag{B-20}$$

The fixed point is  $\int_0^{T+t_0} f(\varphi(\tau, t_0, x_{FP}), \tau) d\tau = 0$  and the stability analysis defined as

$$\frac{\partial P(x_{FP})}{\partial x_{FP}} = I + \int_0^{T+t_0} \frac{\partial f(\varphi(\tau, t_0, x_0), \tau)}{\partial \varphi(\tau, t_0, x_0)} \frac{\partial \varphi(\tau, t_0, x_0)}{\partial x_0} d\tau \tag{B-21}$$

Hence, the monodromy matrix is nothing more than the Jacobian of the Poincare map.

$$\frac{d}{dt}(\varphi_{FP}(t, t_0, x_{FP})) = \left. \frac{\partial f(x, t)}{\partial x} \right|_{x=\varphi(t, t_0, x_{FP})} \varphi_{x_0}(t, t_0, x_{FP}), t \in [0, T] \tag{B-22}$$

From the Floquet Theory we know that the  $i^{\text{th}}$  column of the monodromy matrix is found by integrating the variational equation with an initial condition equal to the  $i^{\text{th}}$  column of the identity matrix for one period. The monodromy matrix differential equation in general case is calculated by numerically integrating with given input values of the equilibrium point, period and the system parameters. Thus to numerically determine the stability and bifurcation type of the solution, the following procedure in Matlab is summarized as

1. The monodromy matrix is calculated.
2. The norm of the eigenvalues of the monodromy matrix is checked to determine the stability and bifurcation type.

## APPENDIX C – INVARIANT AND EQUIVARIANT DERIVATION

The bifurcations of the systems with symmetry, including those where patterns are observed can be analyzed using group theory which is known as equivariant bifurcation theory. This theory determines that how the symmetry of patterns is affected by symmetry of the governing equations that produce them. The governing equations are derived through defining invariant and equivariant functions. Different systems are analyzed using this theory (Amdjadi, 2002; Dawes, 2000; Dawes, 2001; Dawes and Proctor, 2008; Ermentrout et al., 2012; Gunaratne et al., 1994; Porter and Knobloch, 2000, 2001; Rucklidge, 1997; Silber and Skeldon, 1999). The invariants and equivariant functions of the proposed model are developed as

$$\frac{\lambda_s}{\lambda_k} = \frac{\omega_k}{\omega_s} = \frac{m}{n} = 2; \quad n = 1, m = 2.$$

$$v(x, y, t) = S(t)e^{i\left(\frac{x}{\lambda_s} + \omega_s t\right)} f(y) + K(t)e^{i\left(\frac{x}{\lambda_k} + \omega_k t\right)} g(y)$$

$$T: x \rightarrow x + l\lambda_s$$

$$\theta: t \rightarrow t + \frac{\theta\lambda_s}{2\pi}$$

$$T(v) = S(t)e^{i\left(\frac{x+l\lambda_s}{\lambda_s} + \omega_s t\right)} f(y) + K(t)e^{i\left(\frac{x+l\lambda_s}{\lambda_k} + \omega_k t\right)} g(y) \Rightarrow S(t)e^{i\left(\frac{x}{\lambda_s} + \omega_s t\right)} \cdot e^{il} f(y) + K(t)e^{i\left(\frac{x}{\lambda_k} + \omega_k t\right)} \cdot e^{i\frac{\lambda_s}{\lambda_k} l} g(y)$$

$$T(S, K) \rightarrow \left( Se^{-il}, Ke^{-i\frac{\lambda_s}{\lambda_k} l} \right) = \left( Se^{-il}, Ke^{-i\frac{m}{n} l} \right) \Rightarrow T(S, K) \rightarrow (Se^{inl}, Ke^{iml})$$

$$\theta(v) = S(t)e^{i\left(\frac{x}{\lambda_s} + \omega_s \left(t + \frac{\theta\lambda_s}{2\pi}\right)\right)} f(y) + K(t)e^{i\left(\frac{x}{\lambda_k} + \omega_k \left(t + \frac{\theta\lambda_s}{2\pi}\right)\right)} g(y) \Rightarrow S(t)e^{i\left(\frac{x}{\lambda_s} + \omega_s t\right)} \cdot e^{i\theta} f(y) + K(t)e^{i\left(\frac{x}{\lambda_k} + \omega_k t\right)} \cdot e^{i\omega_k \frac{\lambda_s}{2\pi} \theta} g(y)$$

$$\theta(S, K) \rightarrow \left( Se^{-i\theta}, Ke^{-i\frac{\omega_k}{\omega_s} \theta} \right) = \left( Se^{-i\theta}, Ke^{-i\frac{m}{n} \theta} \right) \Rightarrow \theta(S, K) \rightarrow (Se^{in\theta}, Ke^{im\theta})$$

Invariants

$$(K^n \bar{S}^m)^2 = \left[ \left( Ke^{im\theta} \right)^n \left( Se^{in\theta} \right)^m \right]^2 = [K^n e^{imn\theta} \cdot \bar{S}^m \cdot e^{-imn\theta}]^2 = (K^n \bar{S}^m)^2$$

$$S^2 = S\bar{S} = Se^{in\theta} \cdot \overline{Se^{in\theta}} = S \cdot e^{in\theta} \cdot \bar{S} \cdot e^{-in\theta} = S\bar{S}$$

Equivariant functions

$$(S, \bar{S}^{2m-1} K^{2n}), (K, \bar{K}^{2n-1} S^{2m})$$

$$\bar{S}^{2m-1} K^{2n} = \left( \overline{S e^{in\theta}} \right)^{2m-1} \cdot (K e^{im\theta})^{2n} = \bar{S}^{2m-1} \cdot e^{-2imn\theta} \cdot e^{in\theta} \cdot K^{2n} \cdot e^{2imn\theta} = \bar{S}^{2m-1} K^{2n} \cdot e^{in\theta}$$

$$\bar{K}^{2n-1} S^{2m} = \left( \overline{K e^{im\theta}} \right)^{2n-1} \cdot (S e^{in\theta})^{2m} = \bar{K}^{2n-1} \cdot e^{-2imn\theta} \cdot e^{in\theta} \cdot S^{2m} \cdot e^{2imn\theta} = \bar{K}^{2n-1} S^{2m} \cdot e^{in\theta}$$